CHARACTERIZATION OF POROUS HYDROXYAPATITE AND β-WHITLOCKITE CERAMIC DISKS: AN APPLICATION OF PERCOLATION THEORY

by

RAYMOND D. SKWIERCZYNSKI

A thesis submitted in partial fulfillment of the requirements for the degree of

MASTER OF SCIENCE

(Pharmaceutics)

at the

UNIVERSITY OF WISCONSIN - MADISON

1990

CHARACTERIZATION OF POROUS HYDROXYAPATITE AND β-WHITLOCKITE CERAMIC DISKS: AN APPLICATION OF PERCOLATION THEORY

Raymond D. Skwierczynski

(Under the supervision of Professor James L. Wright)

The use of biomaterials as controlled release drug delivery devices is an emerging area of pharmaceutical research. Although many types biomaterials have been studied, biocompatible ceramics have not been considered as a potential drug delivery device in humans. In this research, we have shown that hydroxyapatite and β-whitlockite ceramic disks can be manufactured to give reproducible porosities, and that the sintering temperature is the principal variable that affects the amount of residual porosity in the disk.

The manufactured disks were characterized using percolation theory. From volume fraction accessible and volume fraction isolated data, which were obtained from pycnometry experiments, the critical percolation threshold

and coordination of the sintered ceramic disks were obtained. The critical percolation threshold and coordination of both ceramic lattices correspond to tetrakaidecahedral tessellations.

Finally, the bulk diffusion coefficients of a water-soluble substance, benzoate ion, through hydroxyapatite disks were obtained using the Stokes diaphragm cell method. Using percolation theory, the bulk diffusion coefficients were modeled as a function of the disk porosity and critical percolation threshold.

To my wife,

Tamara

Acknowledgements

I would like to express my sincere appreciation to:

Professor James L. Wright for his enthusiastic guidance and support during this research;

Professor Kenneth A. Connors for his assistance in preparing this thesis;

Professor Sturges W. Bailey for his help in obtaining the x-ray diffraction spectra;

Mr. Mark W. Tengowski, from the Integrated Microscopy Resource for Biomedical Research, for performing the scanning electron microscopy;

Mr. Scott R. Ellis and Ms. Jayne E. Hastedt for their helpful discussions regarding ceramics, percolation theory, and diffusion;

Mr. Michael J. Mulski for being a great roommate and friend;

The Wisconsin Alumni Research Foundation for the financial support; and finally,

The Chemistry Department at the University of Wisconsin - Eau Claire for the excellent undergraduate education and, more importantly, for the lasting friendships that were made while I was there.

Table of Contents

Table of Contents (*continued*) Page

Table of Contents (*continued*)

Table of Contents (*continued*) Page

List of Figures

List of Figures (*continued*)

List of Figures (*continued*)

List of Figures (*continued*)

List of Figures (*continued*)

List of Figures (*continued*)

List of Tables

List of Tables (*continued*)

List of Tables (*continued*)

I. Introduction

The pore structure of a porous composite consists of an interconnected three-dimensional network of pores and capillaries. The network geometry consists of capillary segments of different shapes and sizes which are distributed over the network in some irregular fashion. Introduction of a complicated internal geometry greatly increases the required physical information and mathematical complexity needed to model diffusion of a solute through porous composites. In order to apply a rigorous model to the diffusion of a solute in a porous composite, one must know the complete geometrical (shape) and topological (connectedness) characteristics of the composite and the diffusion coefficient of the solute in all parts of the composite. These are often difficult or impossible to determine experimentally.

There is no obstacle to the complete numerical solution of the problem of diffusion in a porous composite; however, one has to compromise and work with far less than a complete characterization of the system. In this investigation, we explore the possible utility of using percolation theory (*1-3*) to describe the transport of a solute through a porous composite.

A. Percolation theory

A porous composite can be thought of as a binary interspersion of pores and material. Since a complete characterization of the morphological state of the composite cannot be determined easily, one must propose a method to measure the state of the interspersion. One such method makes use of the volume fraction ϕ of pores present (*4*). In a porous composite, the pores can exist either as isolated clusters that are completely surrounded by material or as sample-spanning clusters that allow passage of a diffusing solute from one side of the composite to the other. The sample-spanning pores constitute the volume fraction accessible ϕ^a, and the isolated clusters of pores constitute the volume fraction isolated ϕ^i. The total porosity is equal to the sum of the volume fraction accessible and the volume fraction isolated:

$$\phi = \phi^a + \phi^i \qquad (1)$$

Figure 1 (*5*) illustrates the concept of volume fraction accessible and volume fraction isolated for a two dimensional square lattice with a porosity ϕ of 0.50.

If ϕ is below a critical value ϕ_c, called the critical percolation threshold, ϕ^a is identically equal to zero for

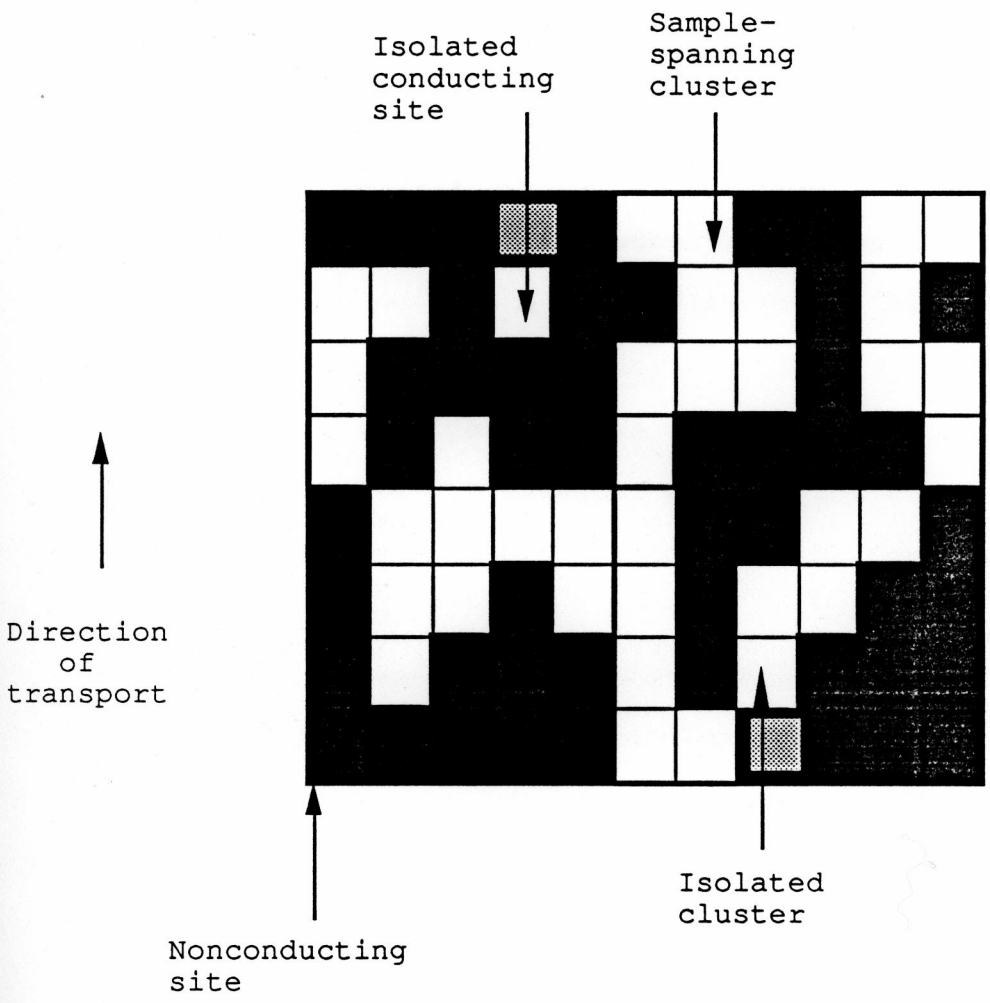

Figure 1. Two-dimensional square lattice (ϕ = 0.50). The white conducting sites represent pores and the black nonconducting sites represent material.

an infinitely large sample. Thus from eq 1, all of the pores are distributed as isolated clusters and $\phi = \phi^i$. The dependence of ϕ^a and ϕ^i on ϕ is shown in Figure 2 for a computer-simulated binary interspersion (*6*). The interspersion was generated by randomly distributing conducting (pores) and nonconducting (material) sites arranged in a three-dimensional cubic lattice (*4*) shown in Figure 3. The critical percolation threshold was determined to be 0.32. The critical percolation threshold is dependent upon the type of lattice in which pores and material are arranged.

A quantity relevant to transport processes in composite systems is the volume fraction effective ϕ^e. To compute ϕ^e, a diffusivity equal to the aqueous diffusion coefficient, D_{aq}, is assigned to the conducting sites and a diffusivity of zero is assigned to the nonconducting sites. A linear transport law is then assumed

$$J_B = -D_B \, (\partial C/\partial x) \qquad (2)$$

where J_B is the flux and $\partial C/\partial x$ is the concentration gradient of diffusing solute through the porous composite. The diffusivity of the solute through a large portion of the composite is termed the bulk diffusion coefficient D_B.

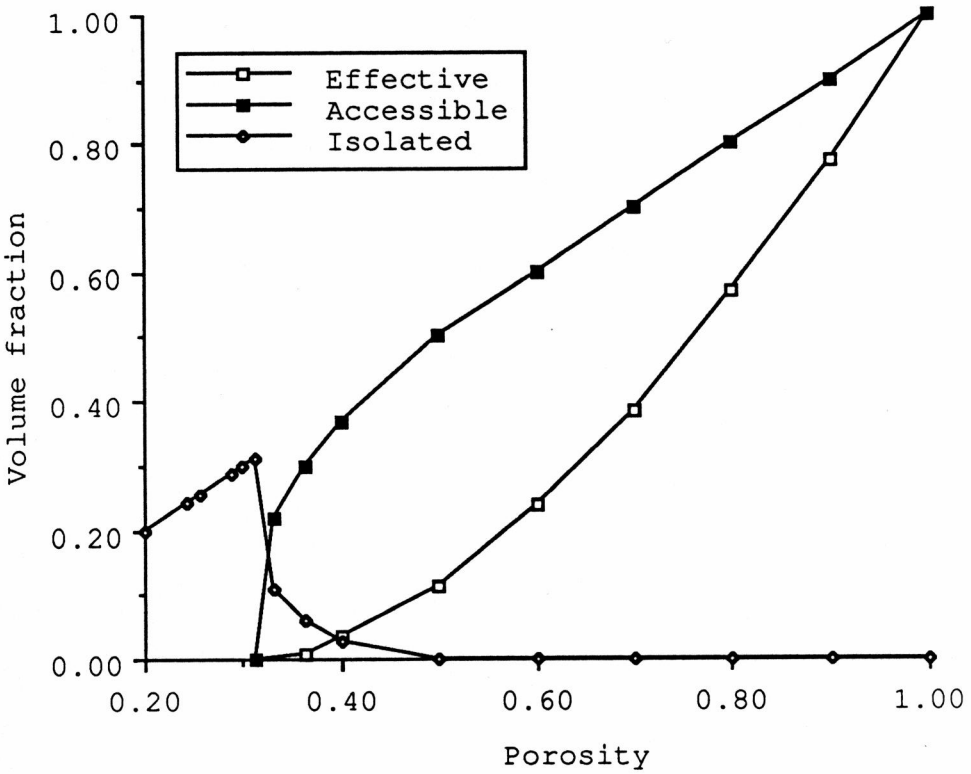

Figure 2. Volume fraction as a function of porosity for a three-dimensional cubic lattice (z = 6).

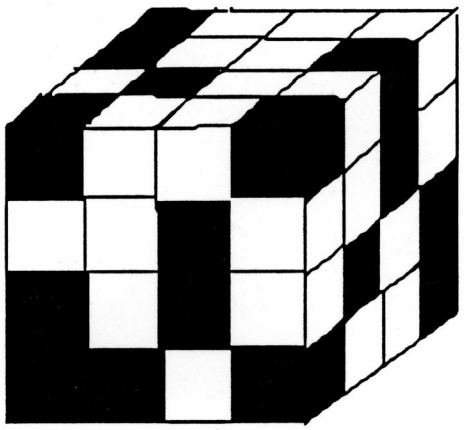

Figure 3. Three-dimensional cubic lattice (z=6). The black cubes are nonconducting sites and the white ones are conducting sites.

The volume fraction effective is defined as the ratio of the bulk diffusion coefficient to the aqueous diffusion coefficient

$$\phi^e \equiv \frac{D_B}{D_{aq}} \tag{3}$$

If all of the pores consisted of right circular cylinders arranged parallel to the flux, the bulk diffusion coefficient would equal the aqueous diffusion coefficient, and $\phi^e = \phi^a$. However, in disordered interspersions, the pores contributing to the sample-spanning clusters are tortuous and may have dead ends that do not contribute to the diffusion of the solute, so in general $\phi^e \leq \phi^a$. Since ϕ^a equals zero below the critical percolation threshold, ϕ^e also equals zero. Above the critical percolation threshold the following is true, $0 \leq \phi^e \leq \phi^a$.

Near the critical percolation threshold, when $\phi \geq \phi_c$, the volume fraction accessible and volume fraction effective obey the following scaling relationships (*1-4*)

$$\phi^a \alpha (\phi - \phi_c)^\beta \tag{4}$$

and

$$\phi^e \alpha (\phi - \phi_c)^\mu \tag{5}$$

where $\beta < 1$ and $\mu > 1$. The notion of β less than unity for all lattices regardless of dimensionality or coordination (number of nearest neighbors), is consistent with the physical fact that at the percolation threshold two large isolated clusters are suddenly connected by the addition of one conducting site. Thus $\partial\phi^a/\partial\phi$ is discontinuous at $\phi = \phi_c$ and

$$\lim_{\phi^+ \to \phi_c} \frac{\partial \phi^a}{\partial \phi} \to \infty \tag{6}$$

The scaling exponent μ is always greater than unity, since the addition of one conducting site at the critical percolation threshold allows transport across the composite. Thus $\partial\phi^e/\partial\phi$ is continuous at $\phi = \phi_c$ and

$$\lim_{\phi^+ \to \phi_c} \frac{\partial \phi^e}{\partial \phi} \to 0 \tag{7}$$

Although there has been much debate concerning the values of β and μ, they are regarded as universal scaling

exponents and are usually taken equal to 0.4 and 2.0, respectively, for a three-dimensional lattice (*1*).

At porosities less than the critical percolation threshold, the pores exist only as isolated clusters. As the porosity increases toward ϕ_c larger clusters appear. At ϕ_c, ϕ^i is a maximum and $\partial\phi^i/\partial\phi$ is discontinuous. With a further increase in porosity, the sample-spanning clusters continue to grow at the expense of the isolated clusters, that is, ϕ^a increases as ϕ^i decreases.

The major determinant of ϕ_c is the coordination of the lattice. Since an increase in coordination number increases the probability of a sample-spanning cluster being formed at a given porosity, the critical percolation threshold must necessarily decrease (*7-9*). See Figure 4 (*10*). For a three dimensional lattice with a coordination number z greater than 12, a good approximation to ϕ_c is (*4*)

$$\phi_c \approx \frac{2.5}{z} \qquad (8)$$

Figures 5 and 6 show the dependence of volume fraction accessible (*7*) and volume fraction effective (*6,11*), respectively, on the coordination number of the lattice.

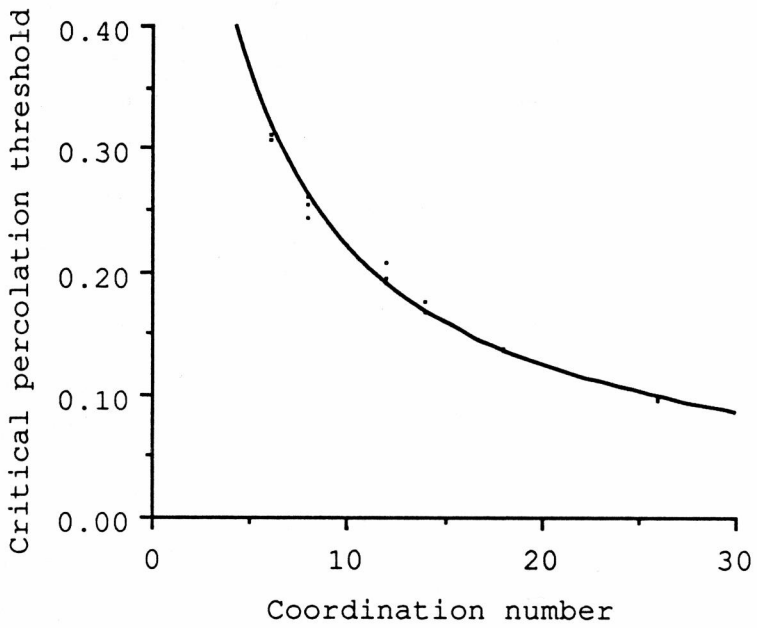

Figure 4. Critical percolation threshold ϕ_c as a function of coordination number for three-dimensional lattices.

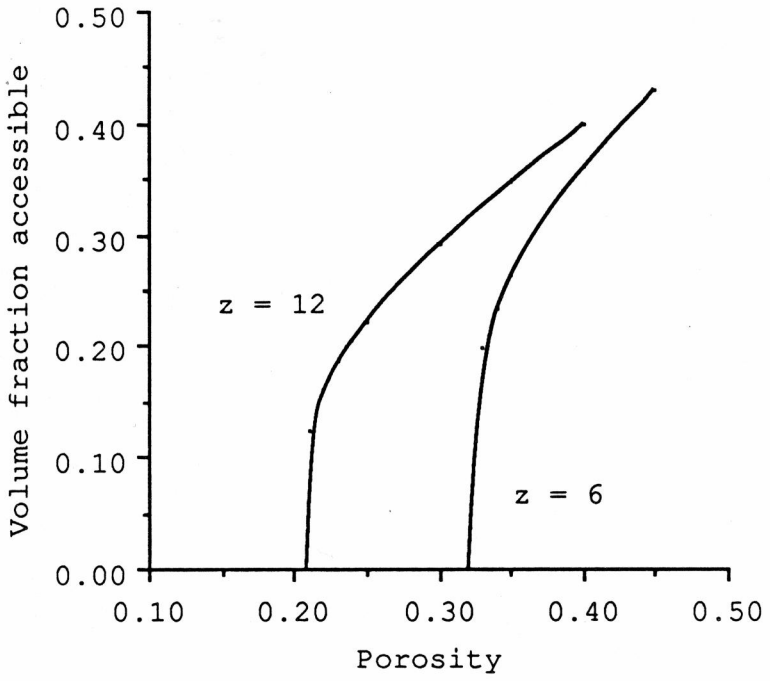

Figure 5. Volume fraction accessible ϕ^a as a function of porosity for three-dimensional lattices of different coordinations.

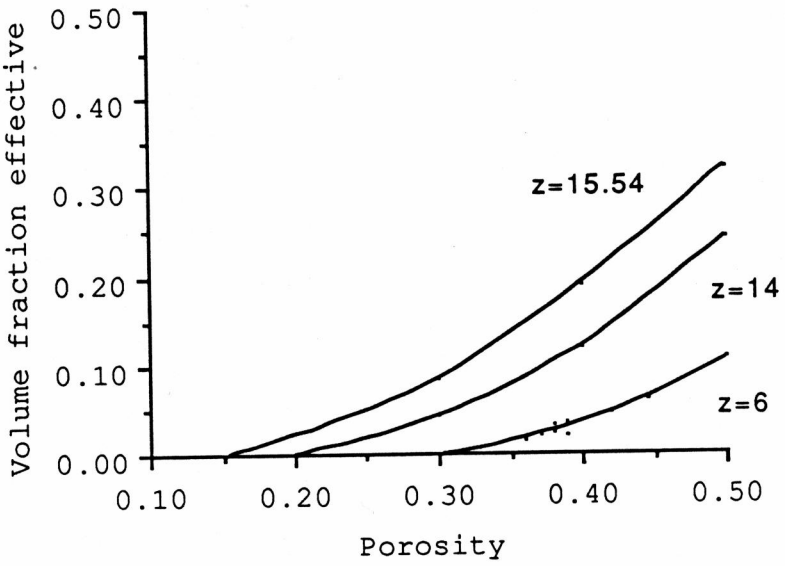

Figure 6. Volume fraction effective ϕ^e as a function of porosity for three-dimensional lattices of different coordinations.

Percolation theory has been used to model critical processes such as phase transitions (*1*), gelation and polymer branching (*1-2,12-14*), diffusion (*1,2*), diffusion and reaction (*4*), and ferromagnetism (*2*). The types of interspersions studied can be divided into two classes: dynamic interspersions, where the morphology changes during the process, and static interspersions, where the morphology does not change appreciably during the process of interest (*4*). Examples of dynamic interspersions studied in our laboratory include the diffusion of a solute from a polymer matrix (*5,10,15*) and the uptake of water by a hygroscopic solute in a polymer matrix (*16*). The diffusion of a solute through porous ceramic compacts (*17-20*) is an example of a static interspersion studied in our laboratory.

B. Ceramics

In order to model the diffusion of a solute through composites consisting of material and pores using percolation theory, one must be able to control the volume fraction of pores ϕ. In this research, we chose to use ceramics as our composite. Ceramics are inorganic, nonmetallic materials that are processed at high temperatures. The porosity of the ceramic can be

reproducibly controlled by altering the manufacturing process (*21*), which can be regarded as a four-step process: (1) granulation of the starting powder, (2) compaction of the powder into disks, (3) low temperature firing, and (4) high temperature firing.

1. Granulation

In this step, the raw ceramic powder is mixed with an organic polymer which binds the powder particles. The granulation can be performed in the presence or absence of water; in this research, the ceramic powders were granulated with a aqueous polymer solution since this wet granulation procedure gave more reproducible results. The porosity of the final ware can be controlled by altering the amount of granulating material used (*21*).

2. Compaction

After drying, the granulated ceramic powder is ground with mortar and pestle, then compacted into disks. As in the tableting of solid pharmaceutical dosage forms (*21,23*), the residual porosity of the ceramic disks can be controlled by varying the applied compaction load.

3. Low temperature firing

The compacted disks are placed in a furnace and are heated slowly to 720° C. During the low temperature firing, the organic granulating agent and other impurities are "burned out," that is, they are oxidized and vaporized. The disks are then slowly cooled to room temperature. The rate of heating and cooling can affect the amount of residual porosity in the disk (*24*), so it is important to establish and follow a prefiring schedule. Also, cooling the disks too rapidly may result in cracking (*25*).

When the prefiring procedure is complete, the disks are referred as being "green." A green (*21*) ceramic is an unsintered compacted powder that has a significant amount (≈ 50%) of residual porosity.

4. High temperature firing

During high temperature firing of the porous green compact, three major changes occur (*24,26*): an increase in average grain size, a change in pore shape, and a change in pore size and number. These processes, which usually take place by solid-state diffusion, are collectively termed sintering.

The properties of ceramics are determined not only by their composition and chemical structure of the phases

present, but also by the arrangement of these phases (the microstructure) (*26*). The microstructure of the ceramic product depends on the fabrication process, the raw materials used, and the kinetics and degree of grain growth and densification which take place during sintering.

The raw ceramic powders consist of macroscopic particles. Each particle consists of an agglomerate of small (<1 μm) grains which are highly curved and possess a high surface free energy. During sintering, the surface free energy of the grains are lowered by grain growth and densification.

Grain growth

The driving force for grain growth is the difference in surface free energy between the fine-grained material and the larger grain-size product (*26*). Atoms diffuse across a grain boundary (the solid-solid interface between two grains), toward the center of curvature of the larger grain (*26*); see Figure 7. The grain growth process can also be thought of as a movement of the grain boundary. The boundary of a convex grain moves away from the center of curvature, that is, the grain grows larger; whereas a boundary of a concave grain moves toward the center of curvature, or the grain "grows" smaller. The rate at which

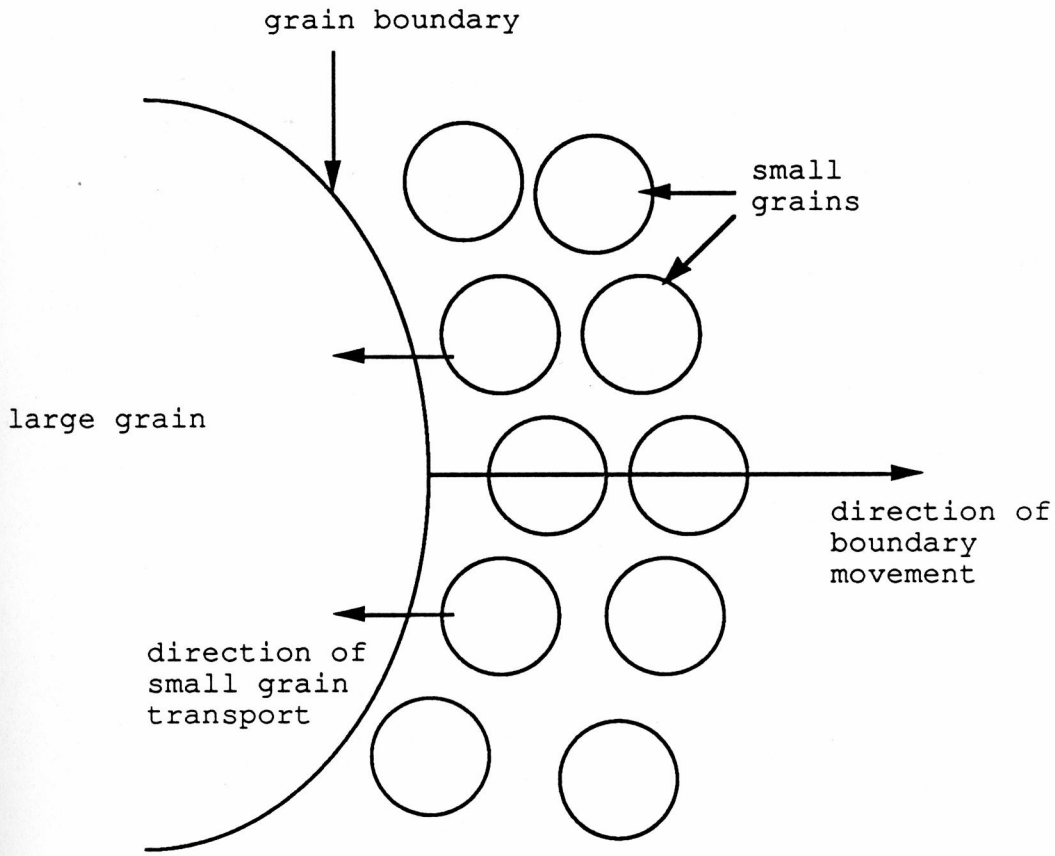

Figure 7. In grain growth, atoms diffuse across the grain boundary toward the center of curvature of the large grain. The large grain grows, that is, the grain boundary moves away from the center of curvature.

a grain grows is proportional to r^n, where r is the radius of curvature of the grain and n is a positive constant that is dependent on the solid-state diffusion mechanism that takes place (*26*). Since a smaller particle has a higher radius of curvature, the rate of grain growth is inversely proportional to the particle diameter of the starting raw material. Therefore, the particle size distribution of the starting raw material is an important controllable variable.

Grain growth is also proportional to the diffusion coefficient of the atoms. Since diffusion can be regarded as a thermally activated process (*27*), the diffusion coefficient can be expressed as

$$D(T) = D_0 \exp\left(\frac{-\Delta G^{\ddagger}}{kT}\right) \qquad (9)$$

where

T is the absolute temperature,

k is the Boltzmann constant

($k = 1.38066 \times 10^{-23}$ J K^{-1}),

$\Delta G^{\ddagger}$ is the Gibbs free energy of activation, and

D_0 is a pre-exponential factor which is slightly dependent on temperature.

From eq 9, the diffusion coefficient and rate of grain growth can be increased by raising the sintering temperature.

When a second phase inclusion is present in the compacted ceramic, the energy necessary for movement of the grain boundary is increased (*26*). Inclusions tend to inhibit grain growth and to limit the final grain size of the product. Second phase inclusions are often added to the raw ceramic powder during granulation. For example, a small amount (~ 1% w/w) of MgO is sometimes added to inhibit the grain growth of aluminum oxide ceramics (*20,26*). Although a second ceramic phase was not added to the powders in this study, a second phase inclusion, residual porosity, is always present in green ceramic compacts. In the latter stages of sintering, the residual pores are dragged along with the grain boundary, retarding the rate of grain growth (*26*). The pores tend to accumulate in the corners between grains, hence affecting the microstructure of the sintered ceramic compact.

Secondary recrystallization, sometimes called discontinuous or exaggerated grain growth (*26*), occurs when a small fraction of grains grows to a large size, consuming the uniform grain-size matrix. Once a single grain grows to such a size, it has many highly curved sides and the

grain grows more rapidly than the smaller neighboring grains of fewer sides. Secondary recrystallization is particularly likely to occur when continuous grain growth is inhibited by the presence of impurities or pores. Under these conditions, the only boundaries that are able to move are those with a curvature much larger than the average, that is, the exaggerated grains with highly curved sides are able to grow, whereas the matrix grains remain uniform in size. Secondary recrystallization will take place at higher sintering temperatures and usually results in small changes in porosity.

Diffusion mechanisms and densification

The thermodynamic driving force for densification is the decrease in surface free energy by elimination of solid-vapor interfaces (*26*). Different mass transport mechanisms govern grain growth and densification (*26*). One mechanism that takes place during the sintering of low vapor pressure ceramics, such as the alkali halides, is evaporation-condensation (*26*). Although this transport process does not occur during the sintering of the ceramics studied in our laboratory, the mechanism illustrates an important consequence of the curvature of small grains. Figure 8 shows two spherical ceramics grains that are

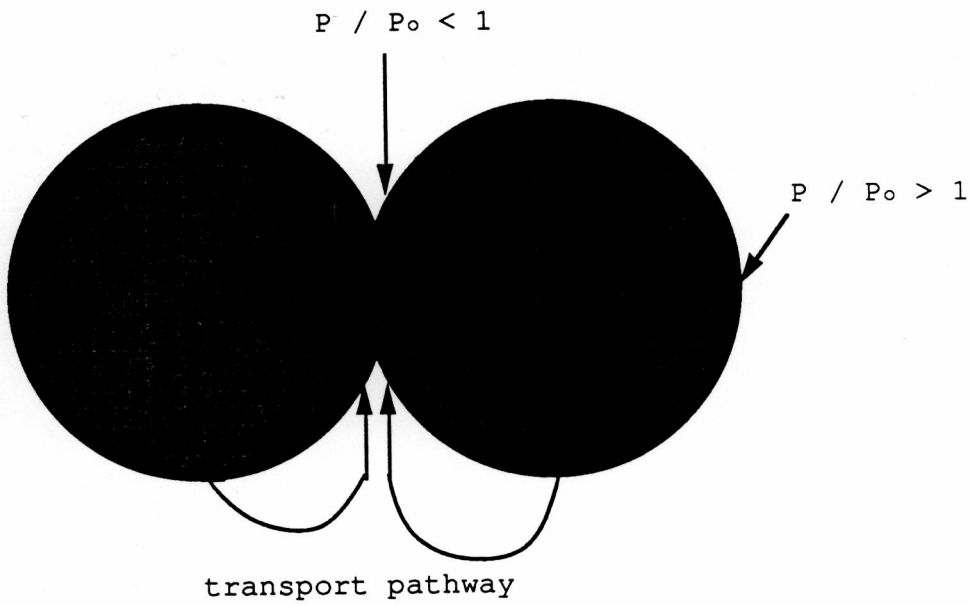

Figure 8. In evaporation - condensation, atoms from the grain surface where $P / P_o > 1$ vaporize and condense in the neck region where $P / P_o < 1$.

joined by a small region called a neck. The radius of curvature of the neck region is negative, that is, the grain boundary is concave with respect to the center. The grain boundary curvature in the other areas of the grain is positive.

The vapor pressure P of a curved surface is different from that of a flat surface P_0. The two pressures are related by the Kelvin equation (*28*)

$$\ln \left(\frac{P}{P_0}\right) = \frac{2\gamma V_m}{RTr} \qquad (10)$$

where Vm is the molar volume,

R is the gas constant ($R = 8.314$ J mol^{-1} K^{-1}),

T is the absolute temperature,

r is the radius of the grain, and

γ is the surface free energy of the grain.

In the regions of positive curvature, $P > P_0$, so at high temperatures, an atom from the surface can easily sublime. In the neck region, $P < P_0$, thus a vaporized atom will tend to condense in this area. When matter is transported from the surface of the regions with positive curvature to the neck, the distance between the centers and the porosity remain unchanged. Only the shape of the pore changes. If the atom from the surface (*26*) is transferred to the neck

by diffusion along the grain boundary or by diffusion along the surface, the same result will occur, as shown in Figure 9. However, if the diffusing atom originates from a grain boundary or a lattice defect (Figure 9), the distance between the grain centers will become smaller and pores will be eliminated (*26*). When the porosity of a ceramic compact decreases, densification has taken place.

In summary, during high temperature firing of a green ceramic, changes in grain size, pore shape, pore size, and porosity occur. The sintering processes are governed by different mass transfer mechanisms. Depending on the source of the diffusing atom, either grain growth or densification will occur. The rate and degree of grain growth and densification can be controlled by varying the initial particle size of the raw ceramic powder, and by varying the sintering time and temperature.

C. Calcium phosphate bioceramics

Although the existence of ceramics has been traced to ancient civilizations, the idea of using ceramics as a biomaterial was not conceived until 1963 when Smith announced that a composite of aluminum oxide and a polymer could be successfully used as a bone replacement material (*29*).

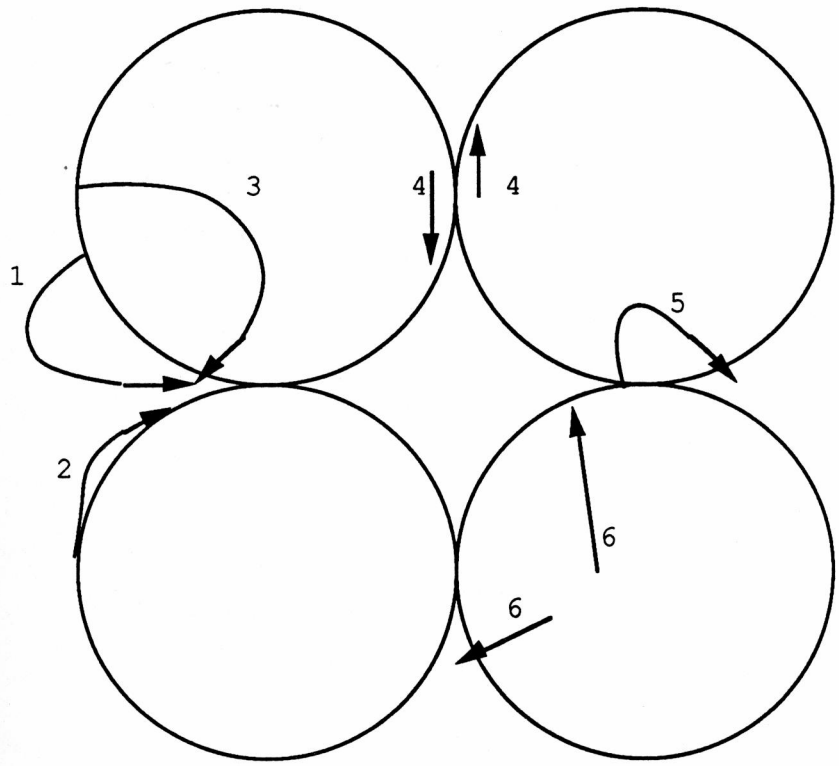

Figure 9. Alternate paths for matter transport during sintering. In each mechanism, matter is transferred to the neck region. If the diffusing atom is from the surface, the porosity will not change. Densification occurs if the diffusing atom is from a grain boundary or a dislocation in the lattice.

Mechanism	Transport Path	Source of Matter
1	Vapor transport	Surface
2	Surface diffusion	Surface
3	Lattice diffusion	Surface
4	Boundary diffusion	Grain boundary
5	Lattice diffusion	Grain boundary
6	Lattice diffusion	Dislocation

Bioceramics fall into three classes: inert, surface active, and resorbable (*30-31*). Inert ceramic materials have been used for heart valves, hip joint replacements, and electronic implants, where strength, durability, and lack of physiological response is needed. The term "inert" refers to materials that are essentially stable with little or no tissue reactiviity when implanted in the living organism. Aluminum oxide is an inert bioceramic studied in our laboratory (*17,19-20*).

Conversely, surface active ceramics, such as hydroxyapatite ($Ca_{10}(OH)_2(PO_4)_6$), react chemically with the physiological environment (*30-32*). For example, as a broken bone heals, the hard tissue and the implant surface form interfacial bonds (*30-32*), which protect the implant from dislocation due to imposed stresses. The chemical and mechanical (porosity) characteristics encourage hard and soft tissue ingrowth where stability and fixation to bone are of primary concern, such as tooth implants and artificial joints (*30-36*). A review of surface active ceramics is given by Hench and Wilson (*37*).

Resorbable ceramics serve as temporary space fillers and scaffolds for the development of new tissue (*30-32,36*). Natural tissue reconstruction occurs simultaneously with resorption. As the ceramic dissolves, it becomes more

porous, allowing the ingrowth of more supporting tissue. As a result mechanical integrity is maintained and stress concentrations are minimized. Two bioceramics that have been found to be resorbable are macroporous hydroxyapatite (average pore diameter is greater than 100 μm) and β-whitlockite (*30-36*). Resorbable bioceramics have been used to treat defects of the face and jaw, and to serve as artificial tendons and composite bone plates (*30-36*).

The pore size of the bioceramic is important because attachemnt occurs only if tissue can grow into the prosthetic. Pore sizes of 10 - 44 μm in aluminum oxide show only a small amount of tissue ingrowth with no detectable bone growth, where as 75 - 100 μm pore diameters show complete connective tissue infiltration (*30*). As with aluminum oxide, bony tissue will grow into hydroxyapatite and β-whitlockite that has pores in the 100 μm range (*30-36*). A bioceramic that has pores greater than 100 μm is termed macroporous, a microporous bioceramic has pore sizes less than 100 μm, and a dense ceramic is a microporous ceramic that has a porosity ϕ less than 0.05 (*36*).

Hydroxyapatite and β-whitlockite

In this research two static bioceramic interspersions, microporous hydroxyapatite and microporous β-whitlockite

compacts, were characterized using the ideas of percolation theory. Microporous hydroxyapatite is compatible with bone and exhibits little or no biodegradation after a six-month implantation period (*38*). This is not unexpected since naturally occurring hydroxyapatite is the major constituent of osseous and dental hard tissue (*30*). The interfacial bond between the hydroxyapatite and bone is stronger than the implant or bone itself; furthermore, the implant cannot be removed without fracturing the surrounding bone (*31,39*).

Holmes (*40*) observed that macroporous hydroxyapatite implanted in the mandibles of dogs is also biocompatible. But in contrast with the microporous hydroxyapatite, 29% of the ceramic degraded after a 12-month implantation period.

Porous β-whitlockite can promote the ingrowth of soft tissue and bone. Since it is bioresorbable, it can aid in the natural regeneration and healing of bone. β-Whitlockite has been used for repair of periodontal loss, mastoid replacement, and joining of vertebrae (*30-32,36-37*). Macroporous β-whitlockite implanted into rat tibias showed a 46% degradation after 24 weeks with significant tissue ingrowth (*33*). The resorption behavior of hydroxyapatite and β-whitlockite can be rationalized by their physical chemical and mechanical properties. First, the solubility of β-whitlockite is greater than the

solubility of hydroxyapatite at all pH's. The intrinsic solubility constant for β-whitlockite is 1.38×10^{-29}, whereas the intrinsic solubility constant for hydroxyapatite is 1.38×10^{-58} (*32*). Since the dissolution rate is governed by the intrinsic solubility (*41*), β-whitlockite should resorb faster. Second, since dissolution rates depend on specific surface area (*41*), densely sintered ceramics should show a smaller tendency to degrade than porous ceramics. Thus, macroporous hydroxyapatite is resorbed and microporous hydroxyapatite tends to be stable.

Finally, β-whitlockite (β-$Ca_3(PO_4)_2$) ceramics are prepared from hydrated tricalcium phosphate ($Ca_3(PO_4)_2$) powder. Unheated hydrated tricalcium phosphate powder has an apatite structure (*36*). A phase transition occurs when the powder is heated to temperatures greater than 800° C, forming β-whitlockite (*36*). Hence the term β-whitlockite will be used when referring to heated tricalcium phosphate powders or sintered tricalcium phosphate compacts.

D. Statement of the problem

The use of biomaterials as controlled release drug delivery devices is an emerging and interesting area of pharmaceutical research. Although numerous biomaterials have been used, most of them are derived from organic polymers, silicon polymers, or paraffin waxes, and the porosity and pore geometry are highly dependent on the amount of polymer cross-linking (*42-60*). Presently, ceramics have not been considered as a potential drug delivery device in humans.

The objectives of this research are to reproducibly manufacture hydroxyapatite and β-whitlockite compacts of different porosities, to characterize these compacts in terms of volume fractions of pores, and to model the diffusion of a water-soluble substance through the ceramic composites as a function of the porosity of the composite using the principles of percolation theory.

II. Experimental

A. Characterization of powders

Hydroxyapatite (calcium phosphate tribasic, $Ca_{10}(OH)_2(PO_4)_6$, Lot no. 88013LM) was obtained from Aldrich Chemical Company (Milwaukee, WI). Tricalcium phosphate ($Ca_3(PO_4)_2$, Lot no. 264909) was obtained from Fluka Chemie AG (Buchs, Switzerland).

1. Particle size distribution

The particle size distribution of each of the calcium phosphate powders was determined using an Olympus BH2 plane polarized light microscope equipped with a 10X eyepiece and a 20X objective lens, which provided a magnification of 200X with a resolution of 0.46 μm. The microscope was calibrated using a ruled calibration slide obtained from Graticules, LTD (Tonbridge, England).

2. Elemental analysis

The calcium phosphate powders were analyzed using inductively coupled plasma (ICP) spectroscopy in order to determine the concentration of trace impurities in the samples. The analyses were performed by Hazelton Laboratories, Incorporated (Madison, WI).

3. Density of powders

Hydroxyapatite and tricalcium phosphate powders were placed in separate aluminum oxide crucibles and were heated to 1300 °C in a Type 51314 box furnace equipped with a Type 59246 control console (Lindberg; Watertown, WI). Densities of the powders were determined using helium pycnometry on a model MVP-1 multipycnometer (Quantachrome Corporation; Syosset, NY). The multipycnometer, shown schematically in Figure 10, consists of a reference cell and a sample cell. The two cells are connected by a short piece of tubing which contains a valve. Powder was placed in the sample cell of the multipycnometer. With the valve between the cells closed, the reference cell of the multipycnometer was pressurized with helium gas to an initial pressure P_1. The valve was then opened, allowing the helium to enter the sample cell; the final pressure decreased to P_2. Since the volume of the reference cell (V_1), the volume of the sample cell (V_2), and the initial and final pressures are known, the volume of the powder (V_S) can be calculated using Boyle's Law

$$V_S = V_1 \left(\frac{P_1}{P_2} - 1 \right) - V_2 \qquad (11)$$

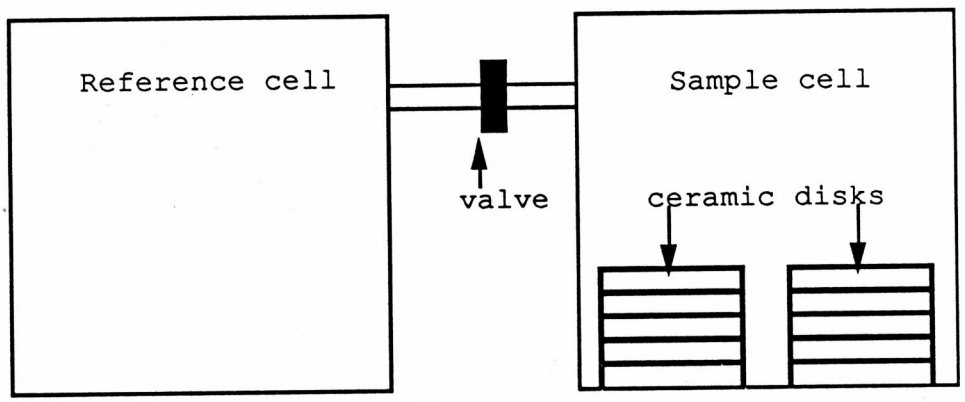

Figure 10. The multipycnometer consists of a reference cell and a sample cell of known volumes. The two cells are connected by a short piece of tubing which contains a valve. Sample, powder or disks, is placed in the sample cell of the multipycnometer. With the valve between the cells closed, the reference cell is pressurized with helium gas to an initial pressure P_1. The valve is then opened allowing the helium to enter the sample cell; the final pressure decreases to P_2.

The pycnometric density ρ_{pyc} can be calculated by

$$\rho_{pyc} = \frac{M_S}{V_S} \qquad (12)$$

where M_S is the total mass of the powder.

4. Differential scanning calorimetry (DSC)

Differential scanning calorimetry was performed on a TA3000 DSC system equipped with a TC 10A TA Processor and a DSC 20 Standard Cell (Mettler Instrument Corporation; Highstown, NJ). The calorimeter was calibrated using an indium calibration standard provided by Mettler.

5. X-ray diffraction spectrommetry

X-ray diffraction analysis of preheated hydroxyapatite and tricalcium phosphate powders was performed using a PAD V Diffraction System (Santa Clara, CA). The recorded spectra were compared with spectra in the JCPDS mineral data base (*61*) in order to identify the polymorphs of calcium phosphate present.

B. Manufacturing of disks

1. Granulation

In a preliminary granulation experiment, various amounts of polyvinylpyrrolidone (PVP) K-15 powder (GAF Corporation; Wayne NJ) were mixed with each calcium phosphate powder. As the powders were mixed, 10.0 g of distilled deionized (Sybron-Barnstead; Boston, MA) water was added dropwise. From this experiment, it was determined that 10% (w/w) PVP gave optimum powder handling and compaction properties.

A wet granulation process was used in subsequent experiments, in order to minimize the variation of porosity within a lot of manufactured disks. A 20.2% PVP aqueous solution was prepared by diluting a 45% aqueous solution of PVP K-60 SOL (GAF). The 20.2% PVP solution was added dropwise to the hydroxyapatite powder and was mixed thoroughly; a total of 0.56 g of 20.2% PVP solution was added per gram of hydroxyapatite powder. The granulated hydroxyapatite powder was dried using a vacuum oven manufactured by Precision Scientific Incorporated (Chicago, IL) and was then ground with mortar and pestle. The same procedure was used to granulate the tricalcium phosphate powder.

2. Compaction of powders

A laboratory press, Model C, manufactured by Fred S. Carver Incorporated (Menomonee Falls, WI) was used to compress the dried granulated powder into disks using a die (12.54 cm ID) manufactured by the University of Wisconsin-Madison Physics Department machine shop. The disks were prepared by compacting 0.50 g of granulated powder. A compaction load of 4.0 metric tons was used unless otherwise stated.

3. Prefiring of disks

The disks were prefired in a Lindberg Type 51848 furnace (Watertown, WI) to oxidize the polyvinylpyrrolidone and other organic materials present. The prefiring schedule is given in Table I.

4. Preparation of microporous disks

The disks were sintered in a Lindberg Type 51314 box furnace equipped with a Lindberg Type 59246 control console. The sintering schedule is provided in Table II. Sintering temperatures varied between 900 and 1300° C; sintering times varied between 1 and 12 hours.

Table I. Prefiring schedule for ceramic disks.

Step	Temperature / °C	Time / min
1	120	30
2	240	30
3	360	30
4	480	30
5	600	30
6[a]	720	60

[a]Following step 6, the disks were allowed to cool to room temperature.

Table II. Sintering schedule for ceramic disks.

Step	Temperature / °C	Time / min
1	240	30
2	480	30
3	720	30
4	[a]	[a]
5[b]	720	30

[a]The disks were fired for 1 to 12 hours at a sintering temperature ranging from 900 to 1200 °C.

[b]Following step 5, the disks were allowed to cool to room temperature.

5. Preparation of macroporous disks

Various amounts of poly(vinyl stearate), PVS, powder (Aldrich) were mixed with dried granulated hydroxyapatite powder. The powder was compressed and the disks were prefired and sintered using the above procedures.

6. Scanning electron microscopy of sintered disks

Scanning electron microscopy (SEM) was performed on microporous hydroxyapatite and β-whitlockite disks using an S-900 low voltage scanning electron microscope (Hitachi Instruments Incorporated; Tokyo, Japan). Prior to viewing, all disks were sputtered with 1 to 2 nm of platinum using an Ion Tech microsputter (Teddington, England).

7. Mercury porosimetry

Intrusion mercury porosimetry analysis was performed using a Quantachrome Autoscan - 500 porosimeter interfaced with an APC IV advanced personal computer (NEC Information Systems, Incorporated; Boxborough, MA).

C. Characterization of disks

1. Porosity of sintered disks

The ceramic disks were weighed to the nearest 0.1 mg using a Mettler Instrument Corporation (Highstown, NJ) analytical balance. The diameter and thickness of each disk were measured with vernier calipers manufactured by the Mitutoyo Corporation (Japan) with an accuracy of 0.02 mm. The volume and density, ρ, of each disk were then calculated. The porosity, ϕ, of each disk was calculated

$$\phi \equiv 1 - \frac{\rho}{\rho_{theory}} \tag{13}$$

where ρ_{theory} is the theoretical powder density (*62*).

2. Pycnometry

The density of each lot of disks was determined using helium pycnometry and liquid pycnometry. Helium pycnometry experiments were performed using a Quantachrome multipycnometer, model MVP-1.

Liquid pycnometry experiments were performed following a conventional procedure (*63*) using specific gravity bottles (Kimble Glass Company; Toledo, OH). The bottles, containing 14 to 16 ceramic disks from the same lot, were

filled with distilled deionized water, sonicated, and placed in a constant temperature water bath (Haake Buchler Instruments, Inc.; Saddle Brook, NJ) at 25 °C. After equilibrium was reached, the bottles were removed from the bath, were allowed to cool to room temperature, and were weighed.

Since the weight of the dry bottle and the ceramic disks are known, the weight and volume of the added water can be calculated; the volume and density of the ceramic disks can then be determined. The procedure was repeated using HPLC grade methanol (Baxter Burdick and Jackson; Muskegon, MI).

3. Volume fraction isolated and Volume fraction accessible

Volume fraction isolated ϕ^i can be calculated using the following equation

$$\phi^i = (1 - \phi)\left(\frac{\rho_{theory}}{\rho_{pyc}} - 1\right) \qquad (14)$$

The derivation of eq 14 is given in Appendix A. Since the sum of volume fraction isolated and volume fraction accessible ϕ^a must equal the total porosity, volume

fraction accessible can be calculated

$$\phi^a = \phi - \phi^i \qquad (15)$$

4. Stokes diaphragm cell

Construction. The bulk diffusion coefficients for benzoic acid through porous hydroxyapatite disks were determined using a Stokes diaphragm cell. The cells were constructed in a two step process. First, a ceramic disk was placed in a Lucite® L cast acrylic housing unit (E. I. Du Pont de Nemours and Company; Wilmington, DE) The holder, which consisted of two symmetric halves, was held together with Torr Seal® base resin and hardener (Varian Associates; Lexington, MA). Care was taken to avoid contact between the Torr Seal® adhesives and the exposed portion of the hydroxyapatite disk. Since a water tight seal was essential, the housing unit was placed in a vice to allow the adhesive to set and cure completely. Figure 11 shows the top, bottom, and side views of one of the symmetric halves of the acrylic housing unit; Figure 12 gives a schematic view of the complete acrylic housing unit containing a hydroxyapatite disk.

The second step in the construction of the diaphragm cell was to attach the half-cells to the acrylic housing

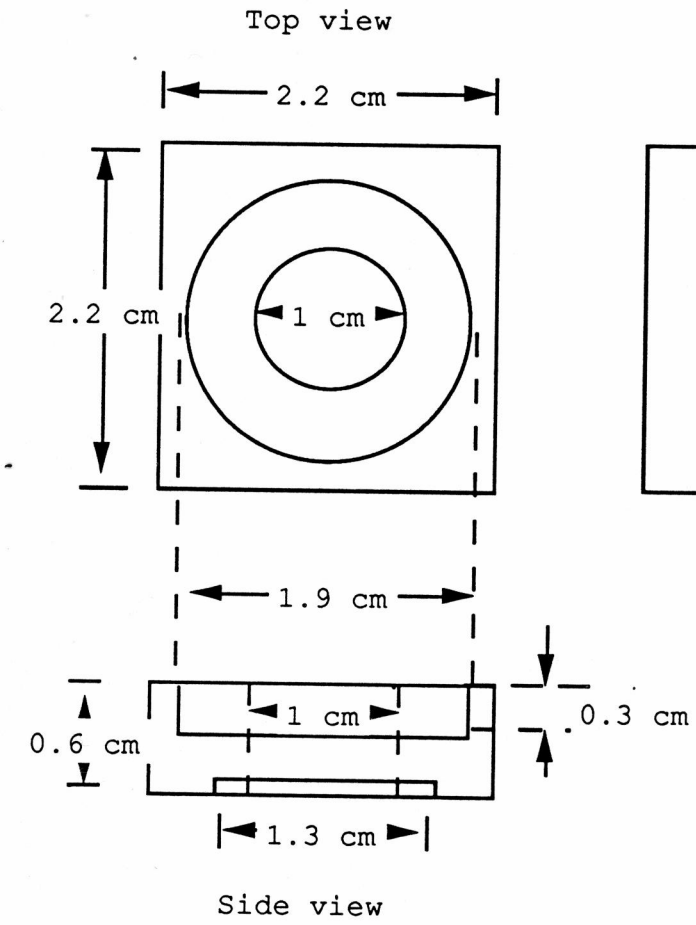

Figure 11. Top, bottom, amd side views of a symmetric half of the acrylic membrane housing unit.

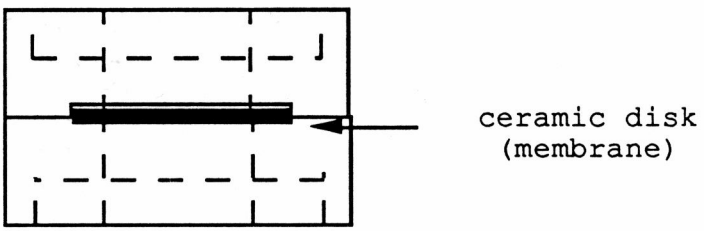

Figure 12. Assembled membrane housing unit.

unit. Ground standard taper 14/35 Pyrex® outer joints (Corning Glass Works; Corning, NY) were attached to the top and bottom of the acrylic housing unit with the Torr Seal® adhesives. Again the adhesive was allowed to set and cure for 24 hours. Figure 13 gives a schematic view of the completed diaphragm cell.

Preparation of solutions. Two diffusion experiments were performed. In the first experiment, the flux of benzoic acid was in the downward direction; the flux of benzoic acid was in the upward direction in the second experiment. The donor and receiver cell solutions contained 4-fluorobenzoic acid (99% purity) and Propyl 4-hydroxybenzoate (99+%) (*64*) obtained from Aldrich, and potassium phosphate dibasic anhydrous (K_2HPO_4, ACS certified) and potassium phosphate monobasic (KH_2PO_4, ACS crystals) obtained from Columbus Chemical Industries Incorporated (Columbus, WI) and Fisher Scientific Company (Fair Lawn, NJ), respectively. The donor half-cell also contained benzoic acid (99+% gold label, ACS reagent grade) obtained from Aldrich. The concentrations of solution components are listed in Table III. All solutions were degassed by sonication prior to use.

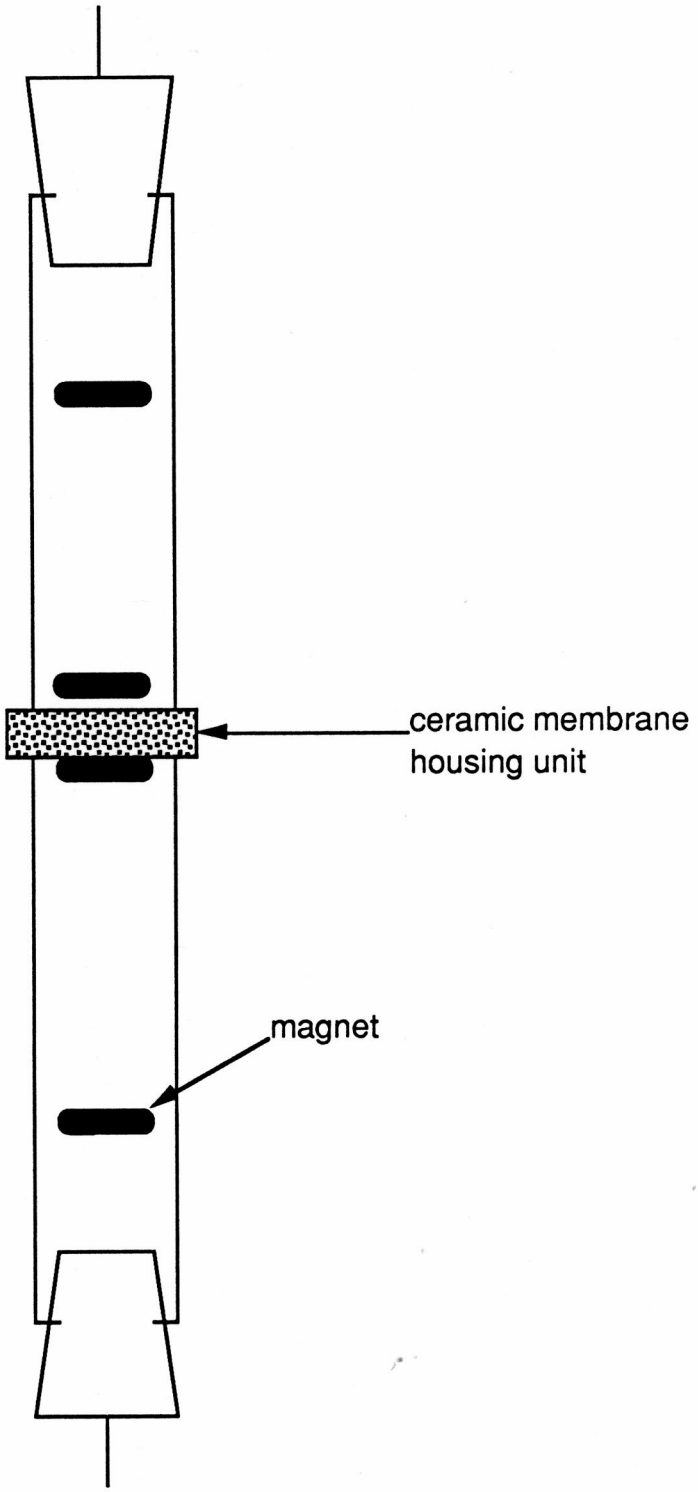

Figure 13. Stokes diaphragm cell.

Table III. Concentration of donor and receiver half-cell solution components.

Compound	Concentration / mol dm^{-3}	
	Experiment 1	Experiment 2
4-fluorobenzoic acid	0.00178	0.000448
benzoic acid[a]	0.00204	0.00205
Propyl 4-hydroxybenzoate	0.00140	0.00140
K_2HPO_4	0.0250	0.0250
KH_2PO_4	0.0250	0.0250

[a]Benzoic acid was only present in the donor half-cell solution.

Diffusion experiments. With the diaphragm cell in an upright position (the donor half-cell lower than the receiver half-cell), the blank solution was added to the receiver half-cell and was allowed to enter the pores of the hydroxyapatite membrane. After 12 hours, the receiver half-cell was completely filled with blank solution and stoppered in such a manner that no air remained in the half-cell. In the first experiment, the diaphragm cell was inverted, and exactly 15.00 ml of benzoate solution was added to the donor half-cell. In the second experiment, the cell was inverted only to add the benzoate solution, which completely filled the donor half-cell, and then was returned to its original position. Two magnets were placed in each half-cell. One magnet was placed close to the hydroxyapatite membrane, in order to minimize potential boundary layer effects, and the other magnet was positioned in the center of the half cell. See Figure 13. The cells were rotated at approximately 100 rotations per minute using a T Line Laboratory Stirrer, Model 134-1 (Talboys Engineering Corporation; Emerson, NJ). Three Alnico 5 maximum pull horseshoe magnets were placed alongside the diaphragm cell to hold the small magnets inside the cell in their proper positions. See Figure 14. The diffusion

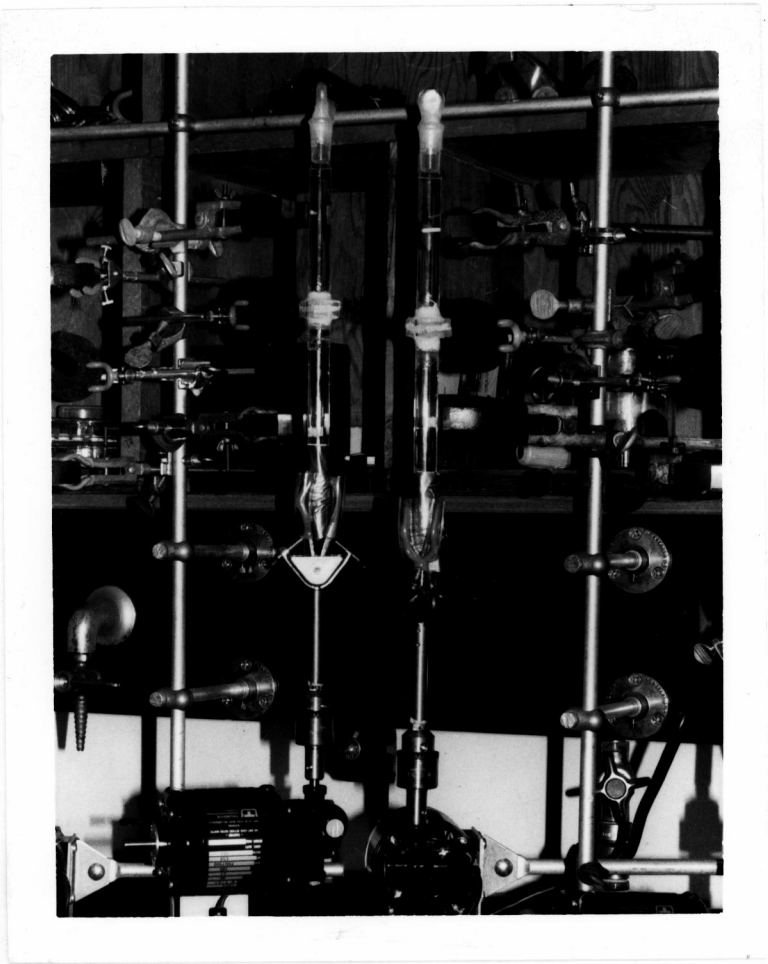

Figure 14. Photograph of Stokes diffusion cells.

experiments were carried out at ambient temperature (24.5 ± 0.5 °C).

The concentration of benzoic acid in the upper half cell was monitored using high performance liquid chromatography (HPLC). By knowing the volume of solution in each half cell, the benzoic acid concentration in the lower half cell was calculated from a mass balance relationship.

It can be shown (See Appendix B.) that the following relationship exists,

$$\ln\left[\frac{(C_d - C_r)}{C_d^o}\right] = -D_B \beta t \qquad (16)$$

where C_d is the concentration of benzoic acid in the donor half cell at time t, C_r is the concentration of benzoic acid in the donor half cell at time t, C_d^o is the concentration of benzoic acid in the donor half cell at time t = 0, and D_B is the bulk diffusion coefficient of benzoic acid through the membrane. The cell constant β is defined as

$$\beta = \frac{A}{\delta}\left(\frac{1}{V_d} + \frac{1}{V_r}\right) \qquad (17)$$

where V_d is the volume of donor cell solution, V_r is the volume of receiver cell solution, A is the area of the membrane exposed to the solution, and δ is the thickness of the membrane. The derivation of eq 16 and 17 are provided in Appendix B.

5. HPLC assay

The isocratic HPLC system consisted of a model 110A solvent delivery module, a model 163 variable wavelength absorbance detector, and an Altex® 210 injector equipped with a 50 ml loop (Experiment 1) or a 250 ml loop (Experiment 2), all from Beckman Instruments, Incorporated (San Ramon CA), a Kipp and Zonen model BD 40 chart recorder (Delft, Holland), and a 4.6 X 150 mm octadecylsilane column from Beckman with average particle diameter of 5 μm. Analysis was performed at 254 nm.

The mobile phase consisted of 45% HPLC grade methanol (Baxter Burdick and Jackson), 1% acetic acid (99.7% purity, ACS reagent grade, Aldrich) and 54% distilled deionized water. The flow rate was 1.0 ml min^{-1}.

In the first diffusion experiment, the donor cell solution was used as the benzoic acid standard solution. In the second experiment, the standard contained benzoic acid diluted with blank solution, giving a final benzoic

acid concentration of 0.001032 mol dm^{-3}. The 4-fluorobenzoic acid present in each benzoic acid standard solution served as an internal standard for the HPLC analysis.

At the time of the analyses, approximately 0.15 ml of solution was removed (without replacement) from the upper half-cell of the Stokes diaphragm cell and was diluted with approximately 1 ml of mobile phase. In Experiment 1, the benzoic acid standard was diluted in a similar manner; no dilution was needed for the benzoic acid standard used in Experiment 2. The standard was injected in duplicate at the beginning and at the end of each analysis. Samples were also injected in duplicate. The benzoic acid concentration in the samples was determined by comparing the benzoic acid:4-fluorobenzoic acid peak height ratio to that of the standard.

III. RESULTS

A. Characterization of powders

1. Particle size distribution

The percent undersize particle size distribution of the hydroxyapatite and tricalcium phosphate powders is given in Tables IV and V. Log-probability plots of the two distributions (Figure 15) gave straight lines, indicating that both powders were log-normally distributed (*65*). The average particle size was 67 μm (log σ = 0.39; N = 225) for hydroxyapatite and 38 μm (log σ = 0.30; N = 225) for tricalcium phosphate.

2. Elemental analysis

The results of the inductively coupled plasma-atomic emission spectrometry analysis of the hydroxyapatite and tricalcium phosphate powders are shown in Table VI.

3. Powder density as a function of temperature

The densities of hydroxyapatite and tricalcium phosphate powders, heated to different temperatures, are listed in Table VII. The density of hydroxyapatite began to increase at 500 °C, due to the release of water

Table IV. Percent undersize particle-size distribution for hydroxyapatite powder.

Particle diameter / μm	Percent undersize
15	0.0
25	13.3
50	38.7
75	54.7
100	65.3
125	76.0
150	82.7
175	90.2
200	96.9
250	100.0

Table V. Percent undersize particle-size distribution for tricalcium phosphate powder.

Particle diameter / μm	Percent undersize
10	0.0
20	18.2
40	52.0
60	72.9
80	84.4
100	92.0
120	94.7
140	96.4
160	97.3
180	98.7
200	99.6
250	100.0

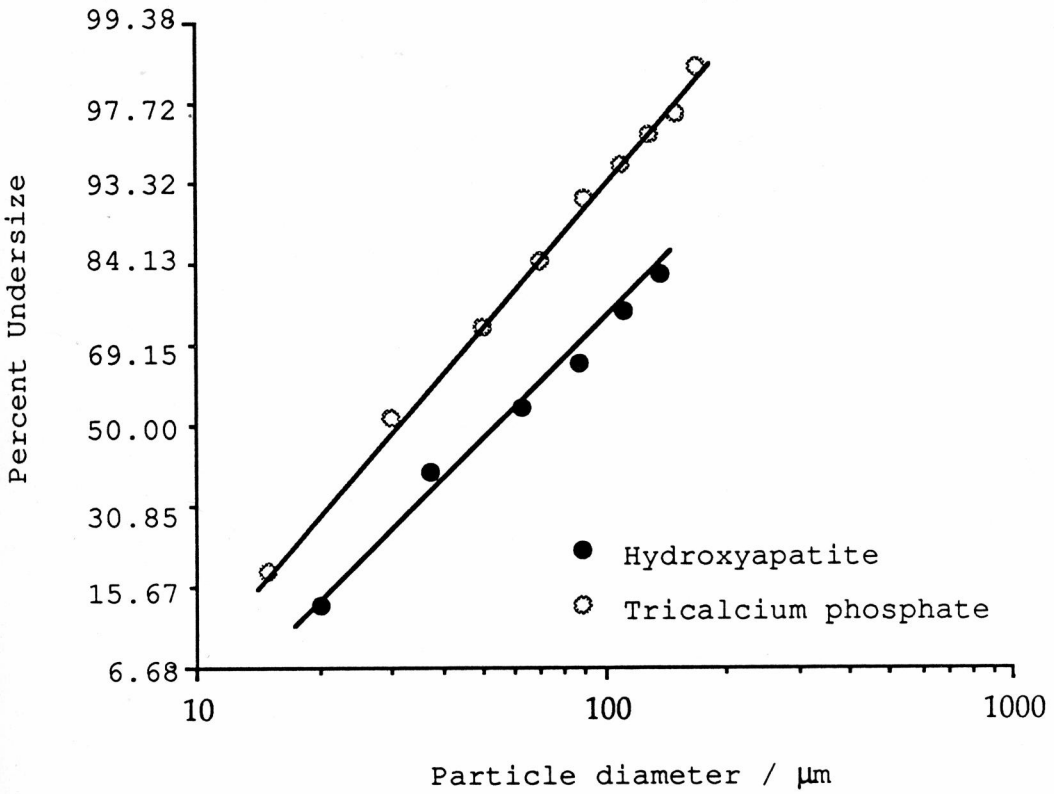

Figure 15. Log-probability plots of percent undersize particle-size distributions of hydroxyapatite and tricalcium phosphate powders. Data are from Tables IV and V.

Table VI. Trace elements present in hydroxyapatite and tricalcium phosphate powders determined by inductively coupled plasma-atomic emission spectrometry.

	Concentration / ppm	
Element	Hydroxyapatite	Tricalcium phosphate
Magnesium	3400	1460
Sodium	1280	< 200
Aluminum	520	320
Barium	< 10	< 10
Iron	400	200
Strontium	165	293
Copper	< 5	< 5
Zinc	18.3	< 4
Manganese	15.2	76.2
Chromium	14.4	10
Potassium	< 1000	< 1000

Table VII. Pycnometric densities of preheated hydroxyapatite and tricalcium phosphate powders.

Temperature / °C	Density / g cm^{-3} Hydroxyapatite	Tricalcium phosphate
25	2.97_3 (0.03_0)[a]	2.97_2 (0.01_7)
105	2.97_8 (0.01_8)	3.02_9 (0.03_5)
200	2.97_7 (0.01_5)	3.02_4 (0.01_5)
300	2.99_7 (0.01_3)	3.02_3 (0.02_0)
400	2.97_9 (0.01_4)	3.02_3 (0.01_5)
500	2.95_3 (0.01_1)	3.03_1 (0.01_5)
600	3.01_8 (0.02_1)	3.02_2 (0.02_3)
700	3.02_6 (0.01_3)	3.03_1 (0.01_5)
800	3.14_5 (0.01_8)	3.04_7 (0.01_4)
900	3.18_9 (0.02_1)	3.03_5 (0.02_1)
1000	3.16_0 (0.01_4)	3.03_9 (0.01_1)
1100	3.17_4 (0.01_6)	3.02_7 (0.01_2)
1200	3.17_5 (0.01_4)	3.02_4 (0.01_2)
1300	3.14_9 (0.02_8)	3.03_6 (0.01_0)

[a] ($P = 0.05$; $N = 8$)

molecules from the crystal lattice (*32*), and approached the theoretical density (*38*) of 3.16 g cm^{-3} at temperatures above 800 °C. The density of tricalcium phosphate powder increased initially, as a function of temperature. At temperatures above 100 °C, the density remained constant (3.04 g cm^{-3}). Failure to approach the theoretical density was presumably caused by the presence of intraparticle pores (*66*). A plot of the data in Table VII is provided in Figure 16.

4. X-ray diffraction of heated powders

X-ray diffraction patterns of the hydroxyapatite and tricalcium phosphate powders, preheated at temperatures up to 1300 °C, were obtained and compared with JCDPS mineral data base (*61*) in order to identify the calcium phosphate polymorphs present.

The tricalcium phosphate powder preheated to temperatures below 600 °C gave spectra characteristic of calcium phosphate hydrate, $Ca_3(PO_4)_2 \cdot x\ H_2O$ (*67*) (Figure 17). At temperatures above 800 °C, the water was completely released from the crystal lattice, giving β-whitlockite, β-$Ca_3(PO_4)_2$ (*68*), as the only form of calcium phosphate present (Figure 18). There was no evidence of

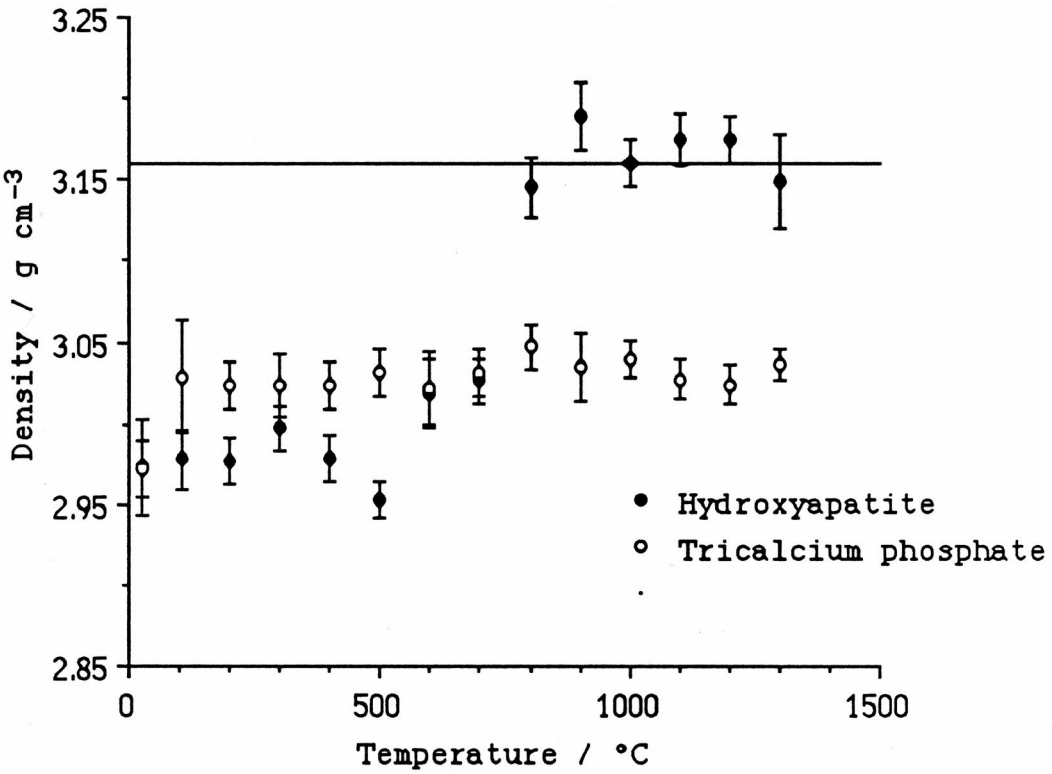

Figure 16. The density of preheated hydroxyapatite and tricalcium phosphate powders as a function of temperature. Data are from Table VII. The error bars represent 95% confidence limits (N = 8). The solid line represents the theoretical density (3.16 g cm^{-3}) of hydroxyapatite and tricalcium phosphate powders (*38*).

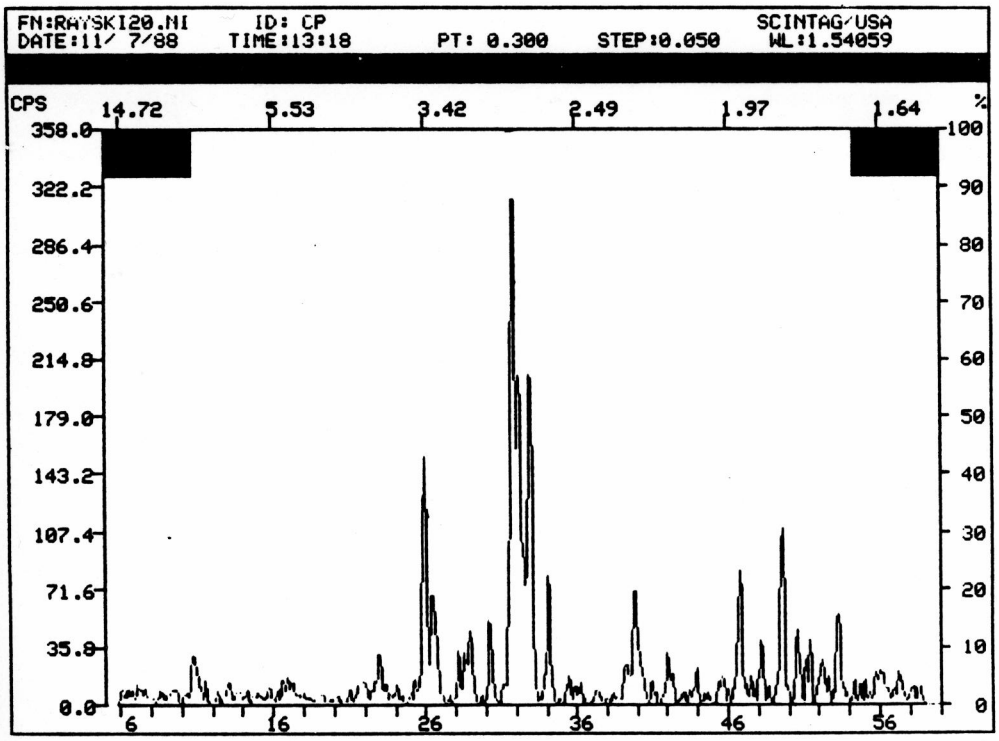

Figure 17. X-ray diffraction spectrum of tricalcium phosphate powder.

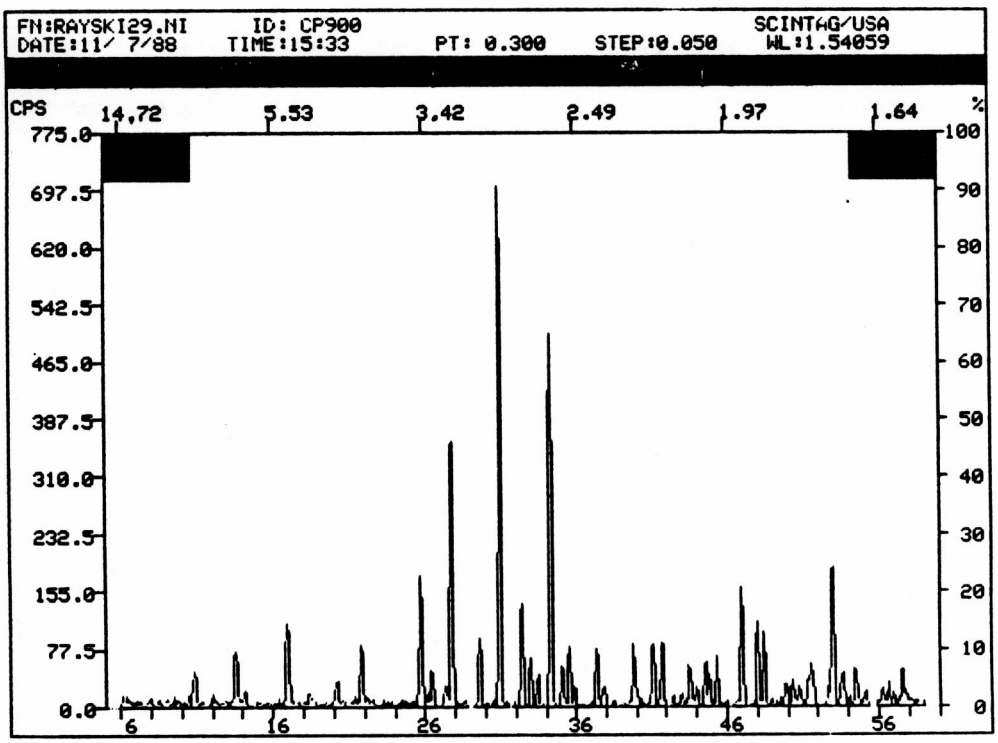

Figure 18. X-ray diffraction spectrum of tricalcium phosphate powder preheated to 900 °C showing the β-whitlockite pattern.

degradation of the β-whitlockite to α-whitlockite, α-$Ca_3(PO_4)_2$ at temperatures above 1200 °C.

The hydroxyapatite powder, at all temperatures, gave only diffraction peaks characteristic of an apatite structure (*69*) (Figures 19 and 20), even though release of lattice water did occur. It has been reported that hydroxyapatite can lose up to 75% of its lattice water without losing the apatite structure (*32*). At temperatures above 1100 °C, hydroxyapatite can decompose to β-whitlockite; this was not detected in any of the samples.

5. Differential scanning calorimetry

Differential scanning calorimetry was performed on hydroxyapatite and tricalcium phosphate powders, scanning a temperature range of 50 to 600 °C. Thermograms (Figures 21 and 22) of both powders show the loss of lattice water at temperatures above 460 °C.

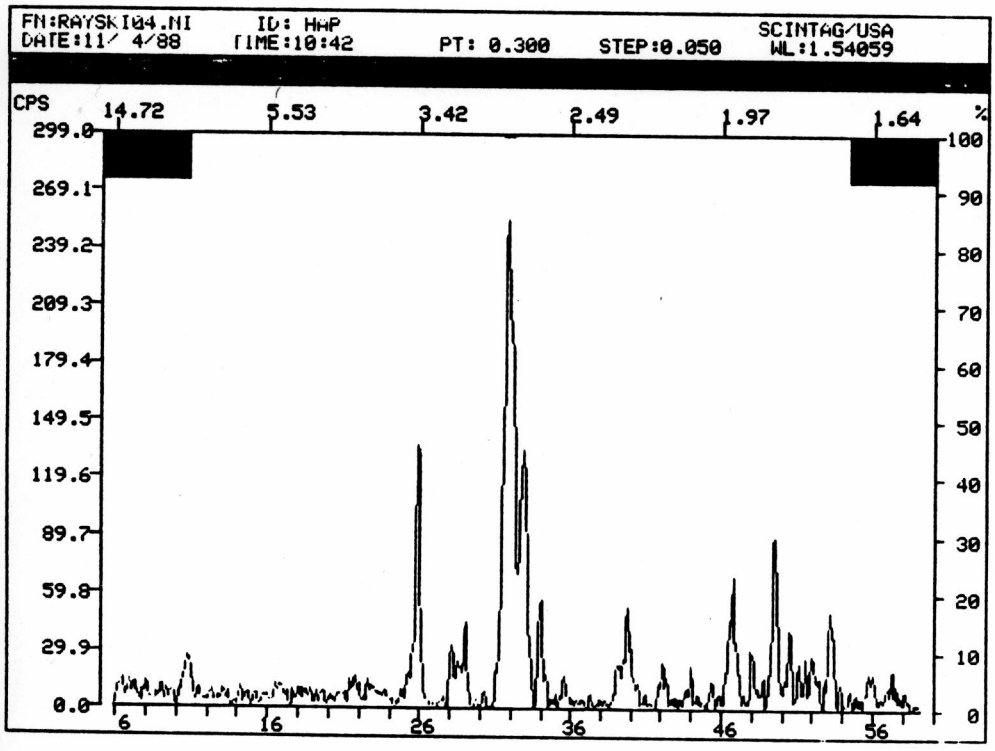

Figure 19. X-ray diffraction spectrum of hydroxyapatite powder.

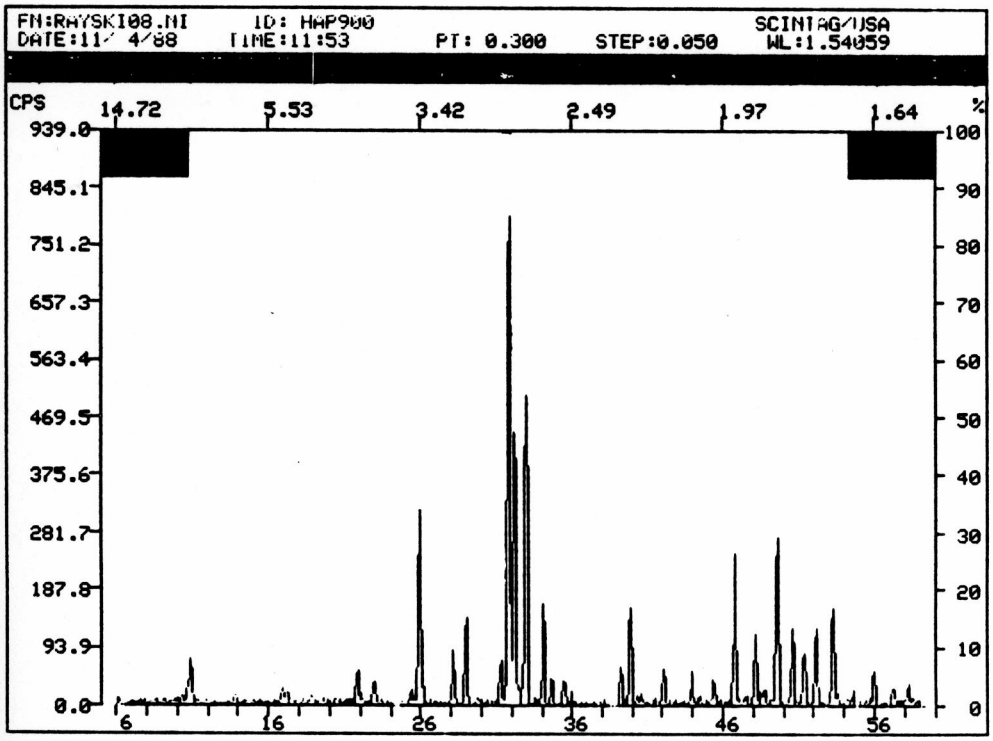

Figure 20. X-ray diffraction spectrum of hydroxyapatite powder preheated to 900 °C.

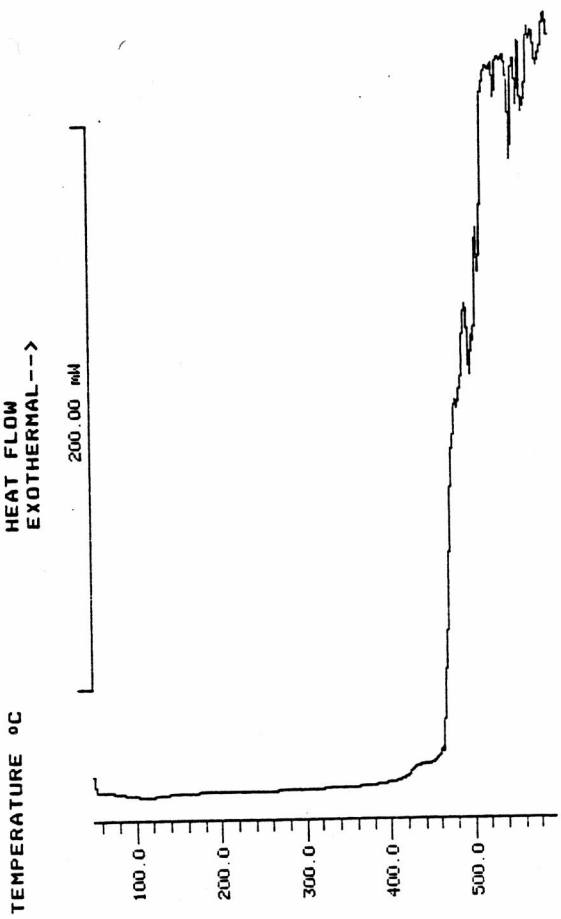

Figure 21. Thermogram of hydroxyapatite powder.

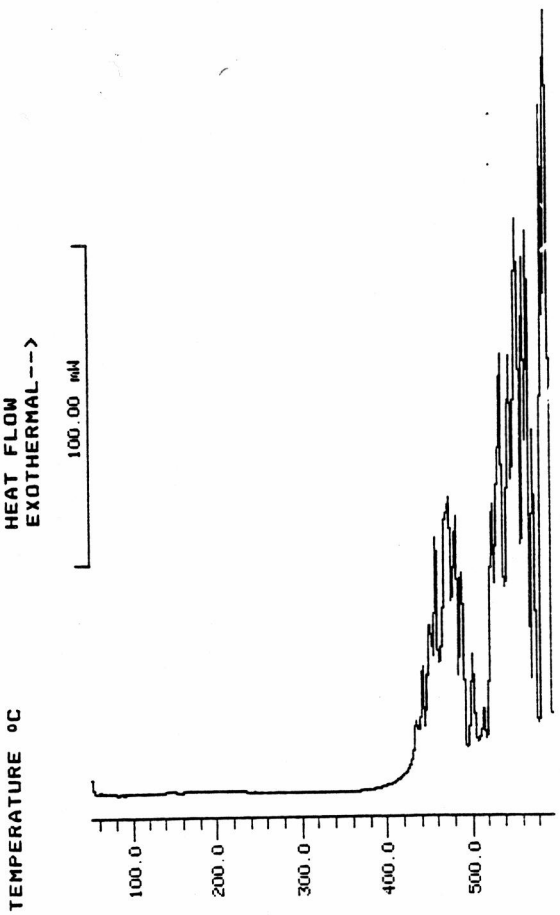

Figure 22. Thermogram of tricalcium phosphate powder.

B. Characterization of disks

1. Porosity of sintered disks as a function of manufacturing variables

The manufacturing process greatly affects the porosity of hydroxyapatite and β-whitlockite disks. One of the goals of this research was to prepare ceramic disks of known porosity, by controlling the fabrication process. Five variables were studied: (1) the amount of polyvinyl-pyrrolidine used in the granulation process, (2) the applied load used to compress the powder into a disk, (3) the amount of organic burnout material added to the granulated ceramic powder, (4) the sintering temperature, and (5) the sintering time.

Amount of granulating material. In a preliminary experiment, the amount of PVP used to granulate the ceramic powders was varied from 0 to 60% (w/w). The powder was dried and compressed into disks with an applied load of 4.0 metric tons (39.2 kN). The disks were sintered at 1050 and 1100 °C. Hydroxyapatite disks that contained greater than 30% PVP cracked during sintering. The β-whitlockite disks were even more susceptible to cracking during firing.

The porosity of hydroxyapatite and β-whitlockite disks as a function of the amount of PVP used in the granulation

process is given in Tables VIII and IX, respectively. Figures 23 and 24 show these data graphically. Both plots show that porosity of the hydroxyapatite and β-whitlockite disks increased as the amount of PVP increased. Also, a temperature effect is shown. As the temperature was increased from 1050 °C to 1100 °C, the porosity of both the hydroxyapatite and β-whitlockite disks decreasd. A PVP concentration of 10% (w/w) gave optimum powder handling conditions, thus this concentration was used in all subsequent studies.

Compaction pressure. The porosity of hydroxyapatite and β-whitlockite disks decreased as the compaction force increased (Tables X and XI). Figures 25 and 26 show that as the compaction force reached 39.2 kN (4 metric tons), the change in the disks' porosity approached zero. Since a large compaction force caused radial cracking to occur in the sintered disks, an applied load of 4.0 metric tons was used to manufacture the ceramic disks.

Amount of added burnout material. Poly(vinyl stearate), PVS, was added to dried granulated hydroxyapatite prior to compaction. The PVS was oxidized and burned out during prefiring, leaving apparent macropores in the green hydroxyapatite disk. The green

Table VIII. Porosity of hydroxyapatite disks as a function of granulation material.

Sintering temperature / °C	Percent PVP (w/w)	Number of disks	Porosity
1100[a]	0	3	0.310 (0.007)[b]
	5	3	0.315 (0.005)
	10	4	0.335 (0.007)
	20	3	0.376 (0.002)
	30	3	0.421 (0.015)
1050[a]	0	1	0.318
	5	5	0.374 (0.017)
	10	3	0.396 (0.025)
	20	5	0.451 (0.022)
	30	3	0.482 (0.036)

[a]The disks were sintered for 6 hours.

[b]Standard deviations are shown in parentheses.

Table IX. Porosity of β-whitlockite disks as a function of granulation material.

Sintering temperature / °C	Percent PVP (w/w)	Number of disks	Porosity
1100[a]	0	4	0.112 (0.005)[b]
	5	4	0.119 (0.006)
	10	3	0.132 (0.003)
1050[a]	0	4	0.185 (0.025)
	5	4	0.174 (0.005)
	10	3	0.214 (0.009)

[a]The disks were sintered for 6 hours.

[b]Standard deviations are shown in parentheses.

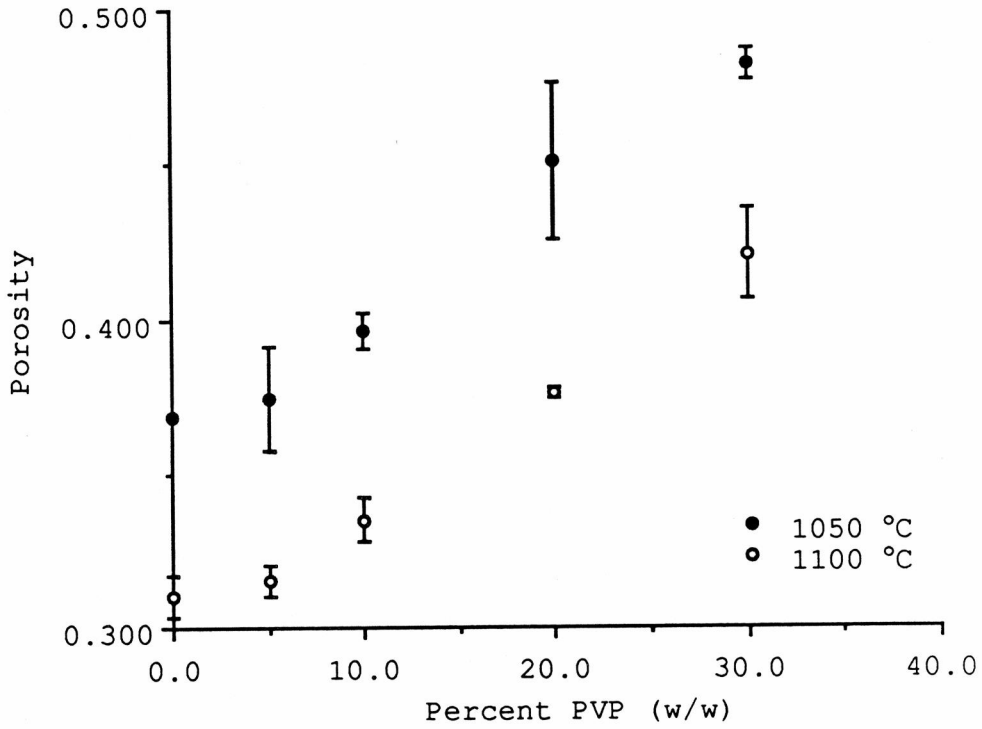

Figure 23. Porosity of hydroxyapatite disks as a function of the amount of PVP used in the granulation process. The disks were sintered for 6 hours. Data are from Table VIII.

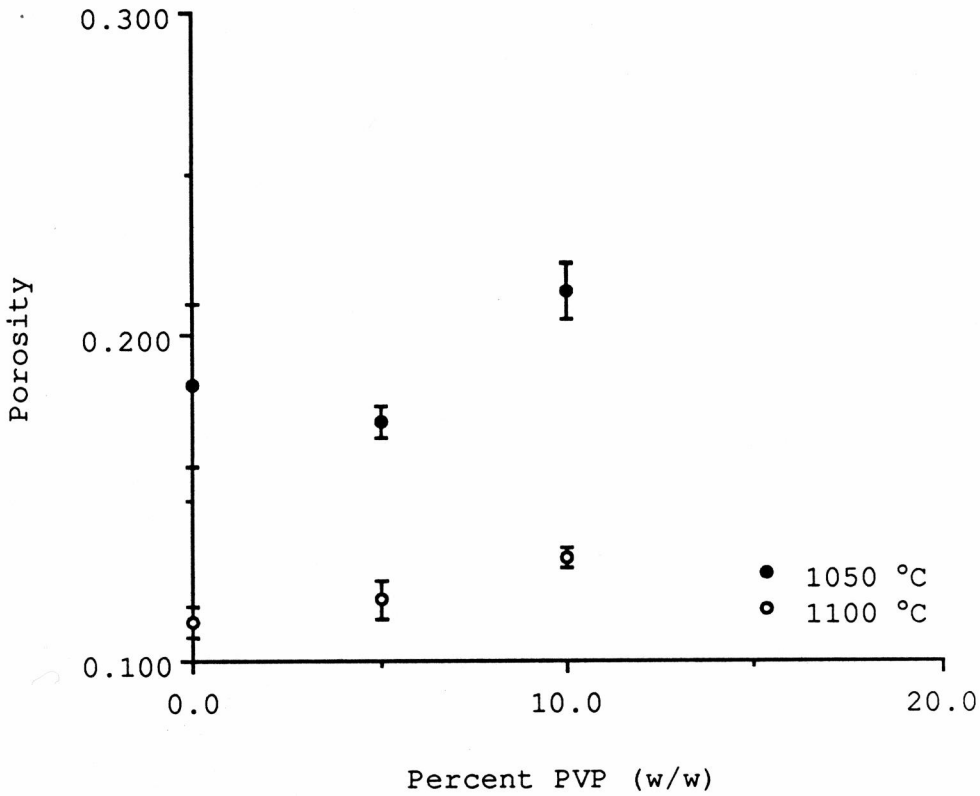

Figure 24. Porosity of β-whitlockite disks as a function of the amount of PVP used in the granulation process. The disks were sintered for 6 hours. Data are from Table IX.

Table X. Porosity of hydroxyapatite disks as a function of compaction force.

Sintering temperature / °C	Force / kN	Number of disks	Porosity
1000[a]	9.8	6	0.528 (0.008)[b]
	19.6	6	0.449 (0.009)
	29.4	6	0.40 (0.01)
	39.2	5	0.27 (0.01)
	49.0	6	0.23 (0.02)
	58.8	3	0.176 (0.005)
1100[a]	9.8	5	0.27 (0.01)
	19.6	6	0.21 (0.01)
	29.4	5	0.17 (0.02)
	39.2	6	0.16 (0.02)
	49.0	5	0.15 (0.02)
	58.8	3	0.14 (0.02)

[a]The disks were sintered for 3 hours.

[b]95% confidence limits are shown in parentheses.

Table XI. Porosity of β-whitlockite disks as a function of compaction force.

Sintering temperature / °C	Force / kN	Number of disks	Porosity
1000[a]	9.8	6	0.547 (0.007)[b]
	19.6	6	0.479 (0.007)
	29.4	5	0.45 (0.01)
	39.2	5	0.40 (0.02)
	49.0	5	0.39 (0.01)
	58.8	3	0.38 (0.01)
1100[a]	9.8	6	0.315 (0.009)
	19.6	6	0.27 (0.01)
	29.4	6	0.26 (0.01)
	39.2	5	0.26 (0.02)
	49.0	6	0.262 (0.008)
	58.8	3	0.25 (0.02)

[a]The disks were sintered for 3 hours.

[b]95% confidence limits are shown in parentheses.

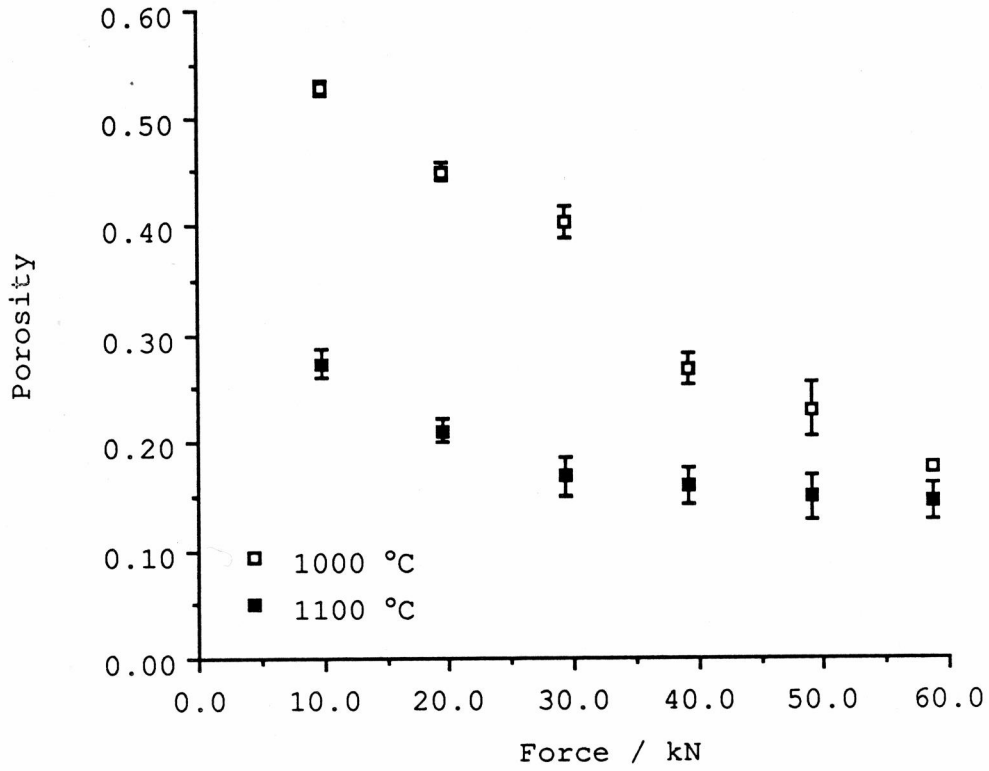

Figure 25. Porosity of hydroxyapatite disks sintered for 3 hours as a function of compaction force. Data are from Table X.

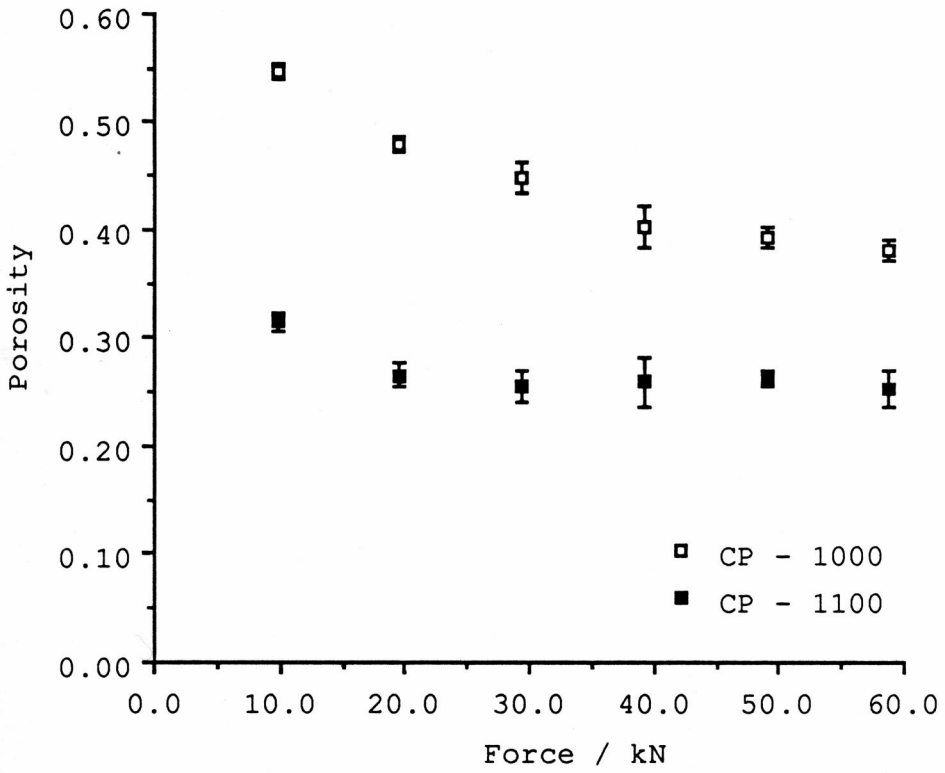

Figure 26. Porosity of β-whitlockite disks sintered for 3 hours as a function of compaction force. Data are from Table XI.

disks were sintered at 1000 and 1100 °C. The porosity of the disks greatly increased as the amount of PVS increased (Table XII). A temperature effect was also observed (Figure 27).

Sintering time and temperature. The most effective method to control the porosity of the hydroxyapatite and β-whitlockite disks was to varying the sintering temperature. As mentioned previously, the porosity of the disks decreased as the sintering temperature was increased. The porosity of hydroxyapatite and β-whitlockite disks as a function of sintering temperature is listed in Tables XIII and XIV. These data, shown graphically in Figures 28 and 29, show a linear relationship between porosity and temperature between 900 and 1100 °C. Above 1100 °C, the porosity remained constant. In most cases, the porosity of the disks did not vary with respect to sintering time.

2. Mercury porosimetry

At a pressure of 500 psia, mercury was unable to intrude the pores of both the hydroxyapatite and tricalcium phosphate disks, therefore the pores present in the disks are probably less than 0.2 μm in diameter (*70*).

Table XII. Porosity of macroporous hydroxyapatite disks as a function of added poly(vinylstearate) burnout material.

Sintering temperature / °C	Percent PVS (w/w)	Porosity
1100[a]	0	0.25 (0.01)[b]
	10	0.36 (0.02)
	20	0.49 (0.002)
1000[a]	0	0.164 (0.002)
	10	0.29 (0.02)
	20	0.44 (0.02)

[a]The disks were sintered for 1 hour.

[b]Standard deviations are shown in parentheses.

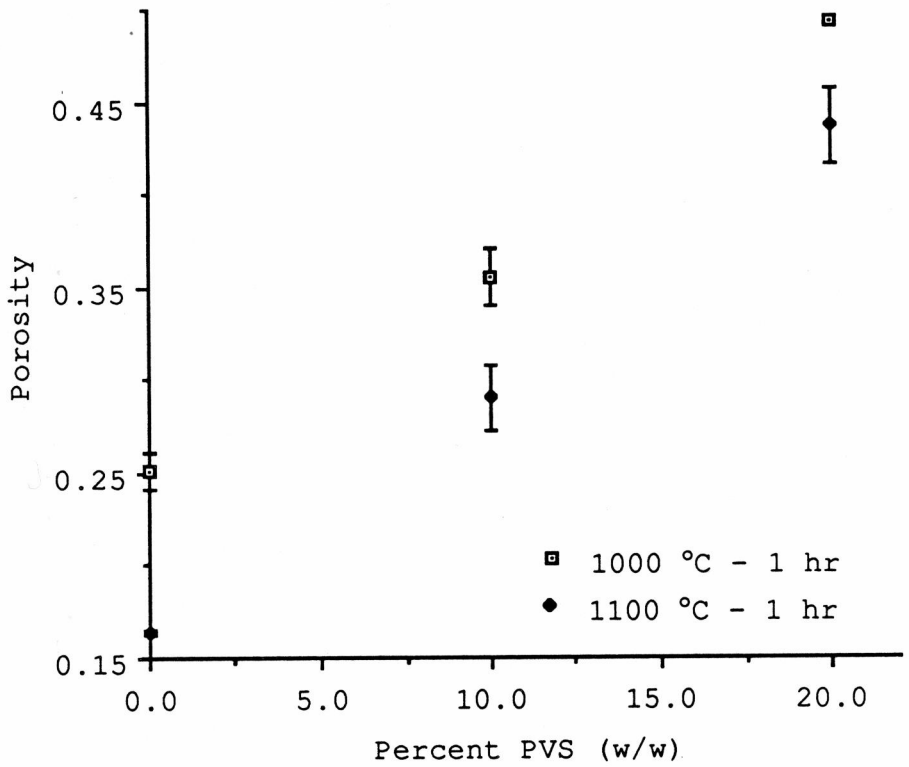

Figure 27. Porosity of hydroxyapatite disks sintered for 1 hour as a function of poly(vinyl stearate) added to dried granulated hydroxyapatite powder. Data are from Table XII.

Table XIII. Porosity of microporous hydroxyapatite disks as a function of sintering time and temperature.[a]

Sintering temperature / °C	Porosity		
	Sintering time		
	3 hours	6 hours	12 hours
900[b]	0.47_8 (0.01_0)[c]		0.45_3 (0.01_1)
925	0.40_6 (0.01_1)		0.45_8 (0.01_1)
950	0.372 (0.008)		0.38_9 (0.01_2)
975	0.36_6 (0.02_0)		0.25_8 (0.02_6)
1000[d]	0.24_5 (0.01_5)	0.25_5 (0.01_5)	0.19_3 (0.01_7)
1025[e]	0.20_3 (0.01_1)	0.19_4 (0.02_3)	0.18_9 (0.01_3)
1050	0.15_1 (0.01_6)	0.15_4 (0.01_7)	0.15_4 (0.01_1)
1075	0.14_5 (0.01_6)	0.12_4 (0.01_6)	0.14_9 (0.01_3)
1100	0.14_3 (0.01_7)	0.11_3 (0.01_2)	0.12_3 (0.01_3)
1200	0.11_5 (0.01_4)		
1300	0.10_4 (0.01_8)		

[a]Compaction load was 4.0 metric tons.
[b]The porosity of "green" hydroxyapatite disks is 0.495 (0.005).
[c]Standard deviations are shown in parentheses.
[d]The porosity of hydroxyapatite disks sintered at 1000 °C for 1 hour is 0.23_9 (0.01_8).
[e]The porosity of hydroxyapatite disks sintered at 1025 °C for 1 hour is 0.19_7 (0.01_2).

Table XIV. Porosity of microporous β-whitlockite disks as a function of sintering time and temperature.[a]

Sintering temperature / °C	Porosity	
	Sintering time	
	3 hours	12 hours
900[b]	0.50_3 (0.01_2)[c]	
925	0.47_6 (0.01_1)	0.496 (0.008)
950		0.41_5 (0.01_5)
975	0.43_5 (0.01_7)	
1000	0.37_3 (0.01_1)	0.37_8 (0.01_3)
1025	0.32_3 (0.02_0)	0.31_7 (0.01_6)
1050	0.24_2 (0.01_1)	0.25_4 (0.01_5)
1075	0.21_6 (0.02_4)	0.17_7 (0.01_7)
1100	0.16_4 (0.01_4)	0.13_5 (0.01_3)
1200	0.14_0 (0.01_2)	
1300	0.12_5 (0.01_4)	

[a]Compaction load was 4.0 metric tons.

[b]The porosity of "green" tricalcium phosphate disks is 0.509 (0.005).

[c]Standard deviations are shown in parentheses.

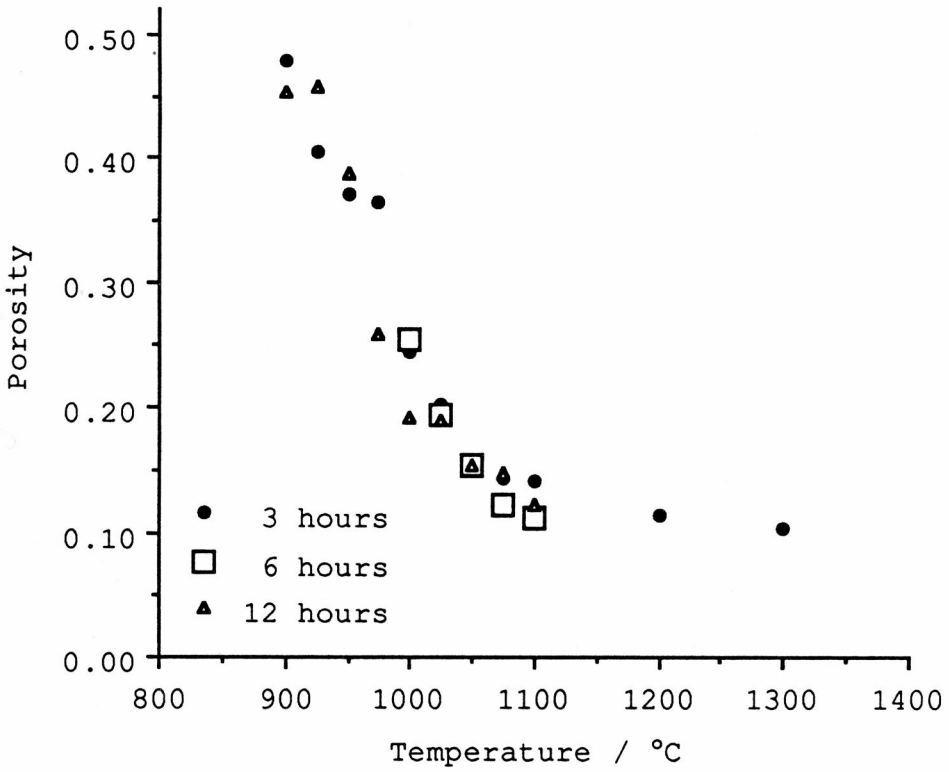

Figure 28. Porosity of microporous hydroxyapatite disks as a function of sintering time and temperature. Data are from Table XIII.

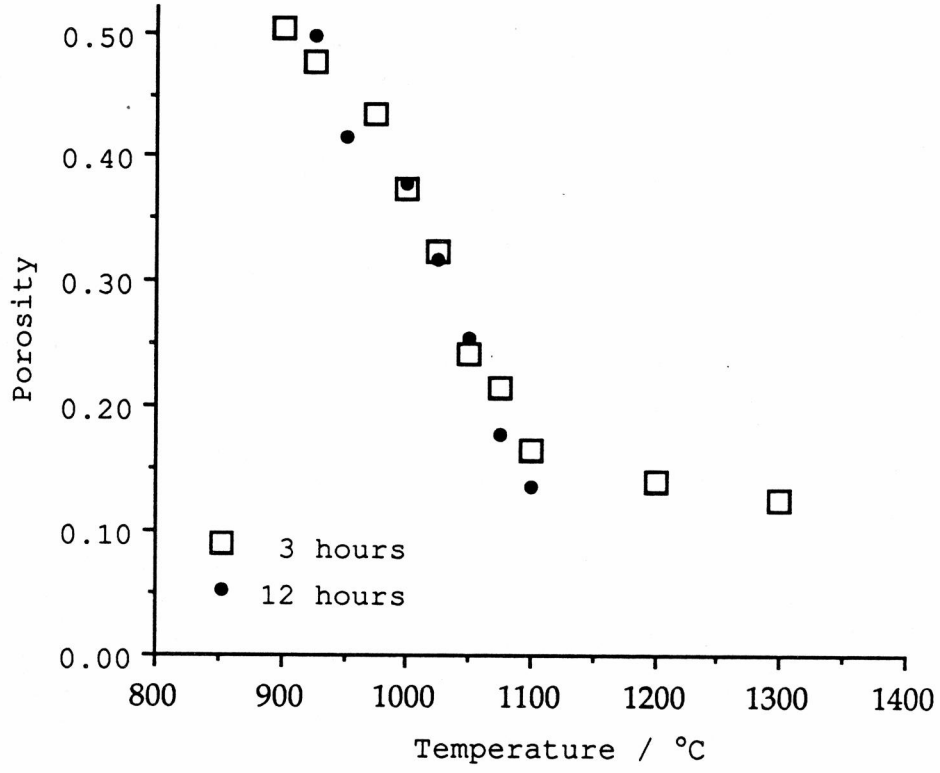

Figure 29. Porosity of microporous β-whitlockite disks as a function of sintering time and temperature. Data are from Table XIV.

3. Scanning electron microscopy

The progressive development of microstructure as a function of sintering temperature is shown in Figures 30 to 35 for hydroxyapatite and Figures 36 to 41 for β-whitlockite. The sintering time was 3 hours for all disks.

Scanning electron microscopy indicates that hydroxyapatite disks sintered at 900 (Figure 31) and 1000 °C (Figure 32) show an increase in both pore and grain size relative to green hydroxyapatite disks (Figure 30). Also a variation in packing was observed. Disks sintered at 1100 °C (Figure 33) have a microstructure which is nearly porefree, with only a few small pores between the large grains. As the temperature increased to 1200 °C (Figure 34), pores on the grain boundaries were slowly eliminated; the ones remaining exist only at the grain corners. As the temperature was raised further to 1300 °C, secondary recrystallization (*26*) occurred. This exaggerated grain growth occurs when a small fraction of grains grows to a large size, consuming the fine-grained matrix. Once a single grain grows to a large size, the curvature of each side increases, and it continues to grow more rapidly than the surrounding smaller grains with fewer sides, thus the driving force for secondary recrystallization is the lower surface energy of the large grain compared with the high

surface energy of the adjacent smaller grains. Figure 35 shows large grains of hydroxyapatite that grew by secondary recrystalization from a fine-grained matrix.

The microstructure of β-whitlockite disks also changed as the sintering temperature was increased. Disks sintered at 900 (Figure 37) and 1000 °C (Figure 38) show an increase in both pore and grain size relative to green tricalcium phosphate disks (Figure 36). Again, variation in packing and pore size was observed. Disks sintered at 1100 (Figure 39) and 1200 °C (Figure 40) have a nearly porefree microstructure. Considerable grain growth occured at 1200 °C. As the temperature was increased to 1300 °C, secondary recrystallization occured (Figure 41).

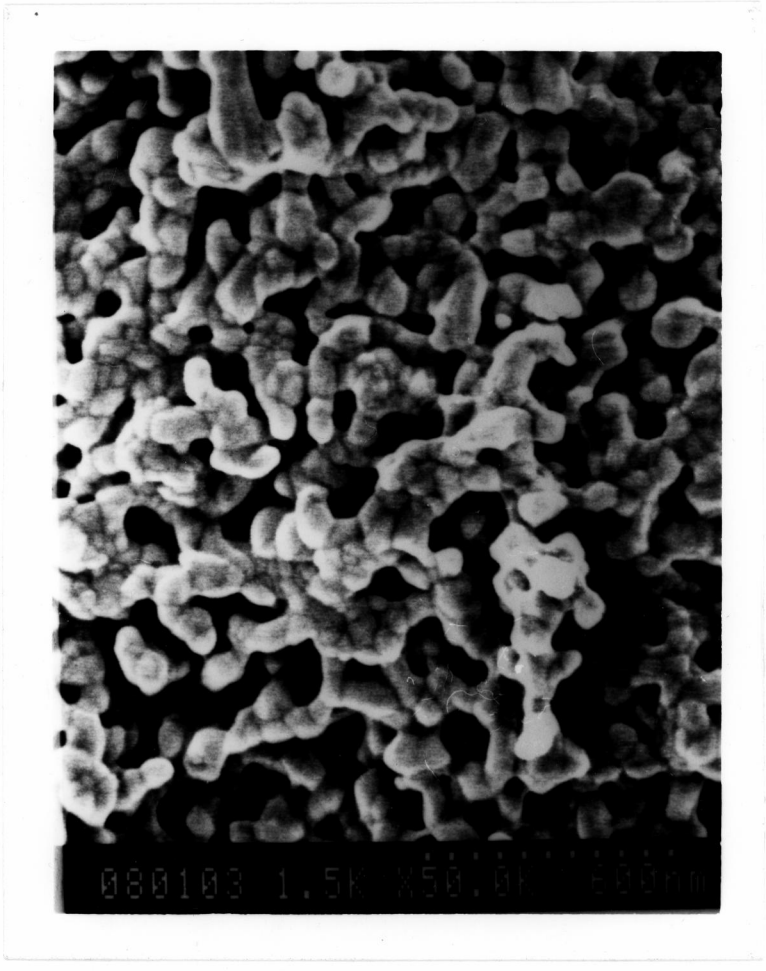

Figure 30. Scanning electron micrograph of a green hydroxyapatite disk prefired at 720 °C (50,000 X).

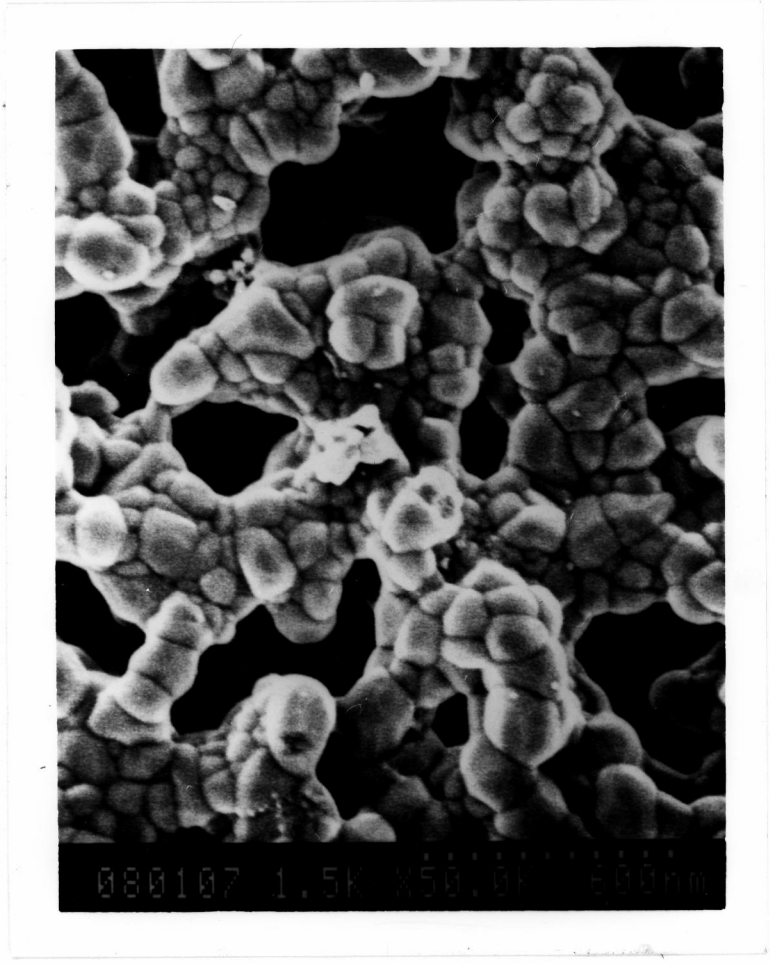

Figure 31. Scanning electron micrograph of a hydroxyapatite disk sintered at 900 °C (50,000 X).

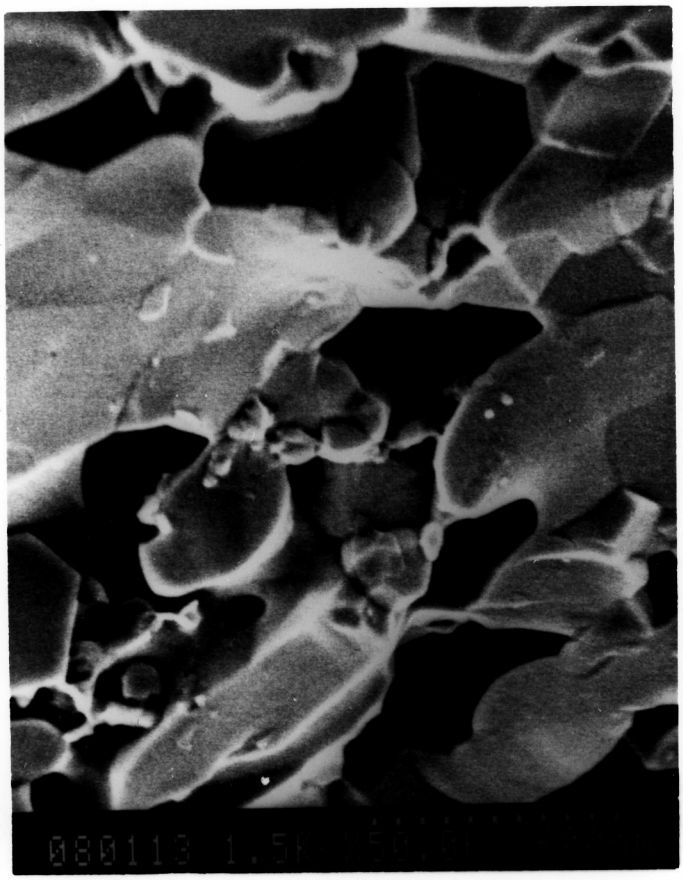

Figure 32. Scanning electron micrograph of a hydroxyapatite disk sintered at 1000 °C (50,000 X).

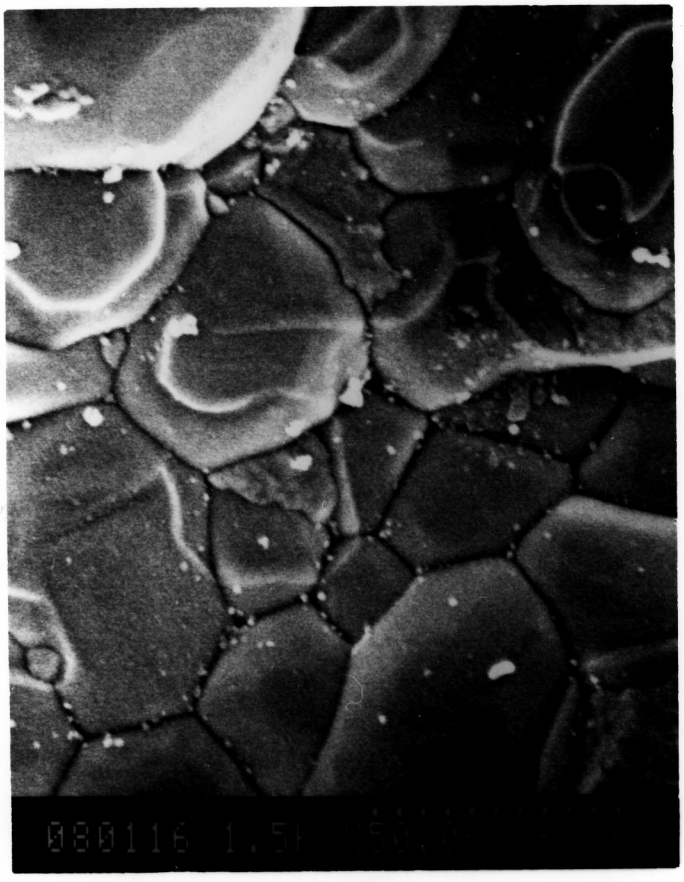

Figure 33. Scanning electron micrograph of a hydroxyapatite disk sintered at 1100 °C (50,000 X).

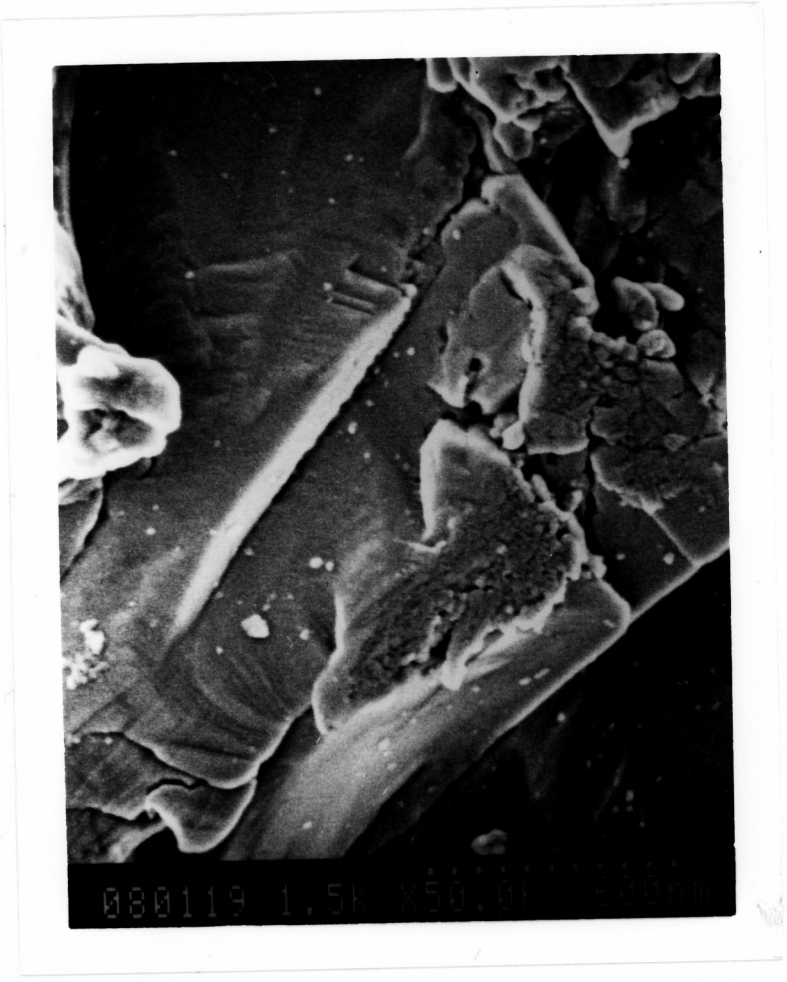

Figure 34. Scanning electron micrograph of a hydroxyapatite disk sintered at 1200 °C (50,000 X).

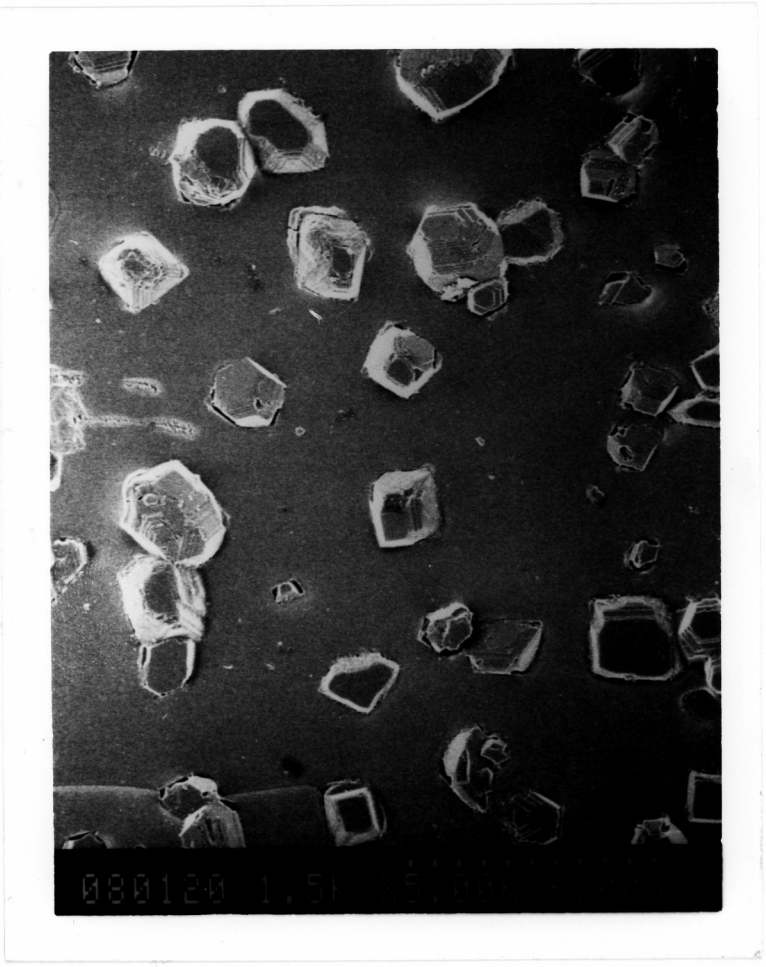

Figure 35. Scanning electron micrograph of a hydroxyapatite disk sintered at 1300 °C (5,000 X).

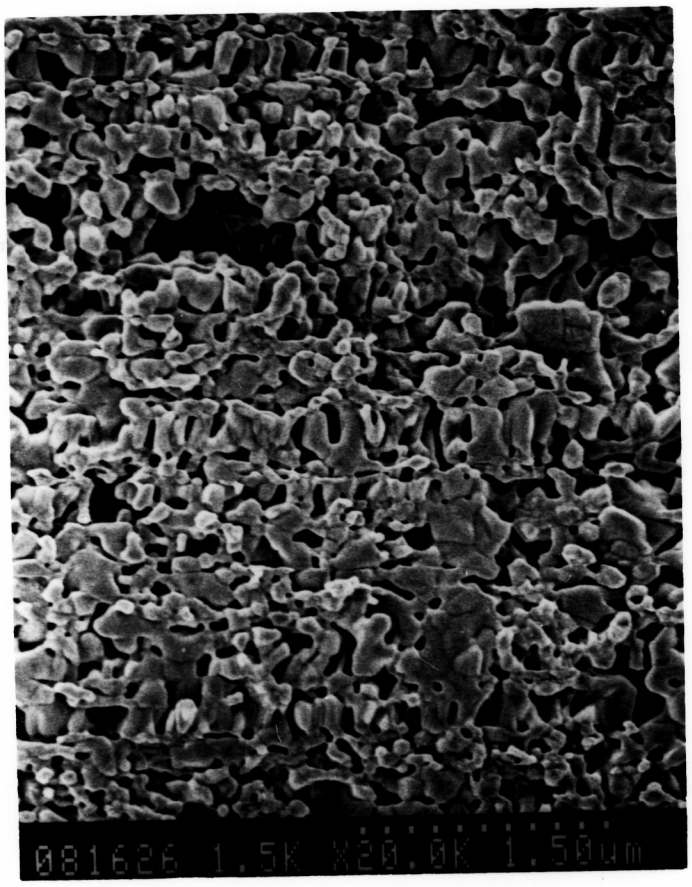

Figure 36. Scanning electron micrograph of a green tricalcium phosphate prefired at 720 °C (20,000 X).

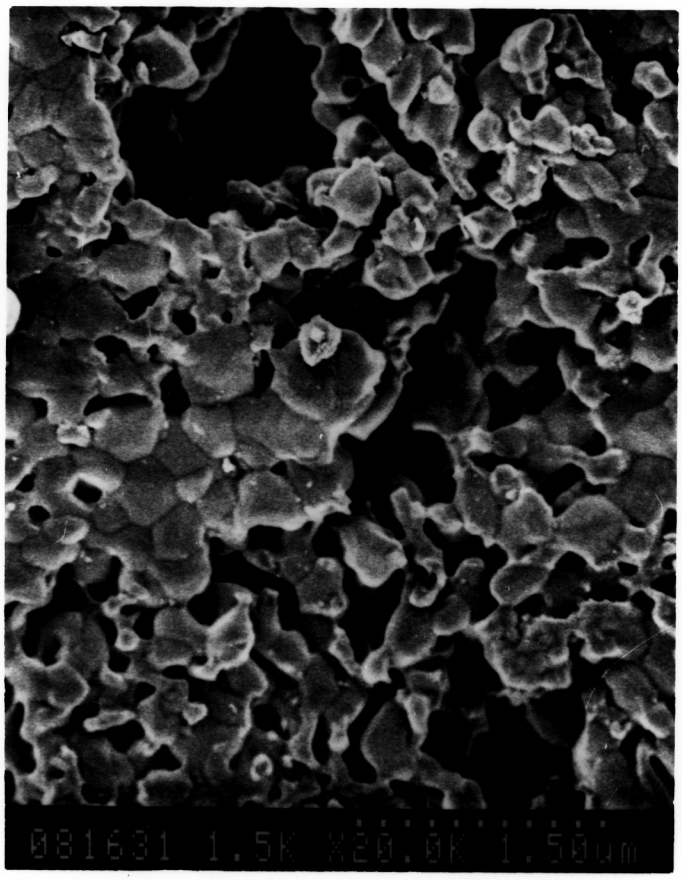

Figure 37. Scanning electron micrograph of a β-whitlockite disk sintered at 900 °C (20,000 X).

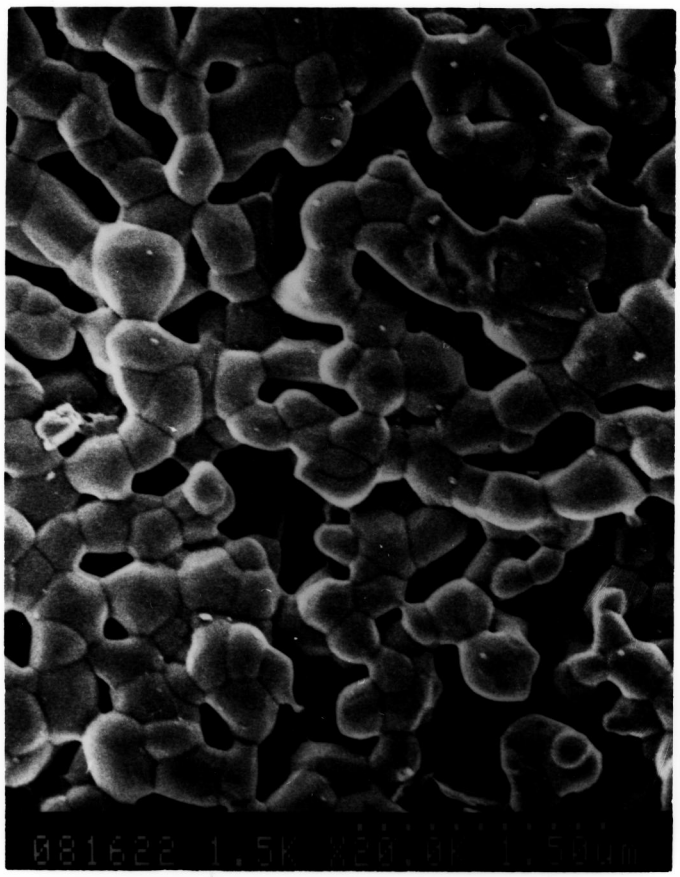

Figure 38. Scanning electron micrograph of a β-whitlockite disk sintered at 1000 °C (20,000 X).

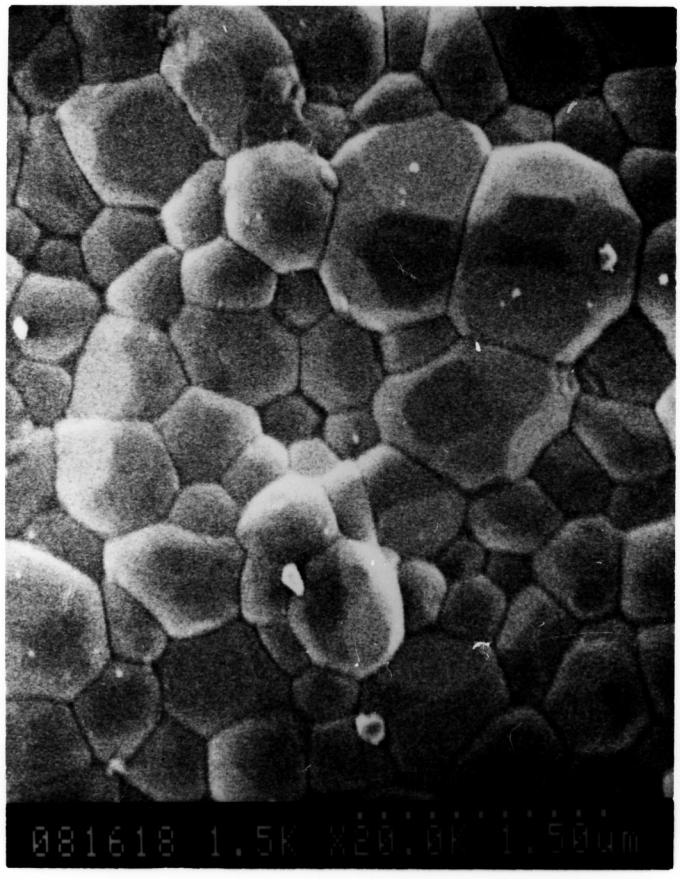

Figure 39. Scanning electron micrograph of a β-whitlockite disk sintered at 1100 °C (20,000 X).

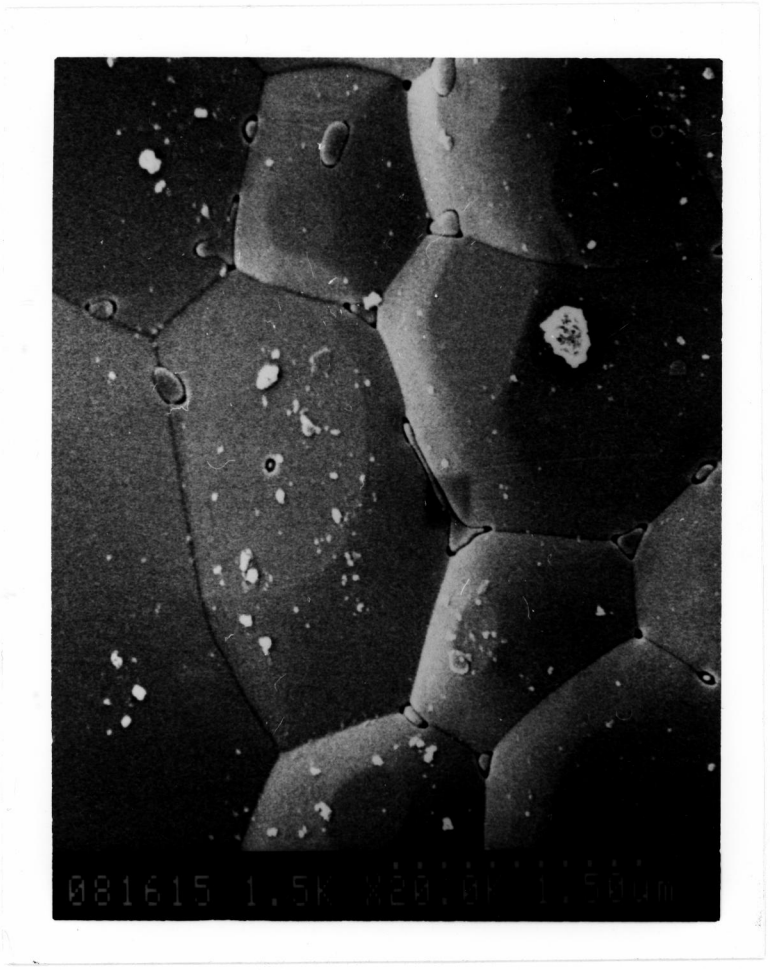

Figure 40. Scanning electron micrograph of a β-whitlockite disk sintered at 1200 °C (20,000 X).

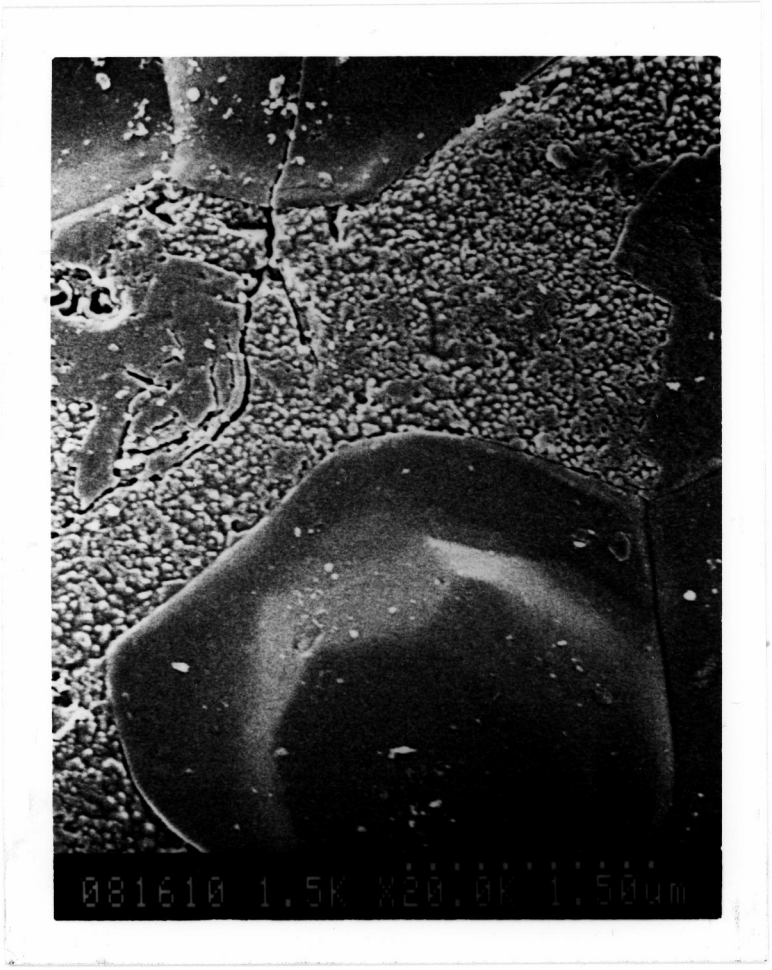

Figure 41. Scanning electron micrograph of a β-whitlockite disk sintered at 1300 °C (20,000 X).

4. Pycnometric densities of sintered disks

The densities of sintered hydroxyapatite disks determined by helium, aqueous, and methanolic pycnometry are given in Tables XV and XVI; the densities of sintered β-whitlockite disks determined by helium and aqueous pycnometry are shown in Table XVII.

5. Volume fraction isolated and volume fraction accessible

Calculation of volume fraction isolated and volume fraction accessible. Volume fraction isolated for each lot of disks was calculated using eq 14; volume fraction accessible was calculated using eq 15. Volume fraction isolated and volume fraction accessible values for hydroxyapatite disks for each of the pycnometry methods are given in Tables XVIII, XIX, and XX. Values for β-whitlockite disks are shown in Tables XXI and XXII. The uncertainties for ϕ^i and ϕ^a were determined by a standard propagation of error technique (*71*).

Determination of the apparent critical percolation threshold. The apparent critical percolation threshold, $\phi_{c,app}$, was determined by fitting the volume fraction accessible data (for disks with $\phi > 0.175$) to the following scaling relationship (*1-4*)

Table XV. Density of hydroxyapatite disks determined by helium and aqueous pycnometry.

Porosity[a]	Pycnometric density	
	Helium[b]	Aqueous[c]
0.47_8 (0.01_0)[d]	3.08_8 (0.01_0)	3.12_6 (0.05_2)
0.45_8 (0.01_1)	3.12_5 (0.01_5)	3.117 (0.009)
0.45_3 (0.01_1)	3.09_3 (0.01_7)	3.09_5 (0.01_3)
0.40_6 (0.01_1)	3.13_9 (0.01_4)	3.09_4 (0.05_2)
0.38_9 (0.01_2)	3.07_0 (0.01_6)	3.10_6 (0.01_8)
0.372 (0.008)	3.10_9 (0.01_2)	3.10_3 (0.01_0)
0.36_6 (0.02_0)	3.13_3 (0.01_7)	3.03_3 (0.01_3)
0.25_8 (0.02_6)	3.029 (0.008)	3.02_7 (0.01_6)
0.25_5 (0.01_5)	2.960 (0.007)	2.90_2 (0.02_8)
0.24_5 (0.01_5)	3.007 (0.008)	2.83_7 (0.02_8)
0.20_3 (0.01_1)	3.011 (0.007)	2.95_3 (0.03_1)
0.19_4 (0.02_3)	2.960 (0.007)	2.87_2 (0.02_8)
0.19_3 (0.01_7)	2.87_4 (0.01_1)	2.89_3 (0.04_3)

[a]The reported porosities are average values for each manufactured lot which consisted of 14 to 16 disks.
[b]Eight density determinations were performed.
[c]Four density determinations were performed.
[d]Standard deviations are shown in parentheses.

Table XV. (*continued*) Density of hydroxyapatite disks determined by helium and aqueous pycnometry.

	Pycnometric density	
Porosity[a]	Helium[b]	Aqueous[c]
0.18_9 (0.01_3)[d]	2.86_2 (0.01_1)	2.817 (0.006)
0.15_4 (0.01_7)	2.950 (0.007)	2.83_2 (0.02_2)
0.15_4 (0.01_1)	2.98_3 (0.01_2)	3.00_2 (0.02_6)
0.15_1 (0.01_6)	2.96_0 (0.01_8)	2.87_0 (0.02_9)
0.14_9 (0.01_3)	2.903 (0.007)	2.91_9 (0.01_4)
0.14_5 (0.01_6)	2.94_4 (0.01_9)	2.87_6 (0.03_3)
0.14_3 (0.01_7)	2.91_5 (0.01_2)	2.86_9 (0.03_1)
0.12_4 (0.01_6)	2.960 (0.007)	2.88_8 (0.01_0)
0.12_3 (0.01_3)	2.985 (0.009)	2.97_6 (0.02_0)
0.11_5 (0.01_4)	2.97_1 (0.04_3)	2.87_3 (0.04_3)
0.11_3 (0.01_2)	3.08_9 (0.02_2)	2.95_0 (0.02_4)
0.10_4 (0.01_8)	3.07_2 (0.01_5)	3.10_7 (0.01_8)

[a]The reported porosities are average values for each manufactured lot which consisted of 14 to 16 disks.
[b]Eight density determinations were performed.
[c]Four density determinations were performed.
[d]Standard deviations are shown in parentheses.

Table XVI. Density of hydroxyapatite disks determined by methanolic pycnometry.

Porosity[a]	Pycnometric density[b]
0.47_8 (0.01_0)[c]	3.05_3 (0.09_5)
0.40_6 (0.01_1)	3.0_7 (0.1_4)
0.372 (0.008)	3.0_7 (0.1_4)
0.36_6 (0.02_0)	2.92_9 (0.03_1)
0.24_5 (0.01_5)	2.8_6 (0.1_0)
0.20_3 (0.01_1)	2.7_1 (0.1_0)
0.18_9 (0.01_3)	3.01_8 (0.01_3)
0.15_4 (0.01_1)	2.92_4 (0.02_9)
0.15_1 (0.01_6)	2.89_5 (0.06_6)
0.14_9 (0.01_3)	2.89_3 (0.02_8)
0.14_5 (0.01_6)	2.7_6 (0.1_1)
0.14_3 (0.01_7)	2.70_6 (0.05_7)
0.11_5 (0.01_4)	2.93_9 (0.03_3)
0.10_4 (0.01_8)	3.00_3 (0.04_9)

[a]The reported porosities are average values for each manufactured lot which consisted of 14 to 16 disks.
[b]Four density determinations were performed.
[c]Standard deviations are shown in parentheses.

Table XVII. Density of β-whitlockite disks determined by helium and aqueous pycnometry.

	Pycnometric density	
Porosity[a]	Helium[b]	Aqueous[c]
0.50_3 (0.01_2)[d]	3.042 (0.005)	2.91_8 (0.01_7)
0.496 (0.008)	3.03_0 (0.01_2)	2.95_4 (0.02_4)
0.47_6 (0.01_1)	3.06_0 (0.009)	2.94_4 (0.02_4)
0.43_5 (0.01_7)	3.04_0 (0.01_0)	2.92_6 (0.03_2)
0.41_5 (0.01_5)	3.06_9 (0.04_0)	2.95_2 (0.02_8)
0.37_8 (0.01_3)	3.06_4 (0.01_2)	2.99_6 (0.03_4)
0.37_3 (0.01_1)	3.065 (0.007)	2.922 (0.005)
0.32_3 (0.02_0)	2.95_1 (0.01_7)	2.95_1 (0.01_1)
0.31_7 (0.01_6)	3.067 (0.007)	2.88_9 (0.02_3)
0.25_4 (0.01_5)	3.067 (0.008)	2.88_0 (0.03_4)
0.24_2 (0.01_1)	3.029 (0.006)	2.92_4 (0.03_6)
0.21_6 (0.02_4)	3.03_8 (0.01_4)	2.86_3 (0.02_6)

[a]The reported porosities are average values for each manufactured lot which consisted of 14 to 16 disks.
[b]Eight density determinations were performed.
[c]Four density determinations were performed.
[d]Standard deviations are shown in parentheses.

Table XVII. (*continued*) Density of β-whitlockite disks determined by helium and aqueous pycnometry.

	Pycnometric density	
Porosity[a]	Helium[b]	Aqueous[c]
0.17_7 (0.01_7)[d]	3.04_6 (0.01_7)	2.79_3 (0.03_0)
0.16_4 (0.01_4)	2.911 (0.004)	2.86_2 (0.01_1)
0.14_0 (0.01_2)	2.95_1 (0.01_6)	2.87_5 (0.01_7)
0.13_5 (0.01_3)	2.97_4 (0.01_2)	2.79_8 (0.02_1)
0.12_5 (0.01_4)	3.11_6 (0.03_3)	2.88_2 (0.02_2)

[a]The reported porosities are average values for each manufactured lot which consisted of 14 to 16 disks.
[b]Eight density determinations were performed.
[c]Four density determinations were performed.
[d]Standard deviations are shown in parentheses.

Table XVIII. Volume fraction isolated and volume fraction accessible of hydroxyapatite disks determined by helium pycnometry.

Porosity[a]	ϕ^i	ϕ^a
0.47_8 (0.01_0)[b]	0.012 (0.001)[c]	0.466 (0.008)[c]
0.45_8 (0.01_1)	0.006 (0.002)	0.452 (0.009)
0.45_3 (0.01_1)	0.012 (0.003)	0.44_1 (0.01_0)
0.40_6 (0.01_1)	0.004 (0.002)	0.402 (0.009)
0.38_9 (0.01_2)	0.018 (0.003)	0.37_1 (0.01_0)
0.372 (0.008)	0.010 (0.002)	0.362 (0.007)
0.36_6 (0.02_0)	0.005 (0.003)	0.36_1 (0.01_7)
0.25_8 (0.02_6)	0.032 (0.002)	0.22_6 (0.02_2)
0.25_5 (0.01_5)	0.050 (0.002)	0.20_5 (0.01_3)
0.24_5 (0.01_5)	0.038 (0.002)	0.20_7 (0.01_3)
0.20_3 (0.01_1)	0.039 (0.002)	0.164 (0.009)
0.19_4 (0.02_3)	0.054 (0.002)	0.14_0 (0.01_9)
0.19_3 (0.01_7)	0.080 (0.003)	0.11_3 (0.01_5)

[a] The reported porosities are average values for each manufactured lot which consisted of 14 to 16 disks.
[b] Standard deviations are shown in parentheses.
[c] Confidence limits (P = 0.05; N = 8) are shown in parentheses.

Table XVIII. (*continued*) Volume fraction isolated and volume fraction accessible of hydroxyapatite disks determined by helium pycnometry.

Porosity[a]	ϕ^i	ϕ^a
0.18_9 (0.01_3)[b]	0.084 (0.003)[c]	0.10_5 (0.01_1)[c]
0.15_4 (0.01_7)	0.060 (0.002)	0.09_4 (0.01_4)
0.15_4 (0.01_1)	0.050 (0.003)	0.10_4 (0.01_0)
0.15_1 (0.01_6)	0.057 (0.005)	0.09_4 (0.01_4)
0.14_9 (0.01_3)	0.075 (0.002)	0.07_4 (0.01_1)
0.14_5 (0.01_6)	0.063 (0.005)	0.08_2 (0.01_4)
0.14_3 (0.01_7)	0.072 (0.003)	0.07_1 (0.01_5)
0.12_4 (0.01_6)	0.059 (0.002)	0.06_5 (0.01_4)
0.12_3 (0.01_3)	0.051 (0.002)	0.07_2 (0.01_1)
0.11_5 (0.01_4)	0.05_6 (0.01_1)	0.05_9 (0.01_6)
0.11_3 (0.01_2)	0.020 (0.005)	0.09_3 (0.01_1)
0.10_4 (0.01_8)	0.026 (0.004)	0.07_8 (0.01_6)

[a] The reported porosities are average values for each manufactured lot which consisted of 14 to 16 disks.
[b] Standard deviations are shown in parentheses.
[c] Confidence limits (P = 0.05; N = 8) are shown in parentheses.

Table XIX. Volume fraction isolated and volume fraction accessible of hydroxyapatite disks determined by aqueous pycnometry.

Porosity[a]	ϕ^i	ϕ^a
0.47_8 (0.01_0)[b]	0.00_6 (0.01_4)[c]	0.47_2 (0.02_1)[c]
0.45_8 (0.01_1)	0.007 (0.003)	0.45_1 (0.01_8)
0.45_3 (0.01_1)	0.011 (0.004)	0.44_2 (0.01_8)
0.40_6 (0.01_1)	0.01_3 (0.01_6)	0.39_3 (0.02_4)
0.38_9 (0.01_2)	0.011 (0.006)	0.37_8 (0.02_0)
0.372 (0.008)	0.012 (0.003)	0.36_0 (0.01_3)
0.36_6 (0.02_0)	0.027 (0.005)	0.33_9 (0.03_2)
0.25_8 (0.02_6)	0.033 (0.007)	0.22_5 (0.04_2)
0.25_5 (0.01_5)	0.06_6 (0.01_3)	0.18_9 (0.02_7)
0.24_5 (0.01_5)	0.08_6 (0.01_3)	0.15_9 (0.02_7)
0.20_3 (0.01_1)	0.05_6 (0.01_4)	0.14_7 (0.02_3)
0.19_4 (0.02_3)	0.08_1 (0.01_4)	0.11_3 (0.03_9)
0.19_3 (0.01_7)	0.07_4 (0.02_1)	0.11_9 (0.03_4)

[a] The reported porosities are average values for each manufactured lot which consisted of 14 to 16 disks.
[b] Standard deviations are shown in parentheses.
[c] Confidence limits (P = 0.05; N = 4) are shown in parentheses.

Table XIX. (*continued*) Volume fraction isolated and volume fraction accessible of hydroxyapatite disks determined by aqueous pycnometry.

Porosity[a]	ϕ^i	ϕ^a
0.18_9 (0.01_3)[b]	0.099 (0.004)[c]	0.09_0 (0.02_1)[c]
0.15_4 (0.01_7)	0.09_8 (0.01_2)	0.05_6 (0.03_0)
0.15_4 (0.01_1)	0.04_5 (0.01_2)	0.10_9 (0.02_1)
0.15_1 (0.01_6)	0.08_6 (0.01_5)	0.06_5 (0.03_0)
0.14_9 (0.01_3)	0.070 (0.007)	0.07_9 (0.02_2)
0.14_5 (0.01_6)	0.08_4 (0.01_7)	0.06_1 (0.03_1)
0.14_3 (0.01_7)	0.08_7 (0.01_6)	0.05_6 (0.03_2)
0.12_4 (0.01_6)	0.083 (0.006)	0.04_1 (0.02_6)
0.12_3 (0.01_3)	0.05_4 (0.01_0)	0.06_9 (0.02_3)
0.11_5 (0.01_4)	0.08_8 (0.02_3)	0.02_7 (0.03_2)
0.11_3 (0.01_2)	0.06_3 (0.01_2)	0.05_0 (0.02_3)
0.10_4 (0.01_8)	0.015 (0.008)	0.08_9 (0.03_0)

[a] The reported porosities are average values for each manufactured lot which consisted of 14 to 16 disks.
[b] Standard deviations are shown in parentheses.
[c] Confidence limits (P = 0.05; N = 4) are shown in parentheses.

Table XX. Volume fraction isolated and volume fraction accessible of hydroxyapatite disks determined by methanolic pycnometry.

Porosity[a]	ϕ^i	ϕ^a
0.47_8 (0.01_0)[b]	0.01_8 (0.02_7)[c]	0.46_0 (0.03_1)[c]
0.40_6 (0.01_1)	0.01_7 (0.04_4)	0.38_9 (0.04_8)
0.372 (0.008)	0.01_8 (0.04_7)	0.35_4 (0.04_9)
0.36_6 (0.02_0)	0.05_0 (0.01_2)	0.31_6 (0.03_4)
0.24_5 (0.01_5)	0.07_9 (0.04_6)	0.16_6 (0.05_2)
0.20_3 (0.01_1)	0.13_2 (0.05_5)	0.07_1 (0.05_7)
0.18_9 (0.01_3)	0.038 (0.006)	0.15_1 (0.02_2)
0.15_4 (0.01_1)	0.06_8 (0.01_4)	0.08_6 (0.02_3)
0.15_1 (0.01_6)	0.07_8 (0.03_4)	0.07_3 (0.04_2)
0.14_9 (0.01_3)	0.07_9 (0.01_4)	0.07_0 (0.02_5)
0.14_5 (0.01_6)	0.12_4 (0.06_2)	0.02_1 (0.06_7)
0.14_3 (0.01_7)	0.14_3 (0.03_4)	0.00_0 (0.04_3)
0.11_5 (0.01_4)	0.06_7 (0.01_7)	0.04_8 (0.02_8)
0.10_4 (0.01_8)	0.04_7 (0.02_5)	0.05_7 (0.03_8)

[a] The reported porosities are average values for each manufactured lot which consisted of 14 to 16 disks.
[b] Standard deviations are shown in parentheses.
[c] Confidence limits (P = 0.05; N = 4) are shown in parentheses.

Table XXI. Volume fraction isolated and volume fraction accessible of β-whitlockite disks determined by helium pycnometry.

Porosity[a]	ϕ^i	ϕ^a
0.50_3 (0.01_2)[b]	0.019 (0.001)[c]	0.48_4 (0.01_0)[c]
0.496 (0.008)	0.022 (0.002)	0.474 (0.007)
0.47_6 (0.01_1)	0.017 (0.001)	0.459 (0.009)
0.43_5 (0.01_7)	0.022 (0.002)	0.41_3 (0.01_4)
0.41_5 (0.01_5)	0.017 (0.007)	0.39_8 (0.01_4)
0.37_8 (0.01_3)	0.019 (0.002)	0.35_9 (0.01_1)
0.37_3 (0.01_1)	0.019 (0.001)	0.354 (0.009)
0.32_3 (0.02_0)	0.048 (0.004)	0.27_5 (0.01_7)
0.31_7 (0.01_6)	0.021 (0.001)	0.29_6 (0.01_3)
0.25_4 (0.01_5)	0.023 (0.002)	0.23_1 (0.01_3)
0.24_2 (0.01_1)	0.033 (0.001)	0.209 (0.009)
0.21_6 (0.02_4)	0.031 (0.003)	0.18_5 (0.02_0)

[a] The reported porosities are average values for each manufactured lot which consisted of 14 to 16 disks.
[b] Standard deviations are shown in parentheses.
[c] Confidence limits (P = 0.05; N = 8) are shown in parentheses.

Table XXI. (*continued*) Volume fraction isolated and volume fraction accessible of β-whitlockite disks determined by helium pycnometry.

Porosity[a]	ϕ^i	ϕ^a
0.17_7 (0.01_7)[b]	0.031 (0.004)[c]	0.14_6 (0.01_5)[c]
0.16_4 (0.01_4)	0.072 (0.001)	0.09_2 (0.01_2)
0.14_0 (0.01_2)	0.061 (0.004)	0.07_2 (0.01_1)
0.13_5 (0.01_3)	0.054 (0.003)	0.08_1 (0.01_1)
0.12_5 (0.01_4)	0.012 (0.008)	0.11_3 (0.01_4)

[a] The reported porosities are average values for each manufactured lot which consisted of 14 to 16 disks.
[b] Standard deviations are shown in parentheses.
[c] Confidence limits (P = 0.05; N = 8) are shown in parentheses.

Table XXII. Volume fraction isolated and volume fraction accessible of β-whitlockite disks determined by aqueous pycnometry.

Porosity[a]	ϕ^i	ϕ^a
0.50_3 (0.01_2)[b]	0.041 (0.005)[c]	0.46_2 (0.02_0)[c]
0.496 (0.008)	0.035 (0.007)	0.46_1 (0.01_5)
0.47_6 (0.01_1)	0.038 (0.007)	0.43_8 (0.01_9)
0.43_5 (0.01_7)	0.04_5 (0.01_1)	0.39_0 (0.02_9)
0.41_5 (0.01_5)	0.04_1 (0.01_0)	0.37_4 (0.02_6)
0.37_8 (0.01_3)	0.03_4 (0.01_2)	0.34_4 (0.02_4)
0.37_3 (0.01_1)	0.051 (0.002)	0.32_2 (0.01_8)
0.32_3 (0.02_0)	0.048 (0.005)	0.27_5 (0.03_2)
0.31_7 (0.01_6)	0.06_4 (0.01_0)	0.25_3 (0.02_7)
0.25_4 (0.01_5)	0.07_3 (0.01_6)	0.18_1 (0.02_8)
0.24_2 (0.01_1)	0.06_1 (0.01_6)	0.18_1 (0.02_4)
0.21_6 (0.02_4)	0.08_1 (0.01_3)	0.13_5 (0.04_0)

[a] The reported porosities are average values for each manufactured lot which consisted of 14 to 16 disks.
[b] Standard deviations are shown in parentheses.
[c] Confidence limits (P = 0.05; N = 4) are shown in parentheses.

Table XXII. (*continued*) Volume fraction isolated and volume fraction accessible of β-whitlockite disks determined by aqueous pycnometry.

Porosity[a]	ϕ^i	ϕ^a
0.17_7 (0.01_7)[b]	0.10_8 (0.01_0)[c]	0.06_9 (0.03_2)[c]
0.16_4 (0.01_4)	0.087 (0.004)	0.07_7 (0.02_3)
0.14_0 (0.01_2)	0.085 (0.006)	0.05_5 (0.02_1)
0.13_5 (0.01_3)	0.112 (0.008)	0.02_3 (0.02_4)
0.12_5 (0.01_4)	0.084 (0.007)	0.04_1 (0.02_5)

[a] The reported porosities are average values for each manufactured lot which consisted of 14 to 16 disks.
[b] Standard deviations are shown in parentheses.
[c] Confidence limits (P = 0.05; N = 4) are shown in parentheses.

$$\phi^a = m_{app} \ (\phi - \phi_{c,app})^{0.4} \qquad (18)$$

using multivariate nonlinear regression analysis (*72*).

Determination of surface porosity (ϕ^s). Since disks with porosities below the critical percolation threshold showed a nonzero volume fraction accessible value, contradictory to percolation theory, it was hypothesized that the apparent volume fraction accessible value was due to the roughness of the surface. The amount of surface porosity was estimated by averaging the volume fraction accessible values for disks with porosities below $\phi_{c,app}$. The estimated surface porosities are shown in Table XXIII.

Determination of the critical percolation threshold. In order to account for the observed surface porosity effects, the volume fraction accessible data (for disks with porosities between $\phi_{c,app}$ and 0.35) were fit to the following modified scaling relationship

$$\phi^a = m \ (\phi - \phi_c)^{0.4} + \phi^s \qquad (19)$$

using multivariate nonlinear regression analysis (*72*). In addition to ϕ_c, the variable m, a preexponential factor, in

Table XXIII. Surface porosity[a] of hydroxyapatite and β-whitlockite disks.

Ceramic	Pycnometry method	ϕ^s
hydroxyapatite	helium	0.08_1 (0.01_4)[b]
hydroxyapatite	aqueous	0.06_4 (0.02_3)
hydroxyapatite	methanolic	0.05_1 (0.03_1)
β-whitlockite	helium	0.09_0 (0.01_8)
β-whitlockite	aqueous	0.04_9 (0.02_3)

[a]The reported surface porosities were calculated by averaging the volume fraction accessible values for disks with porosities below the critical percolation threshold.

[b]Standard deviations are shown in parentheses.

eq 19 was also determined. The values of m and ϕ_c determined by the regression are given in Table XXIV. The volume fraction isolated can be calculated by subtacting the calculated ϕ^a from the porosity (*1-4*)

$$\phi^i = \phi - \phi^a \qquad (20)$$

Plots of the volume fraction accessible data for hydroxyapatite and β-whitlockite for the helium and aqueous pycnometry methods are shown in Figures 42 to 45; plots of the volume fraction isolated data for hydroxyapatite and β-whitlockite for both pycnometry methods are shown in Figures 46 to 49. The methanolic pycnometry data were not plotted and were not fit to eq 19 due to the large uncertainties in these data.

Table XXIV. Results of the regression analyses of volume fraction accessible data for hydroxyapatite (H) and β-whitlockite (W) disks.

Ceramic	Pycnometry method	ϕ_c	m	N
H	helium	0.189 (0.002)[a]	0.3_7 (0.1_5)	7
H	aqueous	0.18_7 (0.00_6)	0.39 (0.08)	7
W	helium	0.17_1 (0.01_3)	0.39 (0.06)	6
W	aqueous	0.17_7 (0.00_3)	0.42 (0.07)	6

[a]Confidence limits (P = 0.05) are shown in parentheses.

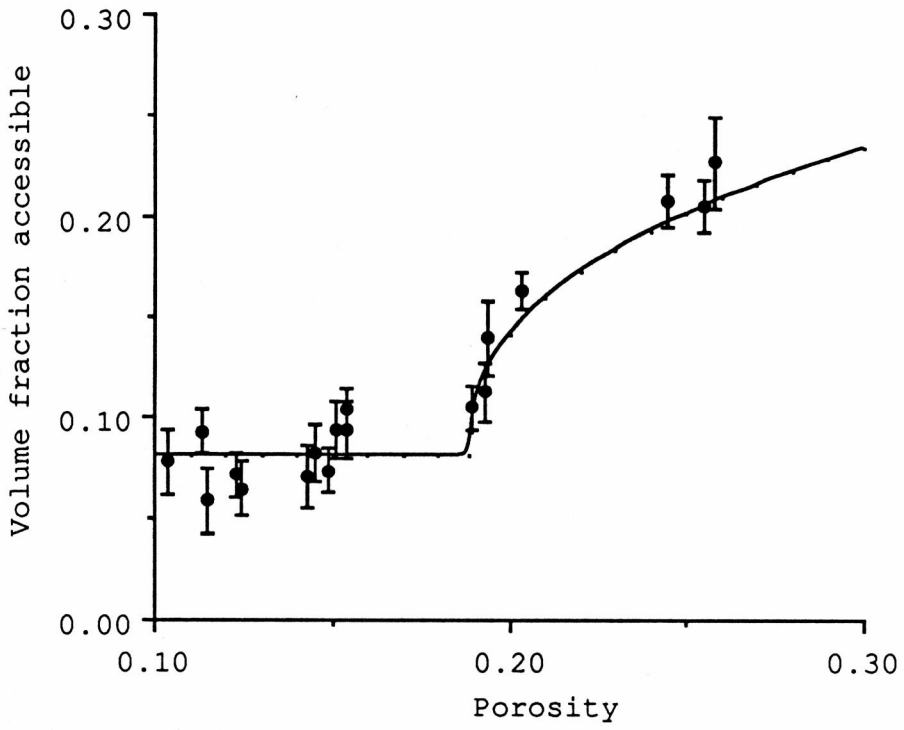

Figure 42. Volume fraction accessible (determined from helium pycnometry) as a function of porosity for hydroxyapatite disks. The line represents the nonlinear regression fit of the data to the scaling relationship given by eq 19 ($\phi_c = 0.189$; $m = 0.3_7$).

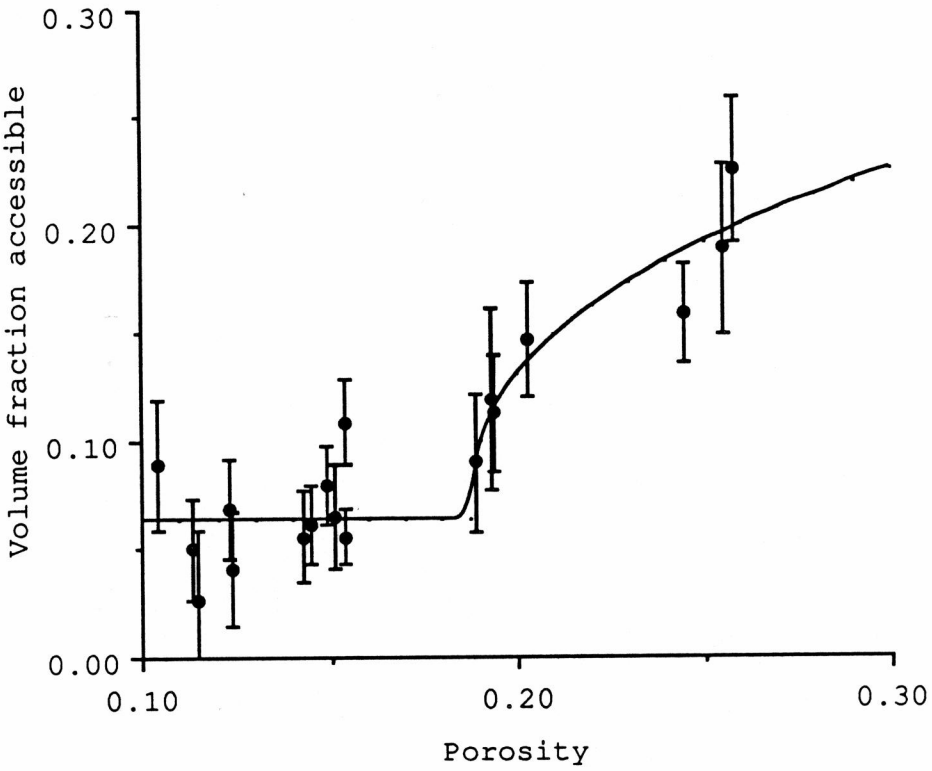

Figure 43. Volume fraction accessible (determined from aqueous pycnometry) as a function of porosity for hydroxyapatite disks. The line represents the nonlinear regression fit of the data to the scaling relationship given by eq 19 ($\phi_c = 0.18_7$; m = 0.39).

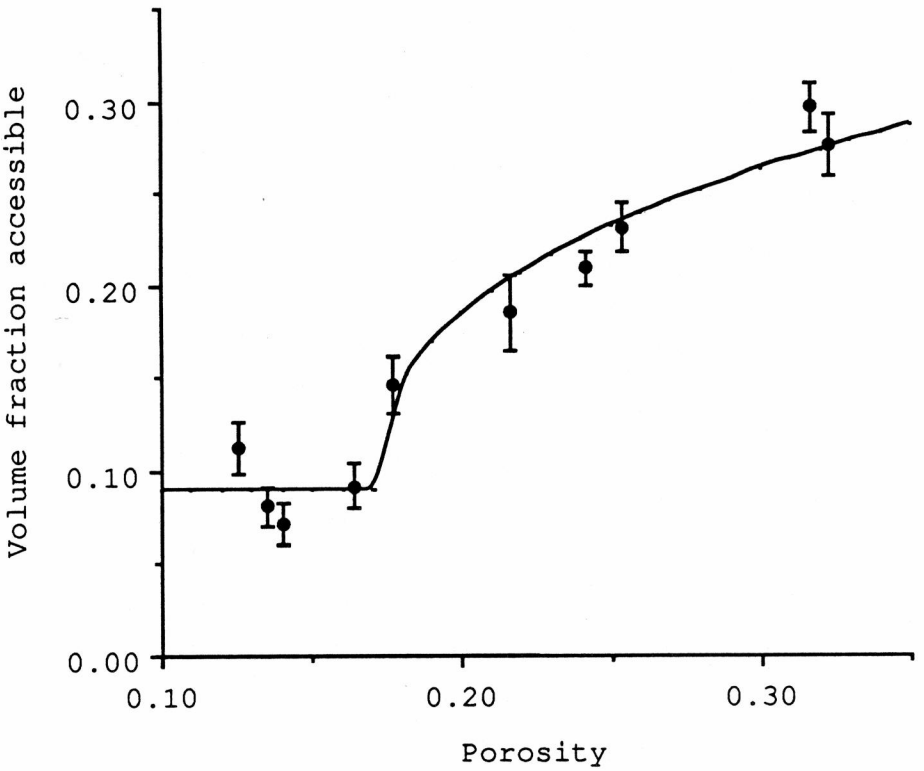

Figure 44. Volume fraction accessible (determined from helium pycnometry) as a function of porosity for β-whitlockite disks. The line represents the nonlinear regression fit of the data to the scaling relationship given by eq 19 ($\phi_c = 0.17_1$; m = 0.39).

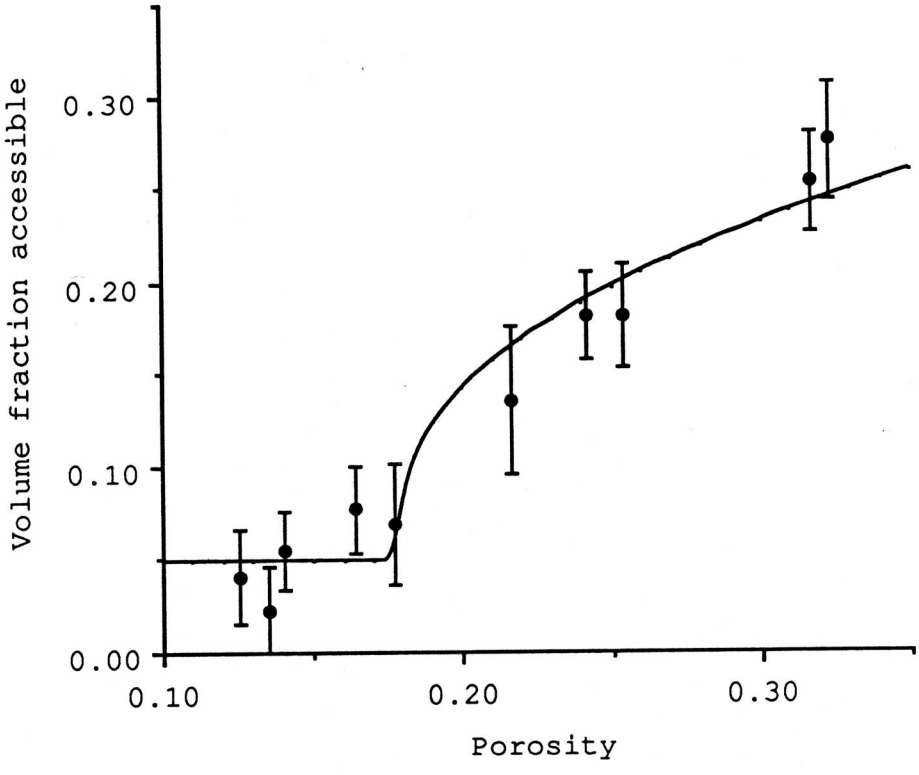

Figure 45. Volume fraction accessible (determined from aqueous pycnometry) as a function of porosity for β-whitlockite disks. The line represents the nonlinear regression fit of the data to the scaling relationship given by eq 19 ($\phi_c = 0.17_7$; $m = 0.42$).

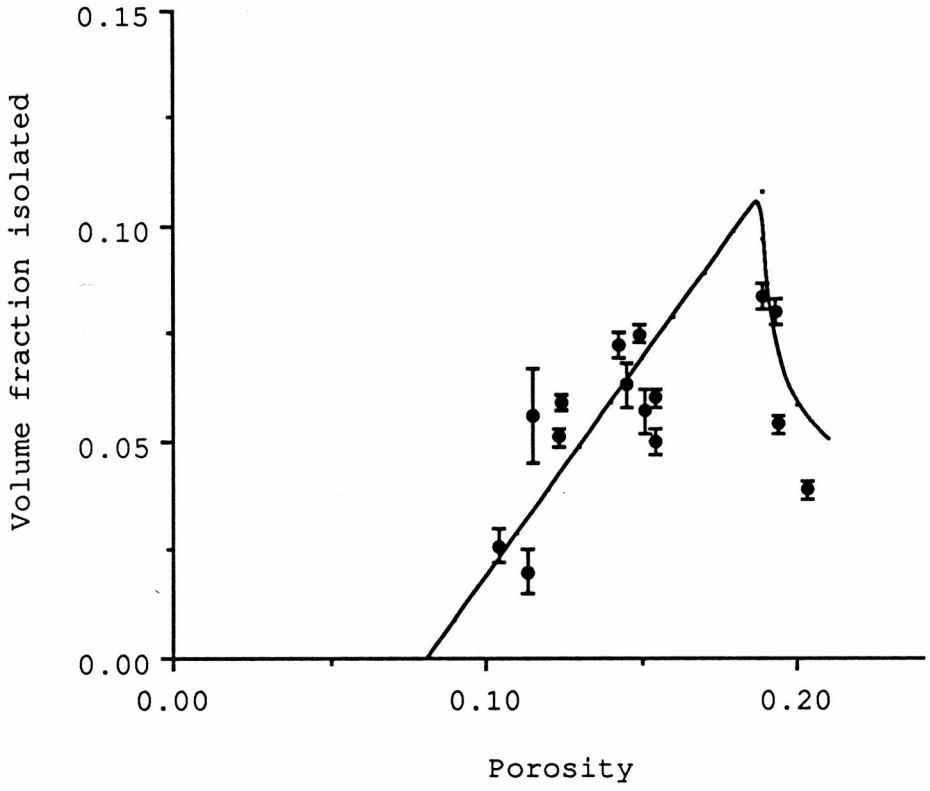

Figure 46. Volume fraction isolated (determined from helium pycnometry) as a function of porosity for hydroxyapatite disks. For $\phi \geq \phi_c$, the line represents the ϕ^i calculated using eq 20; for $\phi < \phi_c$, the straight line is drawn between the following points: $(\phi^s, 0)$ and (ϕ_c, ϕ^i_{max}).

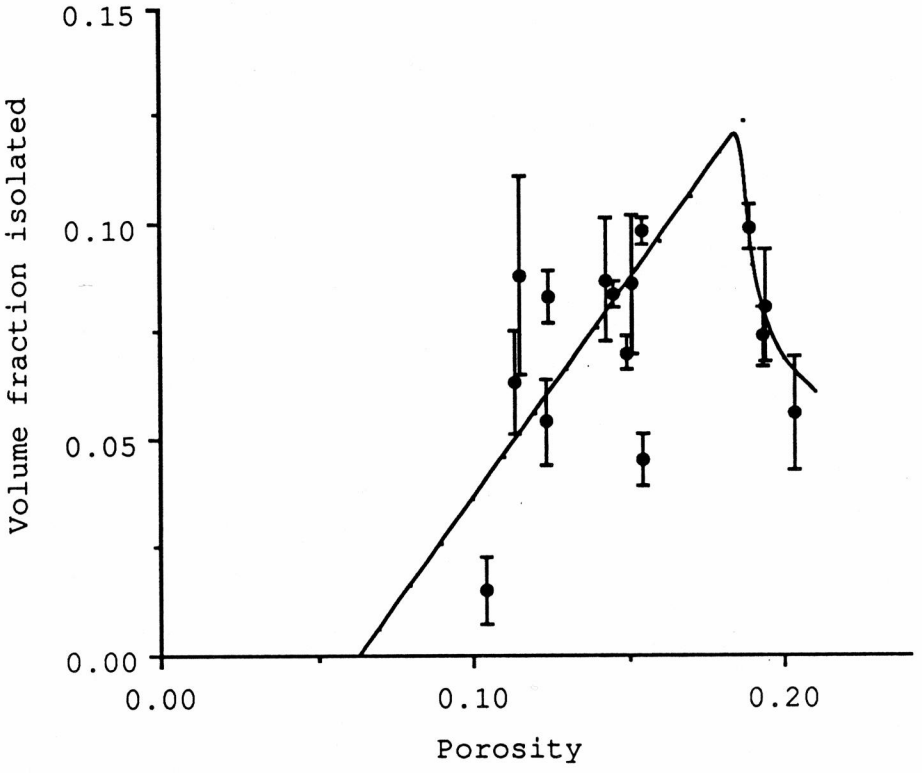

Figure 47. Volume fraction isolated (determined from aqueous pycnometry) as a function of porosity for hydroxyapatite disks. For $\phi \geq \phi_c$, the line represents the ϕ^i calculated using eq 20; for $\phi < \phi_c$, the straight line is drawn between the following points: $(\phi^s, 0)$ and (ϕ_c, ϕ^i_{max}).

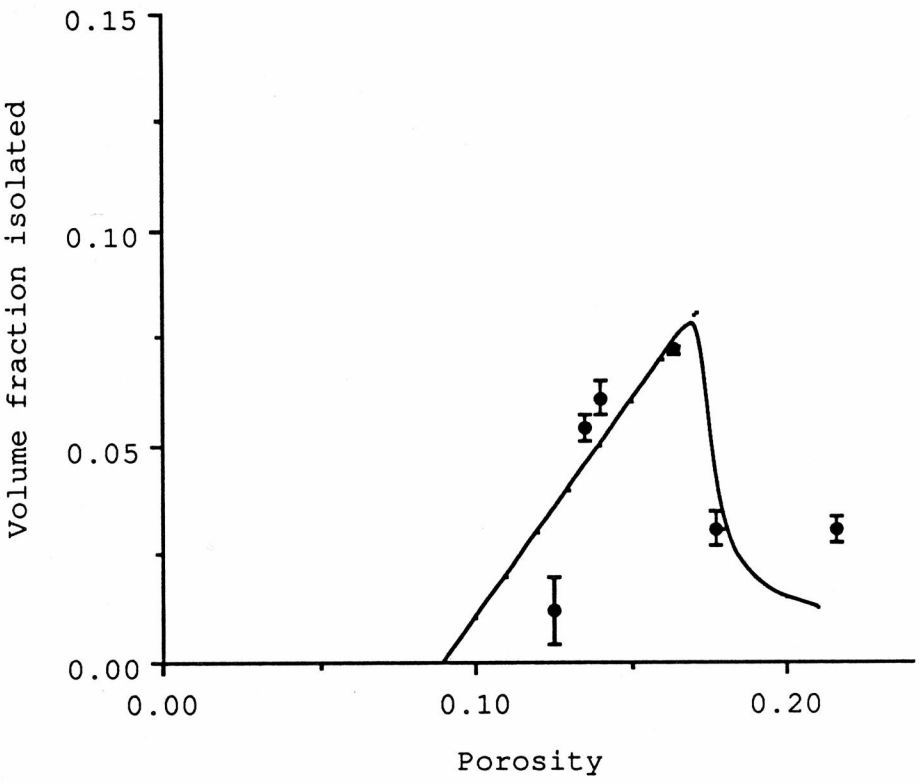

Figure 48. Volume fraction isolated (determined from helium pycnometry) as a function of porosity for β-whitlockite disks. For $\phi \geq \phi_c$, the line represents the ϕ^i calculated using eq 20; for $\phi < \phi_c$, the straight line is drawn between the following points: $(\phi^s, 0)$ and (ϕ_c, ϕ^i_{max}).

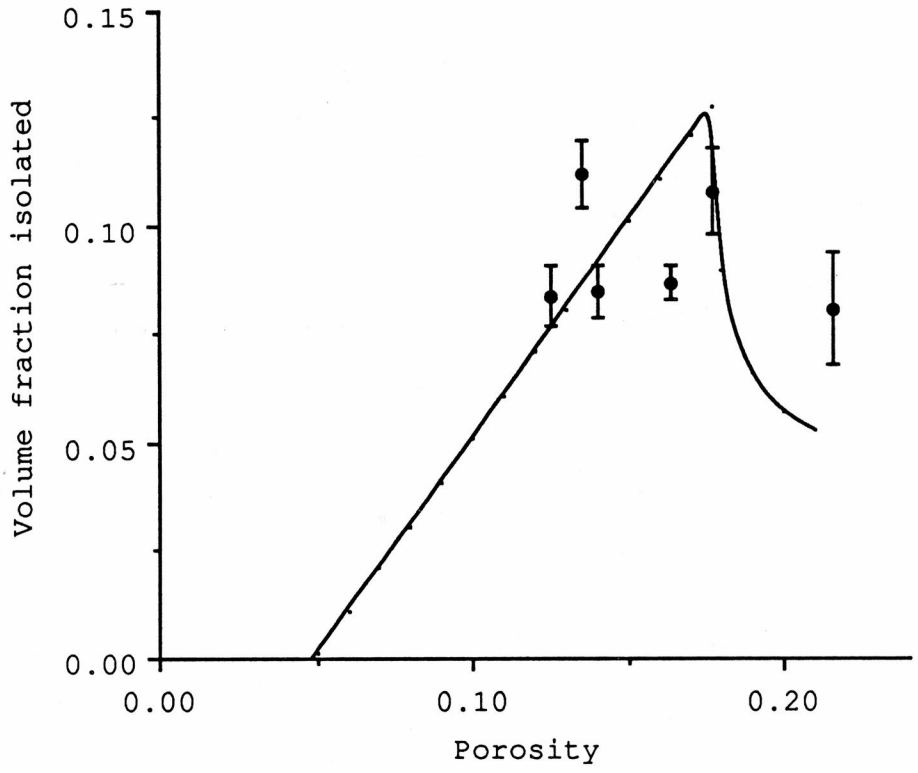

Figure 49. Volume fraction isolated (determined from aqueous pycnometry) as a function of porosity for β-whitlockite disks. For $\phi \geq \phi_c$, the line represents the ϕ^i calculated using eq 20; for $\phi < \phi_c$, the straight line is drawn between the following points: $(\phi^s, 0)$ and (ϕ_c, ϕ^i_{max}).

6. Determination of bulk diffusion coefficients

Two experiments to determine the bulk diffusion coefficients of benzoate ion across hydroxyapatite membranes of various porosities were performed. In these experiments, the concentration of benzoate ion in the upper half-cell of the Stokes diaphragm cell was followed by HPLC analysis. In experiment 1, the upper half-cell was the donor half-cell; the lower half-cell was the donor half-cell in experiment 2. The results of the two experiments are listed in Tables XXV and XXVI. Using mass balance, the concentration of benzoate in the lower half-cell can be calculated. By plotting the left-hand side of eq 16 against time, as shown in Figure 50, a straight line whose slope is $D_B\beta$ is obtained. Since β can be determined independently using the information in Table XXVII and eq 17, D_B can be calculated. The calculated bulk diffusion coefficients are listed in Table XXVIII and are plotted in Figure 51.

The bulk diffusion coefficients can be modeled as a function of membrane porosity using the following modified scaling relationship:

$$D_B = n'(\phi - \phi_c)^{2.0} \qquad (21)$$

Table XXV. Diffusion experiment 1. Concentration (C_d) of benzoate ion in the donor half-cell.

Time / hr	C_d / mg ml^{-1}						
	ϕ						
	0.460	0.406	0.399	0.383	0.238	0.202	0.104
0	0.249	0.249	0.249	0.249	0.249	0.249	0.249
48	0.233	0.237	0.245	0.243	0.248	0.251	0.255
97	0.216	0.227	0.236	0.237	-----	-----	-----
170	0.197	0.213	0.227	0.230	0.246	0.251	0.253
246	0.181	0.198	0.218	0.225	-----	-----	-----
312	0.174	0.186	0.209	0.214	-----	-----	0.248
384	0.156	-----	-----	-----	-----	-----	-----
481	0.145	0.166	0.194	0.201	-----	0.248	0.249
578	0.143	0.160	0.186	0.192	-----	-----	-----
765	-----	-----	-----	0.183	-----	-----	-----
771	0.126	-----	0.175	-----	-----	-----	-----
1176	-----	-----	-----	0.161	0.240	0.251	0.253

Table XXVI. Diffusion experiment 2. Concentration (C_r) of benzoate ion in the receiver half-cell.

	C_r / mg ml^{-1}					
	ϕ					
Time / hr	0.354	0.325	0.238[a]	0.202[a]	0.201	0.184
0	0.0000	0.0000	0.0000	0.0000	0.0000	0.0000
168	0.0128	0.0170	0.0038	0.0000	0.0000	0.0000
336	0.0197	0.0195	0.0040	0.0000	0.0000	0.0000
505	------	------	0.0048	0.0000	0.0000	0.0000
676	------	------	------	0.0000	0.0000	0.0000
1182	------	------	------	0.0000	0.0000	0.0000

[a]The same disk was also used in diffusion experiment 1.

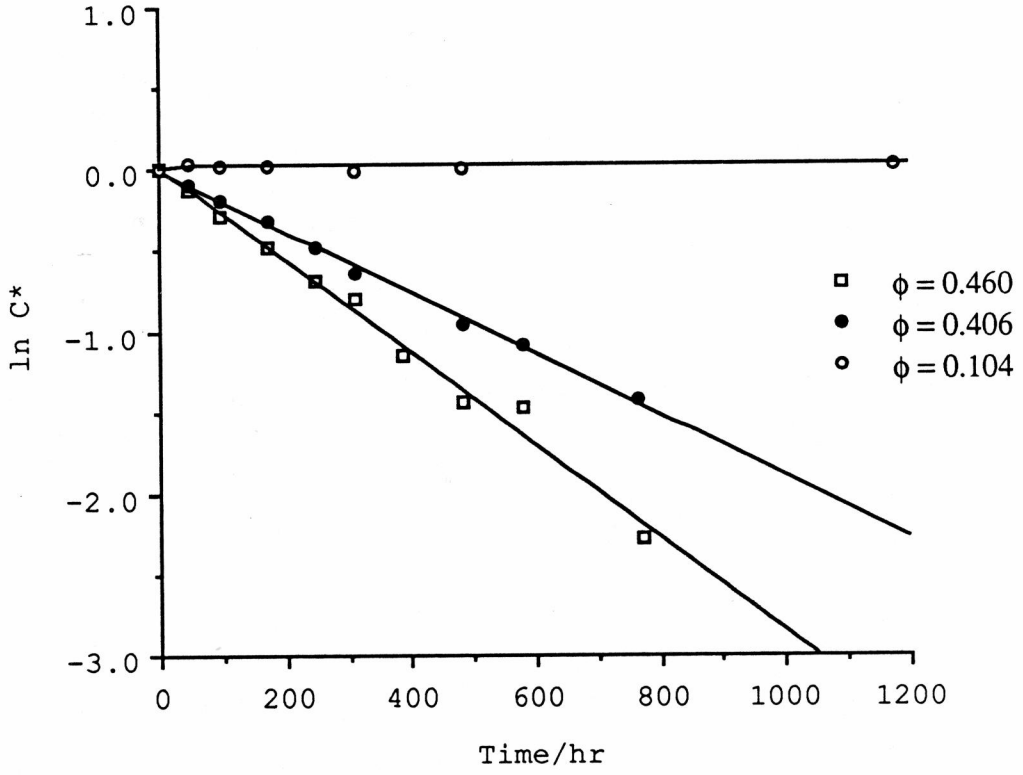

Figure 50. The above plot of ln C^* versus time shows a linear diffusion profile for three disks used in diffusion experiment 1. The value C^* is defined as

$$C^* \equiv \left[\frac{(C_d - C_r)}{C_d^o}\right].$$

Table XXVII. Determination of the diaphragm cell constant β for diffusion experiments 1 and 2.[a]

ϕ	V_r / cm^3	V_d / cm^3	δ / cm	A / cm^2	β / cm^{-2}
0.460[b]	18.4	15.0	0.196	0.636	0.393
0.406[b]	17.6	15.0	0.196	0.636	0.401
0.399[b]	17.9	15.0	0.210	0.636	0.371
0.383[b]	17.8	15.0	0.200	0.636	0.391
0.238[b]	18.1	15.0	0.178	0.636	0.436
0.354[c]	18.2	18.6	0.178	0.636	0.383
0.325[c]	18.8	18.5	0.172	0.636	0.401
0.238[c]	18.5	18.4	0.178	0.636	0.388

[a]The cell constant not calculated for the cells where diffusion of benzoate ion did not occur.

[b]Diffusion experiment 1.

[c]Diffusion experiment 2.

Table XXVIII. Linear regression of diffusion data.

ϕ	N	-10^3 slope[a] / hr		10^9 D_B / cm^2 s^{-1}	
0.460[b]	10	2.8_6	(0.01_1)[c]	$2021._5$	$(7._8)$[c]
0.406[b]	9	1.08_0	(0.002_0)	$748._1$	$(1._4)$
0.399[b]	8	1.88_8	(0.003_6)	$1413._6$	$(2._7)$
0.383[b]	10	0.89_2	(0.01_5)	63_4	(1_1)
0.238[b]	4	0.0057_5	(0.0006_5)	3.6_6	(0.4_1)
0.202[b]	6	0		0	
0.104[b]	6	0		0	
0.354[d]	3	0.050_4	(0.007_6)	$36._6$	$(5._5)$
0.325[d]	3	0.05_1	(0.02_1)	3_5	(1_4)
0.238[d]	4	0.007_5	(0.002_9)	$5._4$	$(2._1)$
0.202[d]	6	0		0	
0.201[d]	6	0		0	
0.184[d]	6	0		0	

[a]Slope = $-D_B\beta$.

[b]Diffusion experiment 1.

[c]Standard error are shown in parentheses.

[d]Diffusion experiment 2.

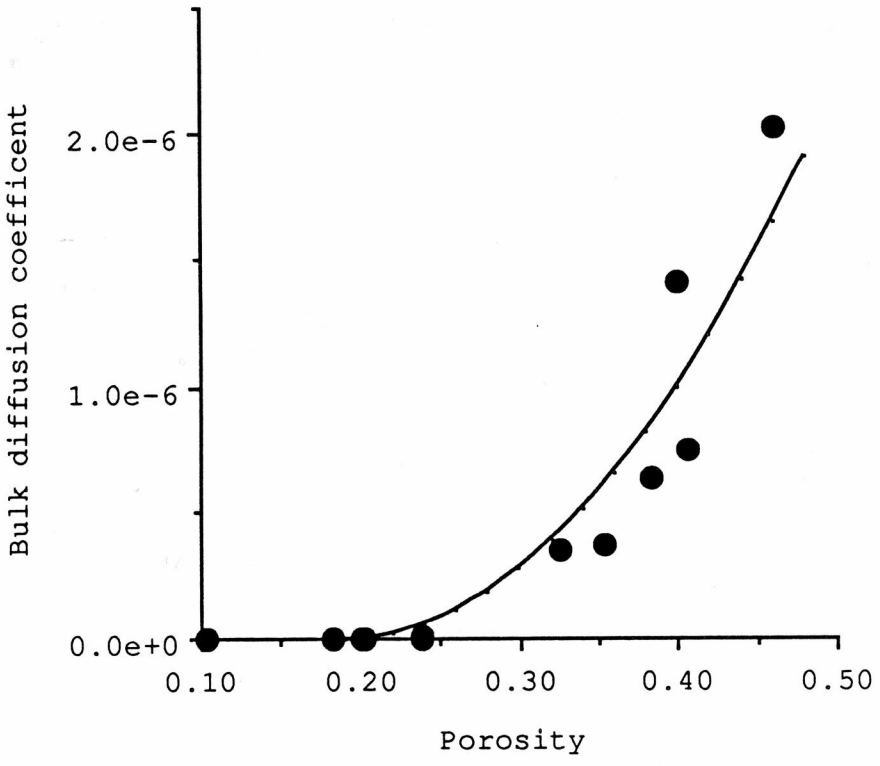

Figure 51. Bulk diffusion coefficients versus porosity. The solid line was obtained by fitting the data to the scaling relationship given in eq 21.

If eq 21 is divided by D_{aq}, one obtains the scaling relationship predicted by percolation theory (*1-4*):

$$\phi^e = \frac{D_B}{D_{aq}} = n\ (\phi - \phi_c)^{2.0} \qquad (22)$$

Since the aqueous diffusion coefficients for benzoate ion have not yet been determined, eq 21 was used to model the data. Assuming the average critical percolation threshold determined by pycnometry (ϕ_c = 0.188), a value of n' = $(2.2_3 \pm 0.5_3)$ X 10^{-5} cm^2 s^{-1} (N = 8; P = 0.05) was determined by nonlinear regression (*72*).

IV. Discussion

A. Manufacturing of porous ceramic disks

The mechanical, electrical conductivity, dielectric, and magnetic properties of a ceramic are governed by the microstructure of the ceramic (*73-74*). Two major contributions to the microstructure that influence these physical properties are the porosity and average grain size. As stated in the introduction, the porosity and pore size distribution of a ceramic prosthetic also influence the physiological properties of the implant.

In our research, we are concerned with the manufacturing of ceramic disks of reproducible residual porosity. Of the five manufacturing variables that were studied, the sintering temperature was the principal variable that controlled the amount of residual porosity of the hydroxyapatite and β-whitlockite disks. From Table XIII, the porosity of the hydroxyapatite disks sintered for 3 hours at 900 °C (ϕ = 0.478) changed only slightly with respect to the green disks (ϕ = 0.495). Similar results were obtained for the β-whitlockite disks. Although the porosity remained virtually unchanged, the microstructure of both ceramics changed considerably. Agglomeration of fine grains and an increase in pore size occurred, as shown

in the photomicrographs obtained by SEM (Figures 30-31 and 36-37).

As shown in Figures 28 and 29, the porosity of both the hydroxyapatite and β-whitlockite disks sintered between 900 and 1100 °C decreased in a nearly linear fashion as the sintering temperature was raised. In addition to densification, substantial grain growth occurred in this temperature region. See Figures 31-33 and 37-39.

As the temperature was raised further to 1200 and 1300 °C, the porosity of both types of ceramic disks did not decrease substantially. Scanning electron microscopy (Figures 34-35 and 40-41) revealed that secondary recrystallization had occurred. The excessive grain growth that occurs during secondary recrystallization is harmful to the mechanical properties of the ceramic (*26*). For ceramics of small grain sizes, strength increases with decreasing grain size.

The porosity of the hydroxyapatite and β-whitlockite disks sintered at a constant temperature changed little as the sintering time was increased from 3 to 12 hours. Although sintering time generally affects the amount of residual porosity (*26*), the rate of sintering of hydroxyapatite and β-whitlockite was so fast that most of the porosity change occurred in the first 15 minutes of

sintering. In contrast, aluminum oxide, another ceramic studied in our laboratory, exhibits a considerable change in porosity when sintered at 1680 °C for periods of 1 to 48 hours (*20*).

Two other manufacturing variables, the amount of granulating agent and the compaction load, were studied only in preliminary experiments. Ten percent (w/w) of PVP granulating agent and a compaction load of 49 kN were used throughout a majority of this work.

The other manufacturing variable examined was the amount of burnout material added to the granulated hydroxyapatite powder prior to compaction. It was hoped that the added burnout material would create a macroporous microstructure. Although the porosity increased as the amount of burnout material increased (Figure 27), SEM analysis showed that the microstructure of the apparent macroporous disks was identical to microporous disks manufactured under similar conditions.

Other methods for manufacturing of hydroxyapatite that give rise to different microstructures have been reported in the literature. Jarcho et al. (*38*) combined $Ca(NO_3)_2 \cdot 4\ H_2O$ and $(NH_4)_2HPO_4$, which precipitated hydroxyapatite. After filtering and drying considerable cracking occurred, yielding only 3 mm thick slabs of green material. Dense

hydroxyapatite was obtained after sintering for 1 hour between 1000 and 1200 °C. Akao et al. (*75*) synthesized hydroxyapatite from $Ca(OH)_2$ and H_3PO_4. The hydroxyapatite was mixed with 1 % cornstarch, compacted, and sintered for 3 hours between 1150 and 1300 °C. Their procedure gave disks with porosities between 0.028 and 0.194, with a grain size between 1.04 and 3.40 μm. Peelen et al. (*76*) mixed hydroxyapatite powder with a hydrogen peroxide solution to produce a slurry. After filtering and drying, the hydroxyapatite was sintered for six hours between 1100 and 1400 °C. The porosity ranged from 0.25 to 0.60, and increased with the amount of hydrogen peroxide used. They report that interconnected pores with diameters between 150 and 250 μm exist along with micropores with a diameter between 0.5 and 1.5 μm. Since the manufacturing procedure influences the pore geometry and pore size distribution, an interesting pursuit would be to use percolation theory to characterize ceramic disks made by these or other manufacturing procedures.

Since ceramics are nonductile and brittle, fracture is a common mechanism for failure. In designing a porous ceramic implant, mechanical strength of the implant is an important concern. Pores obviously decrease the cross-sectional area on which a load can be applied.

Experimentally, for hydroxyapatite (77) and other ceramics (73), it has been determined that the strength of the ceramic decreases exponentially with an increase in porosity. Most of the current ceramics research is aimed at increasing the strength of a ceramic by eliminating the residual porosity, thus an important area where more research is needed, especially for bioceramics, is the manufacturing of strong porous ceramics.

Akao et al. (75), Jarcho et al. (38), and Peelen et al. (76) have examined the mechanical properties of the hydroxyapatite ceramics that they had manufactured. A more interesting and unique approach would be to study the mechanical properties of porous composite hydroxyapatite and β-whitlockite bioceramics by combining these materials with a stronger ceramic such as aluminum oxide, spinel ($MgAl_2O_4$), or fluorapatite ($Ca_{10}F_2(PO_4)_6$). The change in chemical composition, alone, could increase the mechanical strength of the composite; also the presence of a second phase inclusion in the composite could limit the extent of the grain growth, which in turn, would increase the mechanical strength. Varying the amount of fluorapatite, in hydroxyapatite-fluorapatite composites, would allow for the study of changes in mechanical strength and

microstructure without changing the overall crystal lattice of the system.

B. Percolation theory

The volume fraction accessible and volume fraction isolated curves (Figures 42-49) as a function of porosity correspond to those predicted by percolation theory except for the portion of the curve where the porosity is less than the percolation threshold. Since the mathematics of percolation theory assumes an infinite lattice (*1-3*) and the ceramics systems are finite, it is hyphothesized that the observed deviations from percolation theory are due to the presence of surface pores, that is, accessible pores that are not sample spanning. These deviations are most apparent in Figures 42-45, where the volume fraction accessible curves do not approach zero for porosities less than ϕ_c, but rather approach a nonzero porosity that we have defined as ϕ^s. The surface porosities that were determined, from both helium and aqueous pycnometry, ranged from 0.049 to 0.090 (Table XXIII). Intuitively, the presence of accessible pores below the critical percolation threshold is reasonable, since these disks are finite in size. If one recalls the argument presented in the introduction, where $\partial\phi^a/\partial\phi$ is discontinuous at the critical

percolation threshold, the addition of one pore in the interspersion connects two dead-end accessible clusters to create one sample-spanning cluster. Therefore, surface pores must necessarily exist below the critical percolation threshold. An experiment that will be performed at a later date will examine the effects of the disks of different thicknesses on the surface porosity. By decreasing the surface area to volume ratio of the ceramic disks, it is hoped that a change in surface porosity will be observed.

The pre-exponential factor m and ϕ_c were determined using multivariate nonlinear regression (*72*) by fitting the volume fraction accessible data to the modified scaling relationship given in eq 19. The values of m and ϕ_c determined from the pycnometry experiments are listed in Table XXIV. The value of m in all cases was about 0.39.

As mentioned in the introduction, the critical percolation threshold ϕ_c is dependent on the coordination of the interspersion. Conversely, one can estimate the coordination of the interspersion from the value of the percolation threshold. Two common geometrical lattices encountered in ceramics and metals are the Voronoi (*4*) and tetrakaidecahedral (*78*) tessellations. Figure 52 consists of materials i and j distributed in Voronoi polyhedra. The

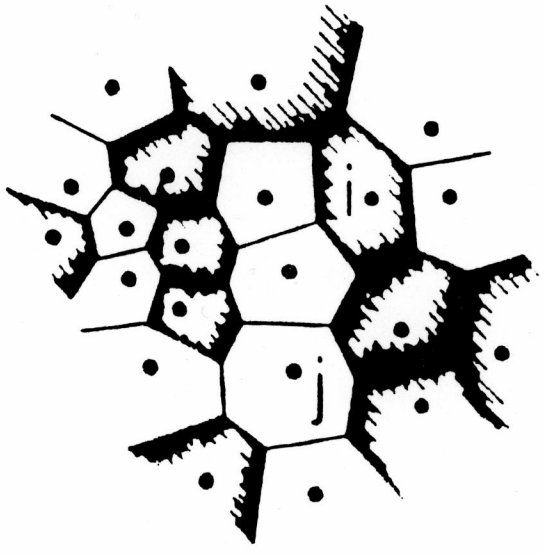

Figure 52. Voronoi polyhedra (*4*).

polyhedra are constructed by subdividing the space by Voronoi tessellation, a process whereby each set of points placed randomly in space is enclosed by the smallest polygon that can be formed by intersecting planes that bisect the lines connecting each point with its nearest neighbors. The average coordination of a Voronoi tessellation is 15.54; the critical percolation threshold for a lattice consisting of Voronoi polyhedra is 0.16 (*10*). A tetrakaidecahedron is pictured in Figure 53. This polyhedron has six square faces and eight hexagonal faces with twenty-four vertices, each having two angles of 120° and one of 90°. A lattice consisting of tetrakaidecahedra has a coordination of 14 and a critical percolation threshold of 0.175 (*9*).

The multivariate nonlinear regression analysis of the volume fraction accessible data for β-whitlockite disks with porosities between ϕ_c and 0.35, estimated ϕ_c to be 0.174, which corresponds to a tetrakaidecahedral lattice. Regression analysis for the hydroxyapatite disks, gave a estimated value of 0.188 for the percolation threshold. Using eq 8, the coordination number of the hydroxyapatite lattice is about 13.3. This suggests that the lattice may consist of distorted tetrakaidecahedra. Distorted tetrakaidecahedra that have all corners meeting at 109°

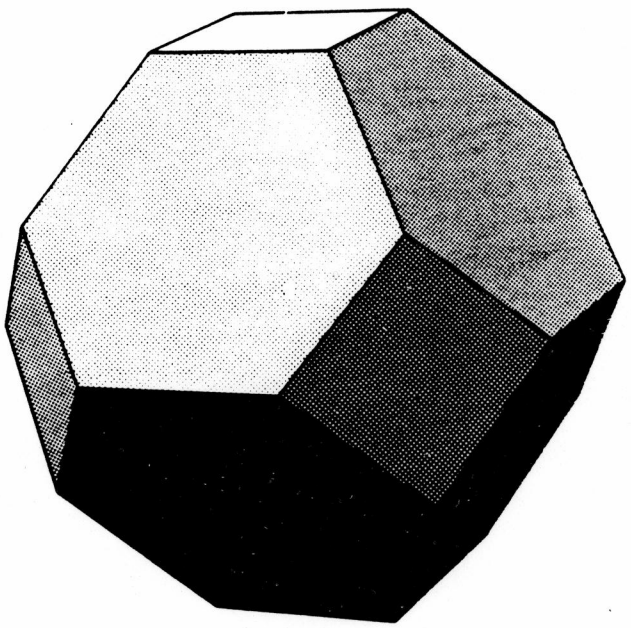

Figure 53. A tetrakaidecahedron (*78*).

and all edges at 120° have been reported in the literature (*78*). By considerably increasing the size of the pores in a compacted ceramic using alternate manufacturing processes, it may be possible to alter the coordination of the lattices. Since a change in coordination would also change the critical percolation threshold, percolation studies of macroporous ceramics would be interesting.

C. Bulk diffusion coefficients

The bulk diffusion coefficients D_B of benzoate through hydroxyapatite were determined using a Stokes diaphragm cell. When performing these types of experiments, several factors that can affect the value of D_B must be addressed. These include: (1) the presence of a diffusion layer on the surfaces of the membrane, (2) the direction of transport, (3) the approach to steady-state, (4) interaction of solute with the membrane, and (5) the sensitivity of the detection method.

First, the diffusion layer thickness was minimized in our experiments by placing magnets on the top and bottom surfaces of the hydroxyapatite membrane and rotating the cell at a high speed (100 rpm). In addition to the magnets on the surface of the membrane, magnets were placed in the

center of each half-cell in order to keep the solutions well stirred.

Second, much discussion on the configuration of the cells has been reported (*79*). In order to eliminate convection, the membrane should be horizontal (*79*). Convection can still occur in a diaphragm cell that has a vertical orientation (membrane is horizontal), if the donor solution is in the upper half-cell (*79*). But in order for this to occur, a density gradient within in the cell must exist. The density gradient in experiment 1 (donor solution in the upper half-cell) was negligible, since the concentration of the benzoate was low (0.00204 mol dm^{-3}). In experiment 2, the donor solution was housed in the lower half-cell. Under this condition, convection cannot occur (*79*). To examine if the direction of transport affected the value of the D_B, two membranes were used in both experiments; the results that were obtained were not significantly different from each other (Table XXVIII). Similar reproducibility has been observed for the bulk diffusion coefficients of benzoate through aluminum oxide membranes (*20*).

Third, in deriving eq 16 (Appendix B), it is assumed that steady-state conditions exist. For most of the hydroxyapatite membranes that gave measurable bulk

diffusion coefficients, steady-state conditions were reached within 24 hours, the only exception being for a membrane with a porosity of 0.238. Here, steady-state conditions were reached after one week.

Fourth, interactions between the solute and the membrane, if any, during diffusion will not affect the steady-state flux of the diffusing solute. Since eq 16 assumes that steady-state conditions exist, the values of the bulk diffusion coefficient will also be unaffected.

Fifth, the calculation of the diffusion coefficient requires accurate knowledge of the concentration differences in the two half-cells. Therefore the accuracy and the detection limit of the analytical technique are important. The critical percolation threshold for hydroxyapatite, determined by pycnometry, was 0.188. However two disks, with porosities of 0.201 and 0.202, showed no detectable diffusion of benzoate. Another concern was the use of the mass balance relationship to calculate the concentration of benzoate in the lower half-cell. In experiment 1, it is possible that diffusion of benzoate did occur through the disks with porosities just above the percolation threshold. However subtraction of the mass of benzoate in the donor cell at time t from the initial mass yields a small difference with a large

uncertainty. This problem can be overcome in part, but not entirely avoided, by placing the donor solution in the lower half-cell (experiment 2), and monitoring the concentration of benzoate as it diffuses into the upper half-cell. Here the measurements are affected by the detection limits of the HPLC detector. The measured concentrations are small and still have a substantial uncertainty, but one can conclude if the diffusion coefficient is nonzero. In experiment 2, no detectable diffusion of benzoate was found for the disks with porosities 0.201 and 0.202. In order to determine accurate values of D_B for disks with porosities just above the percolation threshold, a more sensitive detection method is needed.

Since the diffusion coefficients for disks with porosities just above ϕ_c were difficult to determine with accuracy, the critical percolation threshold from the pycnometry experiments (ϕ_c = 0.188) was used to fit the diffusion data to the scaling relationship given in eq 21. The calculated regression line deviates significantly from the experimental bulk diffusion coefficients for disks with high porosity (Figure 51). By performing additional diffusion experiments using disks with porosities between 0.25 and 0.35, a better fit may be obtained. Bulk

diffusion coefficients for benzoate through β-whitlockite disks will be determined in the future. Finally, the aqueous diffusion coefficient for benzoate will be determined. Then volume fraction effective values can be calculated, and modeled using the scaling relationship given in eq 22.

V. Conclusions

In this research, we have shown that hydroxyapatite and β-whitlockite ceramics can be manufactured to give reproducible porosities, and that the sintering temperature is the principal variable that affects the amount of residual porosity.

We have also shown that the disks can be characterized using percolation theory. From volume fraction accessible and volume fraction isolated data, the critical percolation threshold and coordination of the interspersion can be obtained. The coordination of both ceramic lattices correspond to tetrakaidecahedral tessellations.

Finally, the rate of diffusion of a water-soluble substance through hydroxyapatite disks can be modeled as function of porosity using percolation theory. The bulk diffusion coefficient that is obtained is a function of the aqueous diffusion coefficient, disk porosity, and percolation threshold.

Since the rate of diffusion of the solute through the disk is a function of disk porosity, and the porosity can be controlled through the manufacturing procedure, it is possible that hydroxyapatite and β-whitlockite bioceramics may someday be considered as controlled drug delivery devices.

VI. References

(1) Stauffer, D. *Introduction to Percolation Theory*; Taylor and Francis: London, 1985; pp 1-58, 87-100.

(2) Efros, A. L. *Physics and Geometry of Disorder* (*Engl. Trans.* by Kisin, V. I.); Mir: Moscow, 1986; pp 14-134, 179-226.

(3) Essam, J. W. *Rep. Prog. Phys.* **1980**, *43*, 834-912.

(4) Mohanty, K. K.; Ottino, J. M.; Davis, H.T. *Chem. Engng. Sci.* **1982**, *37*, 905-924.

(5) Hastedt, J. E. M.S. Thesis, University of Wisconsin - Madison, 1988.

(6) Kirkpatrick, S. *Rev. Mod. Phys.* **1973**, *45*, 574-588.

(7) Dean, P.; Bird, N. F. *Monte Carlo Studies of the Percolation Properties of Two and Three Dimensional Lattices*, Mathematics Division Report Ma61 of the National Physical Laboratory, Teddington, Middlesex, England, 1966.

(8) Yuge, Y.; Hori, M. *J. Phys. A: Math. Gen.* **1987**, *20*, 3523-3531.

(9) Domb, C.; Dalton, N. W. *Proc. Phys. Soc.* **1966**, *89*, 859-871.

(10) Hastedt, J. E.; Wright, J. L. *Pharm. Res.*, in press.

(11) Winterfeld, P. H. Ph.D. Thesis, University of Minnesota, 1981.

(12) Flory, P. J. *J. Am. Chem. Soc.* **1941**, *63*, 3083-3090.

(13) Flory, P. J. *J. Am. Chem. Soc.* **1941**, *63*, 3091-3096.

(14) Flory, P. J. *J. Am. Chem. Soc.* **1941**, *63*, 3096-3100.

(15) Hastedt, J. E.; Wright, J. L. Presented at the 21st Annual Pharmaceutics Graduate Student Research Meeting, Minneapolis, MN, June 1989; paper 27.

(16) Mulski, M. J. M.S. Thesis, University of Wisconsin - Madison, 1989.

(17) Wright, J. L.; Ellis, S. R.; Skwierczynski, R. D. Presented at the 1988 Spring Meeting of the Materials Research Society, Reno, NV, April 1988; paper B1.2.

(18) Skwierczynski, R. D.; Wright, J. L. Presented at the 21st Annual Pharmaceutics Graduate Student Research Meeting, Minneapolis, MN, June 1989; paper 28.

(19) Ellis, S. R.; Wright, J. L. Presented at the 21st Annual Pharmaceutics Graduate Student Research Meeting, Minneapolis, MN, June 1989; paper 29.

(20) Ellis, S. R.; Wright, J. L. University of Wisconsin - Madison, unpublished results.

(21) Van Vlack, L. H. *Physical Ceramics for Engineers*; Addison-Wesley: Reading, MA, 1964; pp 227-258.

(22) Carstensen, J. T. *Solid Pharmaceutics: Mechanical Properties and Rate Phenomena*; Academic: New York, 1980; pp 135-140, 167-170.

(23) Reference 22, pp 202-206.

(24) Reference 21, pp 259-280.

(25) Reference 21, pp 151-155.

(26) Kingery, W. D.; Bowen, H. K.; Uhlmann, D. R. *Introduction to Ceramics*, 2nd ed., John Wiley and Sons: New York, 1976; pp 448-490.

(27) Glasstone, S.; Laidler, K. J.; Eyring, H. *The Theory of Rate Processes*, McGraw-Hill: New York, 1941; pp 516-551.

(28) Hiemenz, P. C. *Principles of Colloid and Surface Chemistry*, 2nd ed., Marcel Dekker; New York, 1986; pp 302-307.

(29) Smith, L. *Arch. Surg.* **1963**, *87*, 653-661.

(30) Boretoss, J. W. *CHEMTECH* **1987**, *17*, 224-231.

(31) Hench, L. L.; Ethridge, E. C. *Biomaterials - An Interfacial Approach*; Academic: New York, 1982.

(32) Van Raemdonck, W.; Ducheyne, P.; De Meester, P. In *Metal and Ceramic Biomaterials*, Vol. II; Ducheyne, P.; Hastings, G. W., Eds.; CRC: Boca Raton, FL, 1984; pp 143-166.

(33) Shimazaki, K.; Mooney, V. *J. Orthop. Res.* **1985**, *3*, 301-310.

(34) Klein, C. P. A. T.; Driessen, A. A.; de Groot, K.; van den Hoof, A. *J. Biomed. Mater. Res.* **1983**, *17*, 769-784.

(35) Uchida, A.; Nade, S. M. L.; McCartney, E. R.; Ching W. *J. Bone Joint Surg. (Br)* **1984**, *66-B*, 169-275.

(36) de Groot, K. In *Biocompatibility of Clinical Implant Materials*, Vol. I; Williams, D. F., Ed.; CRC: Boca Raton, FL, 1981; pp 199-222.

(37) Hench, L. L.; Wilson, J. *Science* **1984**, *226*, 630-636.

(38) Jarcho, M.; Bolen, C. H.; Thomas, M. B.; Bobich, J.; Kay, J. F.; Doremus, R. H. *J. Mater. Sci.* **1976**, *11*, 2027-35.

(39) Dennison, H. W.; de Groot, K.; Makkes, P. C.; van den Hooff, A.; Klopper, P. J. *J. Biomed Mater. Res.* **1980**, *14*, 713-721.

(40) Holmes, R. E. *Plast. Reconstr. Surg.* **1979**, *63*, 626-633.

(41) Reference 22, pp 52-57.

(42) Higuchi, T. *J. Pharm. Sci.* **1963**, *52*, 1145-1149.

(43) Singh, P.; Desai, S. J.; Simonelli, A. P.; Higuchi, W. I. *J. Pharm. Sci.* **1967**, *56*, 1548-1555.

(44) Schwartz, J. B.; Simonelli, A. P.; Higuchi, W. I. *J. Pharm. Sci.* **1968**, *57*, 274-277.

(45) Schwartz, J. B.; Simonelli, A. P.; Higuchi, W. I. *J. Pharm. Sci.* **1968**, *57*, 278-282.

(46) Paul, D. R.; McSpadden, S. K. *J. Membrane Sci.* **1976**, *1*, 33-48.

(47) Chien, Y. W. In *Sustained and Controlled Release Drug Delivery Systems*, Robinson, J. R., Ed.; Marcel Dekker: New York, 1978, pp 211-349.

(48) Langer, R. S.; Rhine, W. D.; Hsieh, D. S. T.; Bawa, R. S. In *Controlled Release of Bioactive Materials*, Baker, R., Ed.; Academic: New York, 1980, pp 83-98.

(49) Roseman, T. J.; Cardarelli, N. F.; In *Controlled Release Technologies: Methods, Theory, and Applications*, Vol. I; Kydonieus, A. F., Ed.; CRC: Boca Raton, FL, 1980; pp 21-71.

(50) Cardinal, J. R. In *Recent Advances in Drug Delivery Systems*, Anderson, J. M.; Kim, S. W., Eds.; Plenum: New York, 1984, pp 229-248.

(51) Langer, R.; Brown, L.; Edelman, E. In *Recent Advances in Drug Delivery Systems*, Anderson, J. M.; Kim, S. W., Eds.; Plenum: New York, 1984, pp 249-258.

(52) Peppas, N. A. In *Recent Advances in Drug Delivery Systems*, Anderson, J. M.; Kim, S. W., Eds.; Plenum: New York, 1984, pp 279-289.

(53) Siegel R. A.; Cohen J. M.; Brown, L.; Langer, R. In *Recent Advances in Drug Delivery Systems*, Anderson, J. M.; Kim, S. W., Eds.; Plenum: New York, 1984, pp 315-320.

(54) Bawa, R.; Siegel, R. A.; Marasca, B.; Karel, M.; Langer, R. *J. Contrl. Rel.* **1985**, *1*, 259-267.

(55) Langer, R.; Leong, K.; Edelman, E.; Siegel, R.; Bawa, R. In *Controlled Drug Delivery*, Mueller, B. W., Ed.; Wissenschaftliche Verlagsgesellschaft: Stuttgart, 1987, pp 146-160.

(56) Peppas, N. A. In *Controlled Drug Delivery*, Mueller, B. W., Ed.; Wissenschaftliche Verlagsgesellschaft: Stuttgart, 1987, pp 161-173.

(57) Heller, J. In *Controlled Drug Delivery*, Robinson, J. R.; Lee, V. H. L., Eds.; Marcel Dekker: New York, 1987, pp 179-212.

(58) Chien, Y. W. In *Controlled Drug Delivery*, Robinson, J. R.; Lee, V. H. L., Eds.; Marcel Dekker: New York, 1987, pp 481-522.

(59) Langer, R. *Pharm. Technol.* **13**(8), 18-30.

(60) Siegel, R. A. In *Controlled Release of Drugs: Polymers and Aggregate Systems*, Morton Rosoff, Ed.; VCH: New York, 1989, pp 1-51.

(61) *Powder Diffraction File- Inorganic Phases*, McClure, W. F., Ed.; International Centre for Diffraction Data (JCPDS): Swarthmore, PA, 1986.

(62) Reference 22, p 71.

(63) Connors, K. A. *A Textbook of Pharmaceutical Analysis*, 3rd ed., John Wiley and Sons: New York, 1982, pp 321-327.

(64) The Propyl 4-hydroxybenzoate served as a preservative to prevent bacterial degradation of benzoate. Wickliffe, B.; Entrekin, D. N. *J. Pharm. Sci.* **1964**, *53*, 769-773.

(65) Reference 22, pp 39-43.

(66) Carstensen, J. T.; Hou, X. *Powder Technol.* **1985**, *42*, 153-157.

(67) Reference 61, file no. 18-303.

(68) Reference 61, file no. 9-169.

(69) Reference 61, file no. 9-432.

(70) The value 0.2 μm was estimated using the Washburn equation assuming a contact angle of 135° between mercury and hydroxyapatite. Reference 28, p 338. Scanning electron microscopy verified that the pores were less than 0.2 μm.

(71) Reference 63, pp 604-608.

(72) Wilkinson, L.; Bjerknes, M. *Systat*, version 3.1; Systat: Evanston, IL, 1987.

(73) Reference 26, pp 808-812.

(74) Reference 26, pp 904-910, 947-960, 1006-1014.

(75) Akao, M.; Aoki, H.; Kato, K. *J. Mater. Sci.* **1981**, *16*, 809-812.

(76) Peelen, J. G. J.; Rejda, B. V.; de Groot, K. *Ceramurgia Int.* **1978**, *4*, 71-74.

(77) Rao, W. R.; Boehm, R. F. *J. Dent. Res.* **1974**, *53*, 1351-1354.

(78) Reference 26, p 524.

(79) Cussler, E. L. Diffusion - Mass Transfer in Fluid Systems, Cambridge University: New York, 1984; pp 132-137, 314-316.

(80) Reference 79, pp 26-28.

Appendix A

Derivation of Volume Fraction Isolated as a Function of Porosity and Pycnometric Density

Let

V^i be the volume of isolated conducting sites,

V^a be the volume of accessible conducting sites,

V^n be the volume of nonconducting sites,

m be the mass of the ceramic disk, and

V^t be the total volume of the disk:

$(V^t = V^i + V^a + V^n)$.

Begin with the identity

$$V^i = V^i + V^n - V^n \tag{A.1}$$

Divide eq A.1 by V^t

$$\frac{V^i}{V^t} = \frac{V^i + V^n}{V^t} - \frac{V^n}{V^t} \tag{A.2}$$

By definition, volume fraction isolated, ϕ^i, is equal to

$$\phi^i \equiv \frac{V^i}{V^t} \tag{A.3}$$

Substituting eq A.3 into eq A.4 gives

$$\phi^i = \frac{V^i + V^n}{V^t} - \frac{V^n}{V^t} \tag{A.4}$$

Multiplying each term on the right hand side of eq A.4 by m/m gives

$$\phi^i = \frac{V^i + V^n}{m} \frac{m}{V^t} - \frac{m}{V^t} \frac{V^n}{m} \tag{A.5}$$

Each term on the right hand side of eq A.5 can now be expressed as a density:

$$\rho_{pyc} = \frac{m}{V^i + V^n} \tag{A.6}$$

$$\rho_{theory} = \frac{m}{V^n} \tag{A.7}$$

and

$$\rho = \frac{m}{V^t} \tag{A.8}$$

where ρ_{pyc} is the pycnometric density of the ceramic disk, ρ is the geometric density of the ceramic disk, and ρ_{theory} is the theoretical density of the powder.

Substituting eq A.6, A.7, and A.8 into eq A.5 and factoring yields:

$$\phi^i = \rho \left(\frac{1}{\rho_{pyc}} - \frac{1}{\rho_{theory}} \right) \tag{A.9}$$

Recall that porosity is defined as

$$\phi \equiv 1 - \frac{\rho}{\rho_{theory}} \tag{A.10}$$

Rearranging eq A.10 and substituting into eq A.9, in order to eliminate ρ, yields after simplification,

$$\phi^i = (1 - \phi) \left(\frac{\rho_{theory}}{\rho_{pyc}} - 1 \right) \tag{A.11}$$

Since ρ_{theory} is a constant, volume fraction isolated is a function of both porosity and pycnometric density, each of which can be determined experimentally.

Appendix B

Stokes Diaphragm Cell Diffusion - Derivation of Flux Equation

In this derivation, it is assumed that steady-state is approached even though the concentrations in the donor and receiver half-cells are changing with time (*80*). An exact solution to this problem is elaborate and is not necessary for our purposes.

Consider a membrane of thickness δ in a Stokes diaphragm cell. Let the concentration of diffusing solute in the donor half-cell be C_d and the concentration in the receiver half-cell be C_r. By applying Fick's second law,

$$\frac{\partial C}{\partial t} = D_B \frac{\partial^2 C}{\partial z^2} \qquad \text{(B.1)}$$

where D_B is the bulk diffusion coefficient of solute through the porous membrane and C is the concentration of solute in the membrane, and assuming that a pseudosteady-state condition exists then

$$\frac{\partial C}{\partial t} \approx 0 \qquad \text{(B.2)}$$

From eq B.1 and B.2, it follows that

$$\frac{\partial^2 C}{\partial z^2} = 0 \qquad \text{(B.3)}$$

This differential equation can be solved by integrating twice, giving

$$C = a_1 \times z + a_2 \qquad \text{(B.4)}$$

The boundary and initial conditions for the solute concentration in the membrane are

Boundary Conditions

$$C = C_d \text{ at } z = 0;\ t > 0 \qquad \text{(B.5a)}$$

$$C = C_r \text{ at } z = 0;\ t > 0 \qquad \text{(B.5b)}$$

Initial Conditions

$$C = C_d^\circ \text{ at } t = 0 \qquad \text{(B.6a)}$$

$$C = C_r \text{ at } t = 0 \qquad \text{(B.6b)}$$

Applying these boundary conditions to eq B.4, the constants a_1 and a_2 can be determined:

$$C_d = a_1 \times 0 + a_2 \tag{B.7a}$$

$$C_r = a_1 \times \delta + a_2 \tag{B.7b}$$

Thus,

$$a_1 = \frac{C_d - C_r}{\delta} \tag{B.8a}$$

and

$$a_2 = C_d \tag{B.8b}$$

Substituting eq B.8a and B.8b into eq B.4, gives the following linear concentration profile

$$C = C_d - \left[\frac{(C_d - C_r)}{\delta}\right] z \tag{B.9}$$

which is shown in Figure B.1.

The flux j can be found by applying Fick's first law

$$j = -D_B \frac{dC}{dz} \tag{B.10}$$

Differentiating eq B.9 with respect to z and substituting in eq B.10 gives

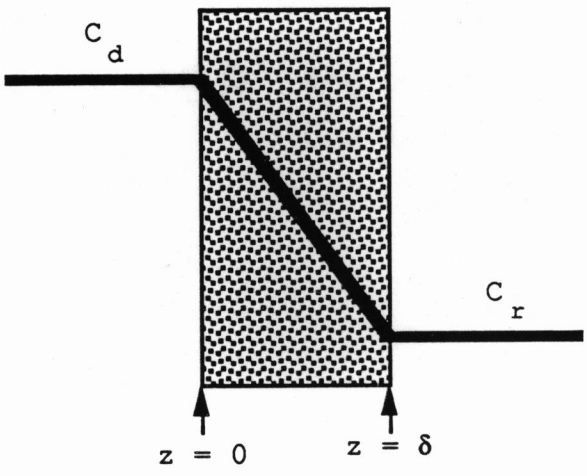

Figure B.1. Concentration profile of diffusing solute in the membrane of a Stokes diaphragm cell.

$$j = \frac{D_B}{\delta} (C_d - C_r) \qquad (B.11)$$

Since the number of solute particles leaving the donor half-cell must be equal to the number entering the receiver half-cell, the following mass balance conditions must exist

$$V_r \frac{dC_r}{dt} = A\ j = \frac{A\ D_B}{\delta} (C_d - C_r) \qquad (B.12a)$$

and

$$V_r \frac{dC_r}{dt} = -A\ j = -\frac{A\ D_B}{\delta} (C_d - C_r) \qquad (B.12b)$$

where V_r and V_d are the volumes of the receiver half-cell solution and donor half-cell solution, respectively, and A is the area of the membrane in contact with the solutions. If eq B.12a and B.12b are divided by V_r and V_d, respectively, and eq B.12a is subtracted from eq B.12b, the following first-order separable differential equation is obtained

$$\frac{d(C_d - C_r)}{dt} = -D_B \beta (C_d - C_r) \qquad (B.13)$$

where β is a constant characteristic of each diaphragm cell

$$\beta = \frac{A}{\delta}\left(\frac{1}{V_d} + \frac{1}{V_r}\right) \tag{B.14}$$

Separating the variables $(C_d - C_r)$ and t in eq B.13 yields

$$\frac{d(C_d - C_r)}{(C_d - C_r)} = -D_B\,\beta\,dt \tag{B.15}$$

Applying the initial conditions, eq B.6a and B.6b, to B.15 gives

$$\int_{C_d^\circ}^{(C_d - C_r)} \frac{d(C_d - C_r)'}{(C_d - C_r)'} = -D_B\,\beta \int_0^t dt' \tag{B.16}$$

Integrating eq B.16 gives the desired result:

$$\ln\left[\frac{(C_d - C_r)}{C_d^\circ}\right] = -D_B\,\beta\,t \tag{B.17}$$

Approved:

Kenneth A. Connors

Professor Kenneth A. Connors

Nov. 27, 1989

Date